Fall 2014

Modeling and characterization of non-ideal effects in high-performance RF MEMS tuners

Juan Zeng
Purdue University

Graduate School Form 30
(Revised 08/14)

PURDUE UNIVERSITY
GRADUATE SCHOOL
Thesis/Dissertation Acceptance

This is to certify that the thesis/dissertation prepared

By Juan Zeng

Entitled
Modeling and Characterization of Non-Ideal Effects in High-Performance RF MEMS Tuners

For the degree of Doctor of Philosophy

Is approved by the final examining committee:

DIMITRIOS PEROULIS

BYUNGHOO JUNG

MARISOL KOSLOWSKI

ANIL BAJAJ

To the best of my knowledge and as understood by the student in the Thesis/Dissertation Agreement, Publication Delay, and Certification/Disclaimer (Graduate School Form 32), this thesis/dissertation adheres to the provisions of Purdue University's "Policy on Integrity in Research" and the use of copyrighted material.

DIMITRIOS PEROULIS

Approved by Major Professor(s): _____

_____

Approved by: V. Balakrishnan 12/03/2014

Head of the Department Graduate Program Date

MODELING AND CHARACTERIZATION OF NON-IDEAL EFFECTS IN HIGH-PERFORMANCE RF MEMS TUNERS

A Dissertation

Submitted to the Faculty

of

Purdue University

by

Juan Zeng

In Partial Fulfillment of the

Requirements for the Degree

of

Doctor of Philosophy

December 2014

Purdue University

West Lafayette, Indiana

This dissertation is dedicated to my family for their love and support.

ACKNOWLEDGMENTS

First and foremost, I would like to express my heartfelt gratitude to my advisor Professor Dimitrios Peroulis for his aspiring guidance, constant support and encouragement throughout my Ph.D. program at Purdue University. He is the best role model for me with his academic excellence and teaching enthusiasm. It is my honor to work with him during the past five years.

I also would like to thank Professor Anil K. Bajaj, Professor Byunghoo Jung and Professor Marisol Koslowski for serving on my dissertation committee. I am very grateful to Professor Anil K. Bajaj for the insightful discussions on our collaborated projects and for reviewing my manuscripts with detailed comments. Professor Jung and Professor Marisol Koslowski have provided insightful and constructive feedback to help me improve the work presented in this dissertation.

I am also thankful to all the former and current colleagues in our ARES group: Dr. Abbas Semnani, Dr. Dimitra Psychogiou, Dr. Nithin Raghunathan, Dr. Yu-Chiao Wu, Dr. Sean Scott, Dr. Wesley Allen, Dr. Xin Wang, Dr. Hao Han Hsu, Dr. Xiaguang (Leo) Liu, Dr. Joshua Small, Dr. Adam Fruehling, Dr. M. Shoaib Arif, Dr. Wasim Irshad, Dr. Kenle Chen, Dr. David Berdy, Dr. Eric Naglich, Dr. Tsung-Chieh Lee, Andrew Kovacs, Anurag Garg, Zhengan (Andy) Yang, Mihal (Michael) Sinani, Mark Hickle, Yu-Chen Wu, Wei Yang, Kaiyuan Zeng, Ruiyi Mao, Michael Hall, Mohammad Abu Khater, Jin Li. I am very fortunate to work with all these talented people in such a collaborative group.

I cannot be more grateful to my host family, Susan Ploss and Rich Ploss, for the continuous love and support since we met in 2007. Also thank you to all my friends for making my life more joyful and colorful.

Last but not least, I would like to thank my parents and my husband for their unconditional love and support. I cannot be more blessed to have met my husband Jian Wang who has always been considerate and supportive.

TABLE OF CONTENTS

Page

Page

LIST OF TABLES

LIST OF FIGURES

Figure Page

ABSTRACT

Zeng, Juan Ph.D., Purdue University, December 2014. Modeling and Characterization of Non-Ideal Effects in High-Performance RF MEMS Tuners. Major Professor: Dimitrios Peroulis.

Abstract: The emerging standards for the next-generation wireless communication system demand for multi-band RF front-ends. Reconfigurable RF devices based on MEMS technology have emerged with the potential to significantly reduce the system complexity and cost. Robust operation of RF MEMS tuners under the non-ideal effects due to fabrication uncertainties and environmental variations is critical in achieving reliable RF MEMS reconfigurable devices. Therefore, it is essential to model and characterize these non-ideal effects, and further to alleviate these non-ideal effects by design optimization.

In this dissertation, the effects of non-perfect anchor support, residual stress, and temperature sensibility of MEMS tuners have been studied. The anchor supports of MEMS beams, which are widely used as tunable components, are often far from the ideally assumed built-in or step-up conditions. An equation-based nonlinear model for inclined supports in non-flat fixed-fixed beams has been developed and validated by experimental results. Residual stress developed during the fabrication presents the major challenges in developing reliable MEMS tuners. An efficient extraction method for in-plane residual stress has been proposed using a single beam test structure. This method has been demonstrated by wafer-scale measurements of electrostatically actuated beams. The statistic and spatial distribution of extracted residual stresses on a quarter wafer is presented, and the accuracy of this method is evaluated by uncertainty analysis. With the awareness the residual stress effects, the design optimization has been conducted for designing stress-tolerant micro-corrugated diaphragm tuners

used in tunable cavity resonators/filters. Furthermore, the temperature sensitivity issue results from the mismatch of material properties between the structure material and substrate has been discussed and a thermally-stable RF MEMS tuner based on a nonuniform micro-corrugated diaphragm has been proposed and experimentally validated over a wide temperature variation.

1. INTRODUCTION

1.1 Motivation

The rapid development of wireless communication technology has led to tremendous growth of emerging consumer and military applications of radio-frequency (RF) and microwave devices and systems. Fig. 1.1 presents the standards and frequencies of different wireless communication networks, which include personal area networks (PAN), local area networks (LAN), metropolitan area networks (PAN), and wide area networks (WAN) [1]. As frequency bands and new communication standards continue to proliferate, RF front-ends are required to operate over different frequency bands and to support a number of wireless standards. A ubiquitous example is the RF transceiver in an iPhone 6 Plus smart phone which is adaptable to multi-band operation (Fig. 1.2). Therefore, the next generation wireless communication puts higher demands on the RF front-ends, featuring small size, low weight, added functionality and low cost.

In the traditional parallel path structures, an RF signal from each standard is processed using a separate signal path. As a consequence, a number of duplicate antennas, switches, power amplifiers, and filters are needed. As a result, the power consumption, cost, and total size of the RF front-end increases as more standards are included. By sharing tunable building blocks between various standards, a reconfigurable system could greatly reduce the chip area and cost [3]. With the use of RF MEMS technology, reconfigurable building blocks such as tunable matching networks, filters, phase shifters and power amplifiers (PAs) can be realized for high-performance RF MEMS front-ends with the potential to be integrated with CMOS [4, 5]. Nowadays, the RF front-end implementation has been a combination of parallel structures and several shared tunable components. The diaphragm in Fig. 1.3 illustrates a mod-

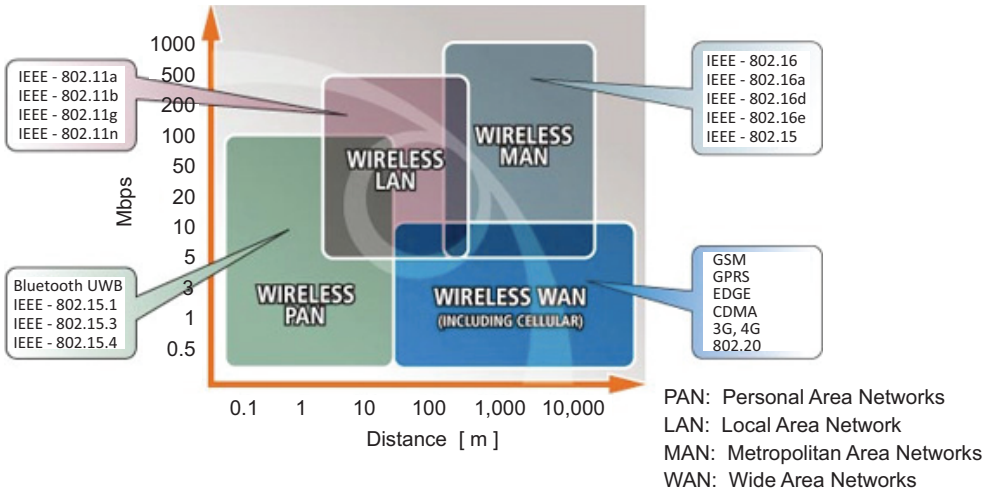

Fig. 1.1. The proliferation of wireless frequency bands and new communication standards demands for multi-band and multi-standard devices [1].

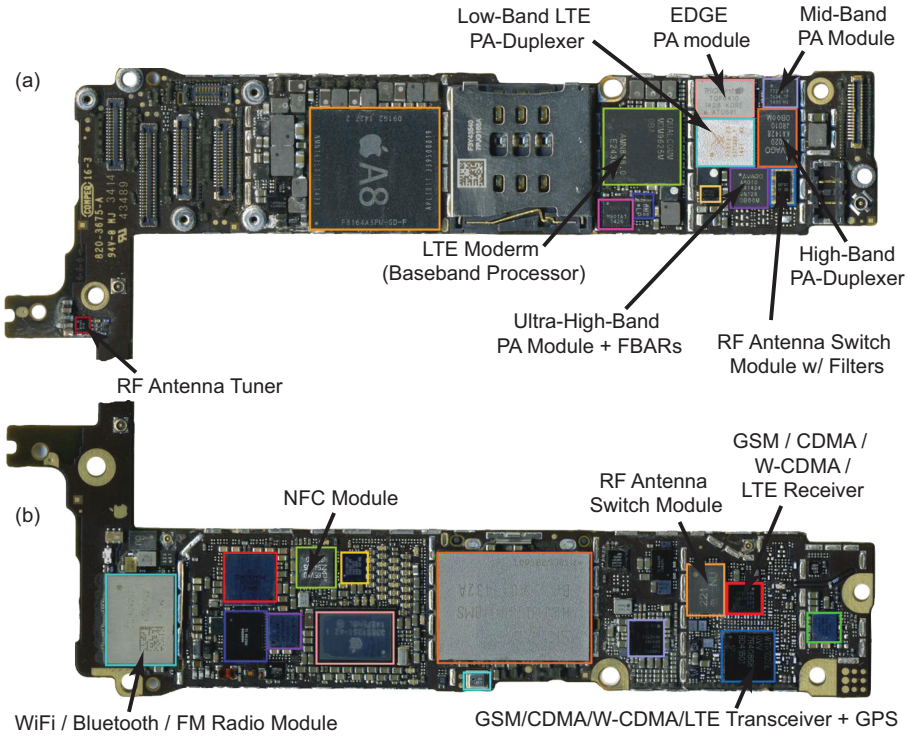

Fig. 1.2. PCB of the iPhone 6 Plus [2]: (a) front side, and (b) back side.

ern smart phone front-end structure with GSM and WCDMA bands. A broadband antenna is shared by multiple frequency bands, and antenna switching arrays are used to select the desired signal path. If more tunable devices, such as the tunable filters, are employed to replace all the discrete components, the system complexity will be further reduced.

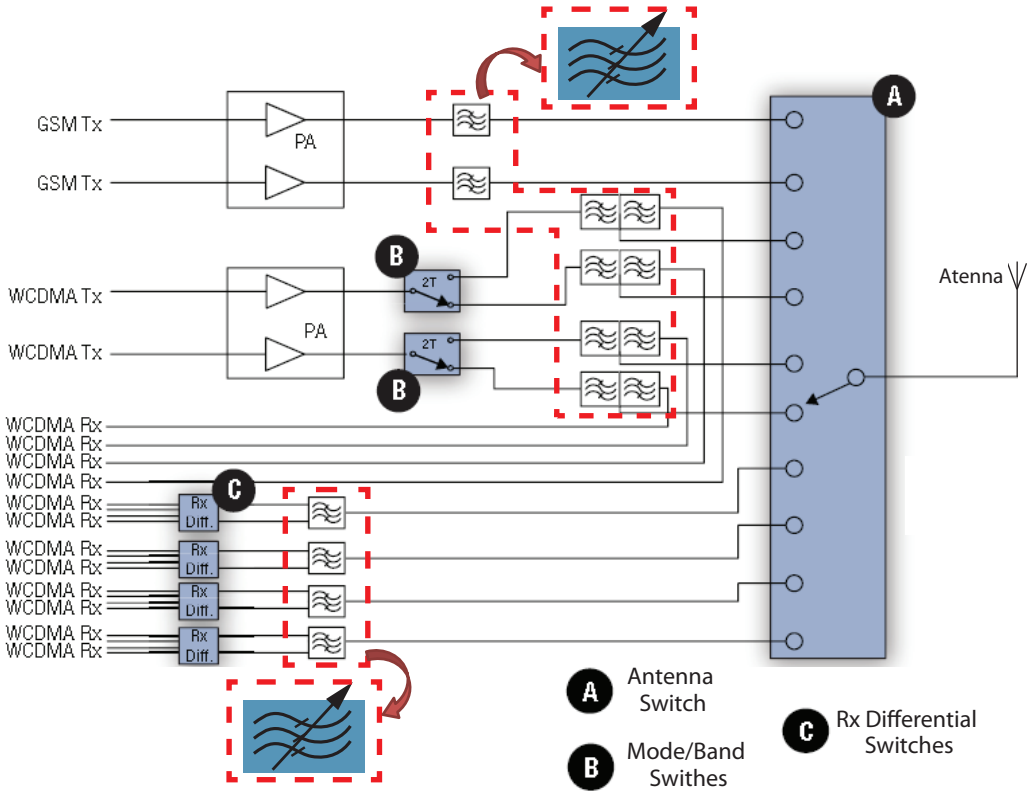

Fig. 1.3. A modern smart phone front-end diagram with GSM and WCDMA bands using parallel structures and several shared tunable components [6]. Tunable filters are desired to replace the discrete filters in the red dashed blocks.

RF microelectromechanical systems (MEMS) technology has emerged as the enabling technology for realizing reconfigurable wireless communication systems using high-performance tunable RF components [7]. Still, RF MEMS tunable blocks are not yet in wide production because there are non-ideal effects in these devices which cause stability and reliability issues. To fill the gap between prototypes and commer-

cial products, it is necessary to first fully characterize these non-ideal effects. This dissertation focuses on the modeling and characterization of non-ideal effects in RF MEMS tuners, and on the design optimization to improve the tolerance of the devices to fabrication variabilities and environmental effects.

1.2 RF MEMS Tunable Components

RF MEMS is one of the most promising technology in the RF and microwave area, providing low insertion loss, low power consumption, very high isolation, high power handling, high quality factor and good tunability [5]. These devices are fabricated with semiconductor surface micromachining and bulk micromachining processes which can be compatible with the fabrication of intergraded circuits. Unlike traditional electronic devices, RF MEMS components utilize their mechanical movement to provide RF functionalities and serve as low loss and linear tuning schemes.

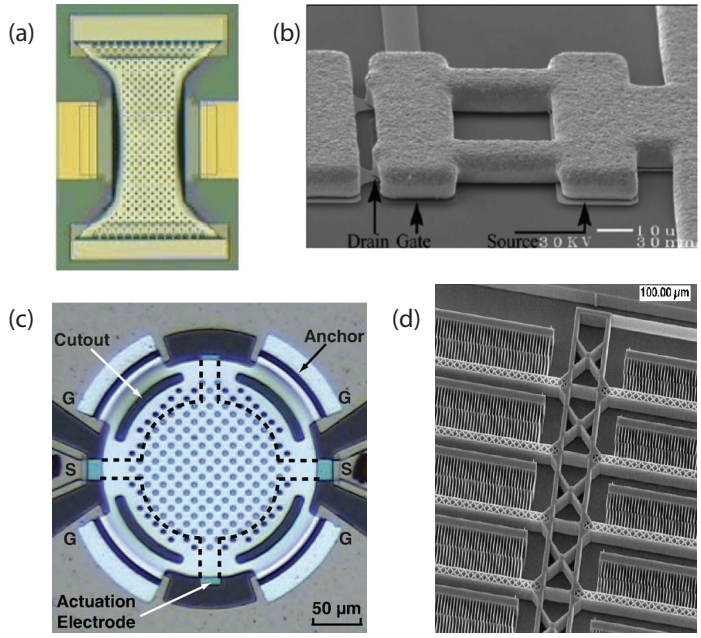

Fig. 1.4. Examples of RF MEMS tunable elements in the form of (a) a capacitive switch [8], (b) a metal contact switch [9], (c) a switched capacitor [10], and (d) an analog variable capacitor [11].

The MEMS capacitive bridge is the basic and essential tuning element in most tunable RF MEMS applications. A MEMS capacitive bridge consists of a suspended beam or plate and an actuation electrode. The bias voltage applied between the bridge and electrode generates an electrostatic force and deflects the micro bridge accordingly. There are mainly four different designs for MEMS capacitive bridges as shown in Fig. 1.4 [5]. When biased with discrete high/low voltages, the micro bridge can operate as a capacitive switch (Fig. 1.4(a)), or a metal contact switch (Fig. 1.4(b)), or a switched capacitor (Fig. 1.4(c)). The micro bridge has up/down states when the bias voltage is off/on, and can realize digital tuning. For example, digital impedance tuners have been implemented with capacitive switches loaded short-circuited shunt stubs whose electrical lengths were controlled by the switching states of the MEMS bridges [12, 13]. An analog variable capacitor (or a varactor) can be implemented when the micro bridge is biased with continuous voltage before contact occurs (Fig. 1.4(d)). Analog impedance tuners using MEMS variable capacitors have also been demonstrated with a wide tuning range [14]. The capacitive bridge can be used as a tunable capacitor or switch to change the load of resonators to fulfill a digital or analog tunable filter built with the resonators.

Tunable filters based on MEMS capacitive tuners have been demonstrated with different types of resonators, such as coplanar waveguide (CPW) resonators [15], microstrip resonators [16, 17] and evanescent-mode cavity resonators [18–20]. Among these implementations, the tunable cavity resonators/filters offer high-Q ($>$ 400 - 1,000) and wide tuning range ($>$ 2:1) from L- to W- band [20]. As shown in Fig. 1.5, continuously tunable cavity resonators/filters have been implemented using different tuning elements including cantilever tuners, beam tuners and diaphragm tuners.

1.3 Non-Ideal Effects in RF MEMS Tuners

As discussed previously, there are non-ideal effects in MEMS devices, such as fabrication variabilities [24], temperature sensitivities [10], dielectric charging [25],

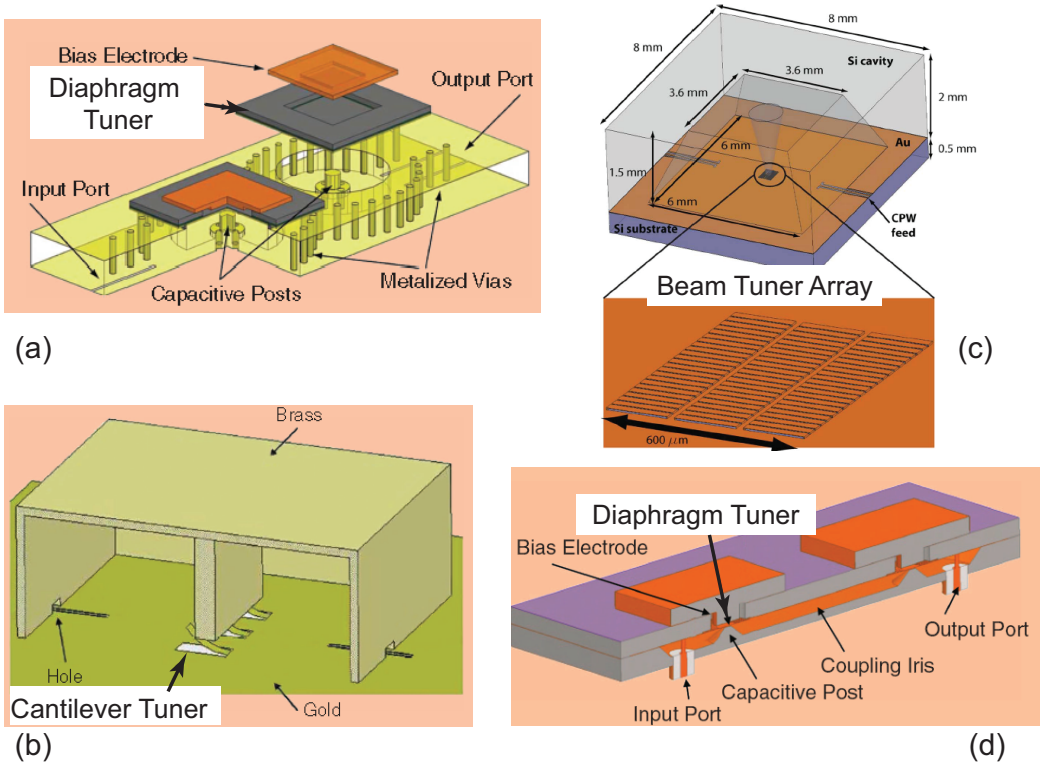

Fig. 1.5. Examples of continuous tunable cavity resonators/filters using (a), (d) a MEMS diaphragm tuner [18,21], (b) a MEMS cantilever tuner [22], and (c) a MEMS fixed-fixed beam tuner array [23].

contact wear [26], material fatigue and creep [27]. These non-ideal effects could cause performance degradation or even device failure. To design RF MEMS devices with good performance and reliability, these issues need to be effectively addressed.

In this dissertation, we focus on the non-ideal effects in capacitive RF MEMS tuners and cover non-perfect anchor effects, in-plane residual stress issues and temperature sensitivity. Non-perfect anchors alter the boundary conditions of the suspended bridge, and directly affect the accuracy of the device modeling using beam or plat theory. Residual stress could arise from the mismatch of both thermal coefficients of expansion (TCE) and crystal lattice periods between the substrate and the structural materials. Consequently, it is have to avoid in practically important fabrication processes [28]. For a fixed-fixed beam or peripherally clamped diaphragm, residual

stress is one of the key parameters in establishing structure reliability and functionality. Tensile residual stress increases the membrane stiffness and thus increases its actuation voltage. For non-planar devices, residual stress leads to a zero-load deflection, which could cause unwanted device topology. Therefore, knowledge of the fabrication-process-induced residual stress is crucial to the proper modeling and design of the MEMS devices. For devices that operate in environments with large temperature variations, thermally-induced stresses may change the device performance. For example, if excessive compressive stress is generated, buckling or even failure of the device may occur. The fixed-fixed micro beams or plates typically have a marked sensitivity to temperature since the device stress changes over temperature due to the mismatch of the thermal expansion coefficient between the MEMS structural material and the substrate. In most practical cases, stress becomes compressive at high temperatures, and causes stress-induced offsets and stiffness variations. With the awareness of the in-plane residual stress and the temperature sensitivity, we perform design optimization to alleviate these non-ideal effects.

1.4 Dissertation Overview

The main objectives of this dissertation are a) to comprehensively model and characterize the non-ideal effects in RF MEMS tuners arising from fabrication uncertainties for accurate prediction of device performance, and b) to present design optimization strategies with the awareness that inevitable non-idealities will exist in RF MEMS tuners. The remaining of this dissertation is organized as follows:

Chapter 2 presents an equation-based nonlinear model for inclined supports in non-flat fixed-fixed beams. Practical fabrication processes often result in inclined beam supports which significantly influence the post-release performance of the beam. This chapter addresses this non-ideal effect and models the mechanical and electromechanical effects of inclined supports for the first time. Specifically, we calculate and validate the effects of residual stress and loading on the post-release beam behavior

including their nonlinear large-displacement characteristics. In addition the model accounts for non-flat beam profiles caused by residual stress and/or a non-flat sacrificial layer profile. The calculated beam displacements agree well with FEM models in both the linear and nonlinear regimes. Furthermore, this model is experimentally validated by comparing predicted beam displacements to measured results.

Chapter 3 reports on the extraction of residual stress in thin films of electrostatically actuated fixed-fixed beam structures using a wafer-scale technique. The nondestructive and automated measurements are taken at room temperature and directly at the beam itself without any additional test structures. Accurate extraction results are achieved by simultaneously incorporating non-idealities such as inclined supports, non-flat beam profiles and fringing fields in the reduced-order numerical model. Through the use of a custom scripting automation program, the geometries and displacement-voltage curves of fixed-fixed beams are measured using a confocal microscope. This technique has been demonstrated by applying it to wafer-scale measurements of nickel beams. The statistical distribution and the spatial distribution of residual stress over a 4-inch quarter wafer piece is presented. Detailed uncertainty analysis has been conducted, and it reveals that inaccurate modeling of the non-ideal effects, especially the non-flat profile and the inclined supports, results in significant errors in the extracted residual stress.

Following the residual stress characterization and discussion in Chapter 3, the design optimization of a MEMS diaphragm tuner for stress reduction is presented in Chapter 4. This MEMS diaphragm tuner is used in evanescent-mode cavity resonators/filters that require large tuning displacement. Attention has been paid to the nonlinear stretching behavior in the large displacement regime and the presence of residual stress. By introducing corrugations into the diaphragm design, stiffening effects caused by residual stress can be alleviated and the nonlinear stiffness of the diaphragm under large deflection can be greatly reduced by choosing appropriate corrugation geometries. With the aid of automated batch mode FEM simulations, a parametric study has been performed which reveals that the corrugation depth and

the corrugation range are the most important geometric parameters in corrugated diaphragm design. Using the linear and nonlinear stiffness coefficients extracted from simulations, the tradeoff between the pull-in voltage and the tuning range of the capacitive MEMS tuner has been analyzed. The systematic study of the effects of corrugation geometries on the pull-in voltage and the tuning range provides guidelines for design optimization.

Chapter 5 presents for the first time a thermally-stable capacitive MEMS tuner based on a circular nonuniform micro-corrugated diaphragm (NMCD) suitable for evanescent-mode resonators/filters which require a large tuning displacement ($>$ 10 μm). Through design optimization of the proposed NMCD by finite-element simulations, the temperature stability of the tuner can be greatly improved. Enhanced temperature stability allows the RF MEMS tuner to be continuously tunable in the full desired range with a greatly reduced variation of required actuation voltage. This design is experimentally validated by optical and electrostatic measurements with a temperature variation up to $\sim$ 100°C.

Chapter 6 summaries the work presented in this dissertation.

2. AN EQUATION-BASED NONLINEAR MODEL FOR INCLINED SUPPORTS IN NON-FLAT MEMS FIXED-FIXED BEAMS

2.1 Introduction

Surface micromachined fixed-fixed beams with anchor supports are widely used in many microstructures, such as switches [29, 30], filters [31, 32] and test devices for determination of thin-film material properties [24, 33–35]. Anchor supports of such beams are not always vertical as designed. Instead, they can be inclined as illustrated in Fig. 2.1(a). This is often due to the shape of the sacrificial layer during fabrication. For example, it has been proven that the topologies of the spin-on layers (e.g., photoresist) strongly depend on the process conditions. Consequently, the inclination angles at the edges of the patterned photoresist are highly dependent on baking temperature and time [36–39]. The inclination of these supports has nontrivial implications on performance metrics of beams, including, for example, the pull-in voltage of electrostatically actuated fixed-fixed beam switches [40, 41]. Furthermore, when the beam is used as a test structure, significant errors in extracting material properties may occur if the supports are not properly modeled. Therefore, the inclination of supports must be taken into account in beam modeling.

Several efforts have been made on studying the anchor compliance and on modeling supports as summarized in Table 2.1. All published equation-based approaches proposed for support modeling assumed vertical supports [42–45]. Mullen *et al.* modeled the vertical supports using a rotational spring and an axial spring [42, 43], and the values of the spring constants were obtained by matching a linear elastic model to finite-element-method (FEM) results. In [46], the response of the supports was modeled by an elastic matrix and its values were obtained by FEM simulations. The

elastic matrix was geometry-dependent, and therefore, FEM simulations were required for each beam with different geometries. Furthermore, the effects of the axial compliance on beam deflections were discussed only in the case that no external load was applied, and the non-flat initial beam shape were purely from the residual stress. The approach based on solving the entire beam and support structure by FEM simulations [47] can take into account the shape of the support, but it is computationally expensive. Another approach used a torsional stiffness as boundary conditions to model the rotational compliance but neglected the translational and axial compliance of the supports [33,45,48–50]. The boundary torsional stiffness was assumed constant and independent of load and residual stress. In [51], the boundary compliance was studied by assuming constant rotational stiffness and transversal spring stiffness as boundary conditions, but it didn't show how the boundary stiffness can be obtained.

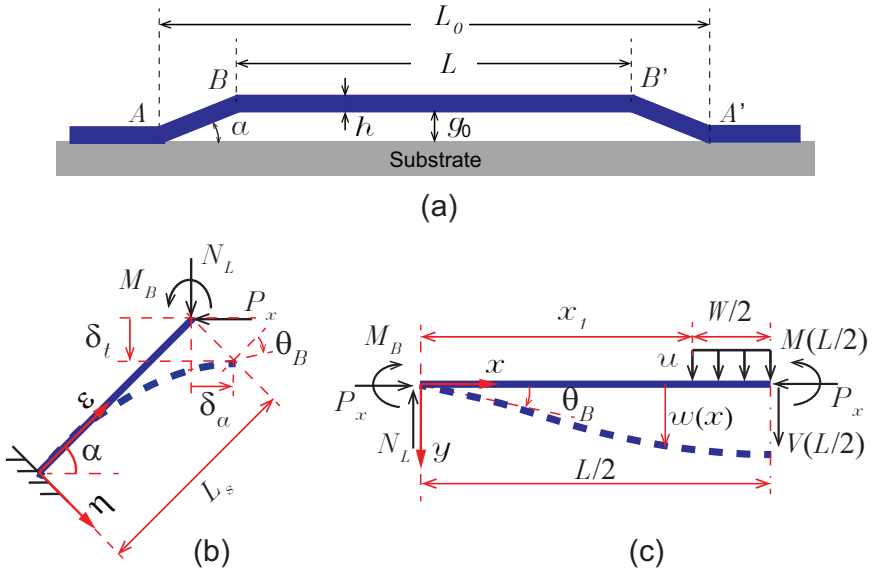

Fig. 2.1. (a) Schematic of a fixed-fixed beam with flat pre-release profile and inclined supports, (b) model for the inclined support, and (c) model for half of the horizontal beam.

The inclined supports shown in Fig. 2.1 and Fig. 2.2 are more realistic but have not been investigated yet in the literature. This chapter models the inclined supports in a fixed-fixed beam as two cantilevers coupled with a horizontal beam, as also pre-

Table 2.1.
Comparison of approaches for support modeling.

Features	This work	[42–44]	[45]	[46]	[47]	[48]	[49, 50]	[51]
Support inclination	✓							
Rotation support compliance	✓	✓	✓	✓	✓	✓	✓	✓
Axial support compliance	✓	✓		✓	✓			
Profile non-flatness due to residual stress	✓			✓	✓	✓	✓	✓
Profile non-flatness due to spin-on layer	✓				✓		✓	
Residual stress	✓			✓	✓	✓	✓	✓
Nonlinear beam stretching	✓		✓	✓	✓	✓	✓	✓
Mechanical loadings	✓	✓					✓	
Electromechanical loadings	✓		✓		✓		✓	✓
Reduced-order modeling without FE-needed information	✓		✓			✓	✓	✓

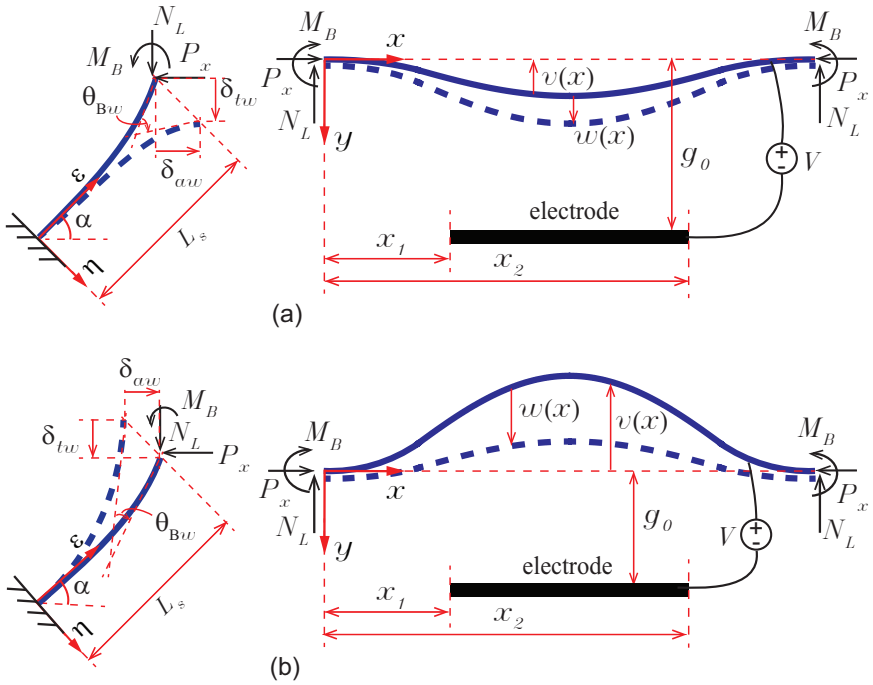

Fig. 2.2. Model for the inclined support and the electrostatically actuated beam with (a) an initially downward post-release profile, and (b) an initially upward post-release profile.

sented in [52]. Section 2.2 presents an inclined-support beam model suitable for beams with stress-induced non-flat profiles (i.e., flat pre-release profiles) and under purely mechanical loads (concentrated or distributed), as shown in Fig. 2.1. This model accounts for support compliance, stress-induced non-flat beam profile, and stretching nonlinearity associated with large-displacement. In addition, the support compliance in this case can be represented by a coupling matrix whose value depends solely on the material properties and the geometry of the supports. Base on the discussion in Section 2.2, Section 2.3 introduces a more advanced reduced-order electromechanical model that covers the more complicated case of arbitrary non-flat beam profiles (Fig. 2.2). Electrostatic forces and the resulting additional nonlinearities are also included in this second model. The rotational compliance of supports in this model is represented by a torsional stiffness that is employed in the Galerkin method for solving the beam model. Both models are compared to and verified by FEM simulations

in Section 2.4. Moreover, experimental data validate the electromechanical model in Section 2.5.

2.2 Mechanical Model for Beams with Inclined Supports and Stress-induced Non-flatness

Fig. 2.1(a) shows a fixed-fixed beam with inclined supports in its pre-release state. The beam has thickness h and width b, and it is deposited on a sacrificial layer with thickness of g_0. The design length of the beam is L_0, but the inclination of supports with with angle α shortens the effective beam length to L. Due to the residual stress developed during the beam deposition process, this beam will show a stress-induced non-flat profile after it is released. This section presents a mechanical model for beams with inclined supports and stress-induced non-flatness. Throughout the work, Euler-Bernoulli beam theory is used in the beam and support modeling.

2.2.1 Beam Model

The beam model accounts for the boundary compliance and the nonlinear dependence of the vertical deflection on the axial stress. Because of the symmetry, only half of the beam is modeled as shown in Fig. 2.1(c). The deflection of the beam $w(x)$ is described by the following coupled nonlinear integro-differential equations [46]:

$$\frac{\mathrm{d}^3 w}{\mathrm{d}x^3} + \beta^2 \frac{\mathrm{d}w}{\mathrm{d}x} = -\frac{V}{EI} \tag{2.1}$$

$$P_x = \frac{Ebh}{L}\left[2\delta_a - \int_0^{L/2}\left(\frac{\mathrm{d}w}{\mathrm{d}x}\right)^2 \mathrm{d}x\right] - \sigma_r bh \tag{2.2}$$

$$\beta = \sqrt{P_x/EI} \tag{2.3}$$

where $I = bh^3/12$ is the moment of inertia, $V(x)$ is the shear force, P_x is the axial force of the beam, δ_a is the node translation along x-axis at joint node B, and σ_r is the residual stress of the beam in the pre-release state. The axial force P_x includes the forces due to axial compliance of the supports, beam stretching, and residual stress.

For a wide beam ($b \geq 5h$), a plane strain condition is assumed by using an effective Young's modulus $E = E_0/(1-\nu^2)$, where E_0 is the Young's modulus and ν is the Poisson's ratio. For a narrow beam ($b < 5h$), $E = E_0$ [24].

The boundary conditions for half of the beam are as follows:

$$w\left(0\right) = \delta_t \tag{2.4}$$

$$\left.\frac{\mathrm{d}w}{\mathrm{d}x}\right|_{x=L/2} = 0 \tag{2.5}$$

$$\left(-EI\right)\left.\frac{\mathrm{d}^2w}{\mathrm{d}x^2}\right|_{x=0} = M_B \tag{2.6}$$

where δ_t is the translational displacement caused by the support compliance at the beam boundary and M_B is the reaction moment at the joint node B.

The deflection of the beam $w(x)$ described by (2.1) is solved for two symmetric loading conditions: the concentrated loading and the partially distributed uniform loading.

When the beam is loaded with a centered concentrated force F_L, the reaction force at the joint node B is $N_L = F_L/2$. The shear force is $V(x) = F_L/2$ for $0 \leq x < L/2$. For given constants P_x and β, the solution for the beam deflection takes the following form:

$$w(x) = C_1 \sin\left(\beta x\right) + C_2 \cos\left(\beta x\right) - \frac{N_L}{P_x}x + C_3 \tag{2.7}$$

where $C_1 - C_3$ are determined by the boundary conditions in (2.4) and their expressions are:

$$C_1 = \frac{\beta M_B \sin\left(\beta L/2\right) + N_L}{\beta P_x cos\left(\beta L/2\right)} \tag{2.8}$$

$$C_2 = \frac{M_B}{P_x} \tag{2.9}$$

$$C_3 = \delta_t - \frac{M_B}{P_x} \tag{2.10}$$

For a centered partially distributed uniform load with pressure u and span W, $N_L = ubW/2$, and the shear force is:

$$V(x) = \begin{cases} \dfrac{ubW}{2}, & \text{for } 0 \le x \le x_1 \\ \dfrac{ubW}{2} - ub\left(x - x_1\right), & \text{for } x_1 \le x \le \frac{L}{2} \end{cases} \tag{2.11}$$

where $x_1 = (L - W)/2$. Assuming that P_x and β are constant, we can derive the solution for the beam deflection as:

$$w(x) = \begin{cases} D_1 \sin\left(\beta x\right) \\ + D_2 \cos\left(\beta x\right) \\ - \dfrac{N_L}{P_x} x + D_3, & \text{for } 0 \le x \le x_1 \\ D_4 \sin\left[\beta\left(x - x_1\right)\right] \\ + D_5 \cos\left[\beta\left(x - x_1\right)\right] \\ + \dfrac{N_L}{WP_x}(x - x_1)^2 \\ - \dfrac{N_L}{P_x}(x - x_1) + D_6, & \text{for } x_1 \le x \le \frac{L}{2} \end{cases} \tag{2.12}$$

where the expressions for coefficients $D_1 - D_6$ can be solved based on the boundary conditions in (2.4) and the following equations which satisfy the continuity relationship of $w\left(x\right)$, $w'\left(x\right)$, and $w''\left(x\right)$ at the point $x = x_1$:

$$D_5 + D_6 = D_1 \sin\left(\beta x_1\right) + D_2 \cos\left(\beta x_1\right) - \frac{N_L}{P_x} x_1 + D_3 \tag{2.13}$$

$$\beta D_4 - \frac{N_L}{P_x} = \beta D_1 \cos\left(\beta x_1\right) - \beta D_2 \sin\left(\beta x_1\right) - \frac{N_L}{P_x} \tag{2.14}$$

$$\beta^2 D_5 - \frac{2N_L}{WP_x} = \beta^2 D_1 \sin\left(\beta x_1\right) + \beta^2 D_2 \cos\left(\beta x_1\right) \tag{2.15}$$

By solving the boundary conditions in (2.4) and (2.13), we can obtain $D_1 - D_6$ as follows:

$$D_1 = \frac{2N_L \sin(\beta W/2) + M_B W \beta^2 \sin(\beta L/2)}{\beta^2 W P_x \cos(\beta L/2)} \tag{2.16}$$

$$D_2 = \frac{M_B}{P_x} \tag{2.17}$$

$$D_3 = \delta_t - \frac{M_B}{P_x} \tag{2.18}$$

$$D_4 = \frac{\sin(\beta W/2)}{\beta^2 W P_x \cos(\beta L/2)} \times \left[2N_L \cos\left(\frac{\beta L - \beta W}{2}\right) + \beta^2 W M_B\right] \tag{2.19}$$

$$D_5 = \frac{N_L}{\beta^2 W P_x} + \frac{N_L \cos(\beta L/2 - \beta W) + \beta^2 M_B W \cos(\beta W/2)}{\beta^2 W P_x \cos(\beta L/2)} \tag{2.20}$$

$$D_6 = \delta_t - \frac{2M_B + (L - W) N_L}{2P_x} - \frac{2N_L}{\beta^2 W P_x} \tag{2.21}$$

2.2.2 Model for Inclined Supports

A new coordinate system is defined for the inclined support as shown in Fig. 2.1(b). The support is modeled as a cantilever with inclination angle α. The length of the support L_s equals $(g_0 + h/2)/\sin(\alpha)$. The following coupled integro-differential equations describe the behavior of the inclined support:

$$\frac{\mathrm{d}^3\eta}{\mathrm{d}\varepsilon^3} + \gamma^2 \frac{\mathrm{d}\eta}{\mathrm{d}\varepsilon} = -\frac{V_\eta}{EI} \tag{2.22}$$

$$V_\eta = -P_x \sin(\alpha) + N_L \cos(\alpha) \tag{2.23}$$

$$P_\varepsilon = P_x \cos(\alpha) + N_L \sin(\alpha) \tag{2.24}$$

$$\gamma = \sqrt{P_\varepsilon / EI} \tag{2.25}$$

where $\eta(\varepsilon)$ is the deflection of the supports along η-axis, and P_ε and V_η are the forces acting on the support along ε-axis and η-axis, respectively. The support is fixed in

one end, and loaded with force P_ε, V_η, and moment M_B at the other end. Therefore, it is subjected to the following boundary conditions:

$$\eta\left(0\right) = 0 \tag{2.26}$$

$$\left.\frac{\mathrm{d}\eta}{\mathrm{d}\varepsilon}\right|_{\varepsilon=0} = 0 \tag{2.27}$$

$$\left(-EI\right)\left.\frac{\mathrm{d}^2\eta}{\mathrm{d}\varepsilon^2}\right|_{\varepsilon=L_s} = M_B \tag{2.28}$$

When V_η, P_ε and γ are assumed constant, the solution for the deflection of the inclined support is:

$$\eta(\varepsilon) = A_1 \sin\left(\gamma\varepsilon\right) + A_2 \cos\left(\gamma\varepsilon\right) - \frac{V_\eta}{P_\varepsilon}\varepsilon + A_3 \tag{2.29}$$

where $A_1 - A_3$ are constant coefficients determined by the boundary conditions in (2.26), and are given by:

$$A_1 = \frac{V_\eta}{\gamma P_\varepsilon} \tag{2.30}$$

$$A_2 = \frac{\gamma M_B - V_\eta \sin\left(\gamma L_s\right)}{\gamma P_\varepsilon \cos\left(\gamma L_s\right)} \tag{2.31}$$

$$A_3 = \frac{-\gamma M_B + V_\eta \sin\left(\gamma L_s\right)}{\gamma P_\varepsilon \cos\left(\gamma L_s\right)} \tag{2.32}$$

However, in most practical cases, the support length L_s is considerably smaller than the beam length L, and consequently the small deflection assumption holds for the support. Therefore, the effect of the axial force on the inclined support can be neglected by discarding the second term on the left-hand side of (2.22). With this simplication, the solution for the support deflection becomes:

$$\eta(\varepsilon) = -\frac{V_\eta}{6EI}\varepsilon^3 + B_1\varepsilon^2 + B_2\varepsilon + B_3 \tag{2.33}$$

where $B_1 - B_3$ are determined by the boundary conditions in (2.26) and are as follows:

$$B_1 = \frac{V_\eta L_s - M_B}{2EI} \tag{2.34}$$

$$B_2 = 0 \tag{2.35}$$

$$B_3 = 0 \tag{2.36}$$

2.2.3 Coupling Between Beam and Supports

The deformation of the inclined supports at the joint points B and B' (where the horizontal beam connects with the supports) indicates the boundary compliance of the horizontal beam. The beam and the inclined supports are coupled by the continuity relationships at the joint node B as follows:

$$\delta_a = \eta\left(L_s\right)\sin\alpha \tag{2.37}$$

$$\delta_t = w\left(0\right) = \eta\left(L_s\right)\cos\alpha \tag{2.38}$$

$$\theta_B = \left.\frac{\mathrm{d}w}{\mathrm{d}x}\right|_{x=0} = \left.\frac{\mathrm{d}\eta}{\mathrm{d}\varepsilon}\right|_{\varepsilon=L_s} \tag{2.39}$$

where δ_a, δ_t and θ_B are the axial, translational and rotational deformations at the beam boundary. By substituting (2.29) into (2.37) and reordering the equations, we define a coupling matrix K_{ij} as:

$$\begin{bmatrix} \delta_a \\ \delta_t \\ \theta_B \end{bmatrix} = \begin{bmatrix} K_{11} & -K_{11}\tan\left(\alpha\right) & K_{13} \\ \dfrac{K_{11}}{\tan\left(\alpha\right)} & -K_{11} & \dfrac{K_{13}}{\tan\left(\alpha\right)} \\ \dfrac{-K_{13}}{\tan\left(\alpha\right)} & K_{13} & K_{33} \end{bmatrix} \begin{bmatrix} N_L \\ P_x \\ M_B \end{bmatrix} \tag{2.40}$$

where

$$K_{11} = \frac{\tan\left(\gamma L_s\right) - \gamma L_s}{\gamma P_\varepsilon}\sin\left(\alpha\right)\cos\left(\alpha\right) \tag{2.41}$$

$$K_{13} = -\frac{1-\cos\left(\gamma L_s\right)}{P_\varepsilon\cos\left(\gamma L_s\right)}\sin\left(\alpha\right) \tag{2.42}$$

$$K_{33} = -\frac{\gamma\sin\left(\gamma L_s\right)}{P_\varepsilon\cos\left(\gamma L_s\right)} \tag{2.43}$$

For given α, there are only three independent parameters K_{11}, K_{13} and K_{33} in the coupling matrix. The coupling matrix can be simplified as follows if (2.33) is used instead of (2.29):

$$K_{11}^{0} = \frac{L_s^3}{3EI}\sin(\alpha)\cos(\alpha) \tag{2.44}$$

$$K_{13}^{0} = -\frac{L_s^2}{2EI}\sin(\alpha) \tag{2.45}$$

$$K_{33}^{0} = -\frac{L_s}{EI} \tag{2.46}$$

In (2.44), the coupling matrix is independent of external load and the axial force, and it is only determined by the material properties and the support geometry. This simplification makes the inclined support model applicable to the electromechanical beam model as detailed in the following section.

From (2.1) and (2.22), we notice that the axial force P_x, and consequently β, γ, V_η, and P_ε are nonlinearly coupled with the beam deflection $w(x)$. To solve the system of nonlinear integro-differential equations, one can use graphical method as follows. First, P_x is assigned with a trial value. The value of β, γ, V_η and P_ε are related to P_x by (2.1c) and (2.22b-2.22d), respectively. Second, M_B can be obtained by solving (2.37c), and δ_a, δ_t and θ_B are calculated by (2.40). Then, the beam deflection $w(x)$ is calculated using (2.7) for a concentrated load or (2.12) for a distributed load. The calculated δ_a and $w(x)$ are used in return to compute the axial force P_x using (2.1b). When the difference between the resulting value of P_x and the assigned value satisfies a given accuracy constraint (0.5% is used here), this value of P_x is taken to be the solution for P_x, and the final solution of the beam deflection $w(x)$ is obtained. Although P_x and P_ε are assumed positive (i.e., β and γ are real), the solution for the beam deflection $w(x)$ is valid for both positive and negative axial force since the sine and cosine functions can be converted to their hyperbolic counterparts when β and γ are imaginary.

Although the beam model is solved for symmetric loadings (concentrated or distributed), which are the most common cases in MEMS fixed-fixed beam applications, this approach can be applied to more general non-symmetric loading cases by using different boundary conditions. Without symmetry, the symmetric condition for the beam in (2.4) needs to be substituted by the boundary condition of the beam at

$x = L$. Additional integro-differential equations as in (2.22) need to be added for modeling the other support. Moreover, the solutions must satisfy the continuity relationships of $w(x)$, $w'(x)$, and $w''(x)$ at the point where the nonsymmetric loading is applied. By applying the same procedures described in the previous paragraph, the solutions for non-symmetric loading can be obtained.

2.3 Electromechanical Model for Beams with Inclined Supports and Arbitrary Non-flatness

Besides the stress-induced curvature, non-flat beam profiles may also result from uneven sacrificial layers. In our case, the unevenness of the sacrificial layer is caused by the electrode underneath the beam for electrostatic actuation. This section develops an reduced-order electromechanical model for beams with inclined supports and arbitrary shaped profiles.

2.3.1 Electromechanical Beam Model

The beam model is adapted from a reduced-order numerical model by Snow and Bajaj [49, 50]. Snow's model accounts for a variety of non-ideal conditions, including: boundary torsional compliance, nonlinear stretching, initial stress, initial profile, electrostatic fringing field, and finite electrodes. However, the axial compliance of the supports is neglected and it assumes a priori knowledge of the boundary torsional stiffness. The adapted model accurately predict the static behaviors of beams electrostatically actuated by taking into account the axial compliance of the supports, and using the boundary conditions provided by the support model as discussed in Section 2.2.

As shown in Fig. 2.2, $w(x)$ is defined as the relative vertical displacement from its post-release position $v(x)$, instead of its pre-release position as in Section 2.2. The beam deflection is described by the following coupled integro-differential equations:

$$
\begin{aligned}
& EI\frac{\mathrm{d}^4 w}{\mathrm{d}x^4} + P_w\left(\frac{\mathrm{d}^2 w}{\mathrm{d}x^2} - \frac{\mathrm{d}^2 v}{\mathrm{d}x^2}\right) - N_0\frac{\mathrm{d}^2 w}{\mathrm{d}x^2} \\
= \quad & \frac{\epsilon_0 b V^2}{2\left(g_0 + v - w\right)^2}\left[1 + 0.24A_0\left(g_0 + v - w\right)^{0.76}\right] \\
& \times \left[H\left(x - x_1\right) - H\left(x - x_2\right)\right] \qquad (2.47)
\end{aligned}
$$

$$
\begin{aligned}
P_w = & \frac{2Ebh}{L}\delta_{aw} - \frac{Ebh}{2L} \\
& \times \int_0^L \left[\left(\frac{\mathrm{d}w}{\mathrm{d}x}\right)^2 - 2\left(\frac{\mathrm{d}w}{\mathrm{d}x}\right)\left(\frac{\mathrm{d}v}{\mathrm{d}x}\right)\right]\mathrm{d}x \qquad (2.48)
\end{aligned}
$$

$$N_0 = \sigma_0 bh \qquad (2.49)$$

$$A_0 = 0.85\frac{1}{b^{0.76}} + 2.5\frac{h^{0.24}}{b} \qquad (2.50)$$

where P_w is the axial force from the nonlinear stretching of the beam and from the axial compliance δ_{aw} at the beam boundary. The force N_0 from the initial stress σ_0 keeps the beam in a stable position $v\left(x\right)$ after the beam is released. The total axial force is $P_x = P_w - \sigma_0 bh$. It is worth to notice that the initial stress σ_0 in the post-release beam is smaller in magnitude than the residual stress σ_r in its pre-release state, since the beam deflects vertically when it is released and the stress is relaxed. The Heaviside step functions in (2.47a) describe the finite electrode under the beam spanning from x_1 to x_2. V is the actuation voltage applied, and ϵ_0 is the permittivity of free space. The beam profile with arbitrary non-flatness is described by a Fourier series:

$$v\left(x\right) \approx \sum_{i=1}^{M} p_i \sin\left(i\pi x\right) \qquad (2.51)$$

where the sine series has been chosen to approximate a non-zero derivative of $v\left(x\right)$ at beam boundaries, and the coefficients p_i are:

$$p_i = 2\int_0^1 v\left(x\right)\sin\left(i\pi x\right)dx \qquad (2.52)$$

Non-dimensional variables are introduced to make (2.47) more convenient to solve, and are defined as follows:

$$\begin{aligned} \hat{x} &= \frac{x}{L},\ \hat{x}_1 = \frac{x_1}{L},\quad \hat{x}_2 = \frac{x_2}{L}, \\ \hat{w} &= \frac{w}{g_0},\ \hat{v} = \frac{v}{g_0},\ \hat{\delta}_{aw} = \frac{\delta_{aw}}{L}. \end{aligned} \tag{2.53}$$

Substituting (2.53) into (2.47), we obtain:

$$\begin{aligned} & EI\frac{\mathrm{d}^4\hat{w}}{\mathrm{d}\hat{x}^4} - \hat{N}_0\frac{\mathrm{d}^2\hat{w}}{\mathrm{d}\hat{x}^2} + \left(\frac{\mathrm{d}^2\hat{w}}{\mathrm{d}\hat{x}^2} - \frac{\mathrm{d}^2\hat{v}}{\mathrm{d}\hat{x}^2}\right) \\ & \times \left\{\alpha_0\hat{\delta}_{aw} - \alpha_1\int_0^1\left[\left(\frac{\mathrm{d}\hat{w}}{\mathrm{d}\hat{x}}\right)^2 - 2\left(\frac{\mathrm{d}\hat{w}}{\mathrm{d}\hat{x}}\right)\left(\frac{\mathrm{d}\hat{v}}{\mathrm{d}\hat{x}}\right)\right]\mathrm{d}\hat{x}\right\} \\ & = \frac{\alpha_2 V^2}{2\left(1+\hat{v}-\hat{w}\right)^2}\left[1 + A_1\left(1+\hat{v}-\hat{w}\right)^{0.76}\right] \\ & \quad \times \left[H\left(\hat{x}-\hat{x}_1\right) - H\left(\hat{x}-\hat{x}_2\right)\right] \end{aligned} \tag{2.54}$$

where

$$\begin{aligned} \alpha_0 &= \frac{24L^2}{h^2},\ \ \alpha_1 = \frac{6g_0^2}{h^2}, \qquad \alpha_2 = \frac{6\epsilon_0 L^4}{Eh^3 g_0^3} \\ \hat{N}_0 &= \frac{N_0 L^2}{EI}, \qquad\qquad\qquad A_1 = 0.24A_0 g_0^{0.76} \end{aligned} \tag{2.55}$$

To solve the integro-differential equations in (2.54), they are rendered them into a system of ordinary differential equations by utilizing global basis functions using the Galerkin method [50]. It is assumed that the solution for the beam model is a linear combination of the translational displacement from the support compliance and the linear mode shapes of the undamped, straight beam, as follows:

$$\hat{w}\left(x\right) \approx \hat{\delta}_{tw} + \sum_{i=1}^{M} u_i\phi_i\left(x\right) \tag{2.56}$$

where $\hat{\delta}_{tw} = \delta_{tw}/g_0$, and $\phi_i\left(x\right)$ is the ith linear undamped mode shape of the beam, and governed by:

$$\frac{\mathrm{d}^4\phi_i}{\mathrm{d}\hat{x}^4} = \hat{N}\frac{\mathrm{d}^2\phi_i}{\mathrm{d}\hat{x}^2} + \omega_i^2\phi_i \tag{2.57}$$

where ω_i is the ith natural frequency. The boundary conditions for solving (2.57) and (2.54) are required to be applicable to the Galerkin method and also to satisfy the beam-support coupling as discussed below.

2.3.2 Coupling between Beam and Supports

The support deformation is calculated using the same model presented in Section 2.2.2. However, the coupling relationships need to be modified for the electromechanical beam model. As shown in Fig. 2.2, when the beam rests at its initial post-release position $v(x)$ before being actuated, the deformed beam and supports are in equilibrium with $N_L = 0$, $P_x = -\sigma_0 bh$ and $M_B = M_{B0}$. When the beam is actuated by an electrostatic force F_e, the beam and the support deflect to a new stable position with $N_L = F_e/2$, $P_x = -\sigma_0 bh + P_w$ and $M_B = M_{B0} + M_w$. P_w and M_w are the axial force and moment resulting from the relative beam deflection $w(x)$, respectively. P_w is given by (2.47b), and $M_w = -EIw''(0)$. δ_{aw}, δ_{tw}, and θ_{Bw} are defined to denote the relative axial displacement, translational displacement and angle rotation away from the initial position of the support, respectively. Since the simplified coupling matrix in (2.44) is independent of external load and the axial force,the relative displacement and rotation of the support can be calculated as follows without knowing the initial position of the support:

$$\begin{bmatrix} \delta_{aw} \\ \delta_{tw} \\ \theta_{Bw} \end{bmatrix} = \begin{bmatrix} K_{11}^0 & -K_{11}^0 \tan(\alpha) & K_{13}^0 \\ \dfrac{K_{11}^0}{\tan(\alpha)} & -K_{11}^0 & \dfrac{K_{13}^0}{\tan(\alpha)} \\ \dfrac{-K_{13}^0}{\tan(\alpha)} & K_{13}^0 & K_{33}^0 \end{bmatrix} \begin{bmatrix} N_L \\ P_w \\ M_w \end{bmatrix} \tag{2.58}$$

where N_L is the reaction force when an actuation voltage V is applied:

$$N_L = \frac{\epsilon_0 bV^2}{4} \int_0^L \frac{1 + 0.24A_0 (g_0 + v - w)^{0.76}}{(g_0 + v - w)^2} \mathrm{d}x \tag{2.59}$$

The beam deflection $w(x)$ satisfies the coupling relationships between the beam and the support as follows:

$$\begin{aligned} w(0) = w(L) &= \delta_{tw} \\ \left.\frac{\mathrm{d}w}{\mathrm{d}x}\right|_{x=0} = -\left.\frac{\mathrm{d}w}{\mathrm{d}x}\right|_{x=L} &= \theta_{Bw} \end{aligned} \tag{2.60}$$

However, the Galerkin method used for solving the beam deflection $w(x)$ requires the boundary conditions to be applicable to each mode shape and also their linear

combination. Therefore, (2.60) cannot be directly used. To adapt to the Galerkin method, a boundary torsional stiffness k_T is defined to present the rotational compliance of the supports:

$$k_T = -\frac{M_w}{\theta_{Bw}} \tag{2.61}$$

Therefore, the non-dimensional boundary conditions for solving (2.57) is:

$$\begin{aligned} \phi_i(0) = 0, \qquad & \phi_i(1) = 0 \\ \phi_i''(0) = \frac{Lk_T}{EI}\phi_i'(0), \; & \phi_i''(1) = -\frac{Lk_T}{EI}\phi_i'(1) \end{aligned} \tag{2.62}$$

which guarantees that the non-dimensional beam displacement $\hat{w}$ satisfies:

$$\begin{aligned} \hat{w}(0) = \hat{\delta}_{tw} \qquad & \hat{w}(1) = \hat{\delta}_{tw} \\ \hat{w}''(0) = \frac{Lk_T}{EI}\hat{w}'(0), \; & \hat{w}''(1) = -\frac{Lk_T}{EI}\hat{w}'(1) \end{aligned} \tag{2.63}$$

We will show in Section 2.5 that the boundary torsional stiffness k_T for inclined supports is not only a function of the beam's material properties and geometries, but is also associated with the electrostatic loading.

2.4 Results and Discussion

In this section, the numerical results of the mechanical model described in Section 2.2 and the electromechanical model described in Section 2.3 are presented. The accuracy of the numerical results is verified by comparing to FEM simulations under different loading conditions.

2.4.1 Results for Beams with Inclined Supports and Stress-induced Non-flatness

The stress-induced non-flat profiles are calculated by the model presented in Section 2.2 for a 400-μm-long beam with inclined supports ($\alpha = 10°$) and are plotted in Fig. 2.3(a). By referring to Fig. 2.3(b), the vertical deflection of the beam relaxes the residual stress. When the beam is under a compressive stress, the beam has larger

stress-induced deflection compared with the case of a tensile stress with the same magnitude, and consequently, more stress relaxation.

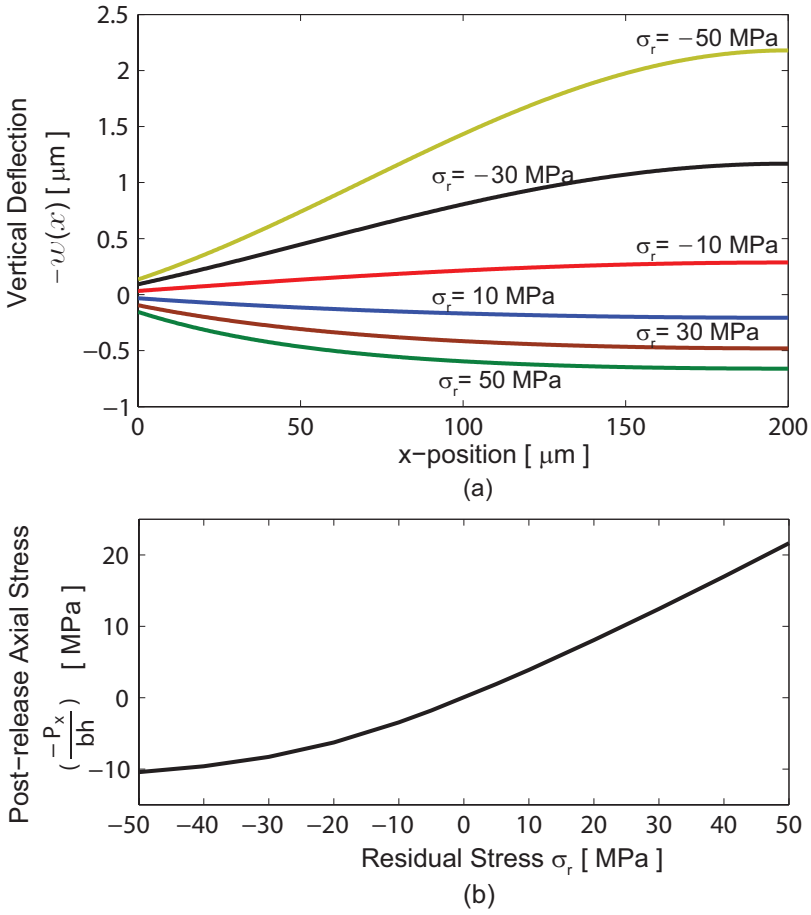

Fig. 2.3. (a) Post-release beam shapes caused by different residual stresses, and (b) post-release axial stress v.s. residual stress, for a 400-μm-long beam ($h = 2$ μm, $b = 120$ μm, $g_0 = 3$ μm, $\alpha = 10°$).

The simplification made for the coupling matrix is verified by comparing the K_{ij} values and the beam displacements when (2.41) and (2.44) are used, respectively. As shown in Fig. 2.4(a), the differences of the coupling parameters in (2.41) and (2.44) are less than 4.0% for residual stress ranging from −30 MPa to 30 MPa. The beam displacements calculated using the coupling parameters in (2.41) only differ from the results calculated using (2.44) by 0.72%, as shown in Fig. 2.4(b), which indicates that

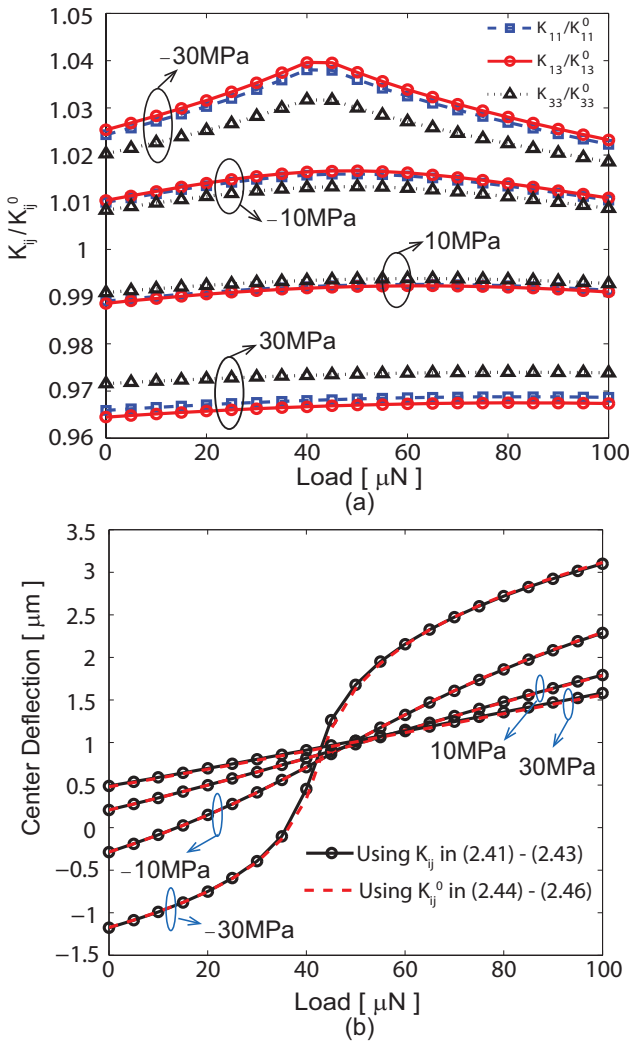

Fig. 2.4. (a) Calculated results of coupling parameters. (K_{ij} and K_{ij}^0 are shown in (2.41)-(2.43) and (2.44)-(2.46), respectively.) (b) Calculated results of displacement versus load curves by using different coupling parameters in (2.41)-(2.43) and (2.44)-(2.46), respectively. ($L = 400$ μm, $\alpha = 10°$, $h = 2$ μm, $b = 120$ μm, $g_0 = 3$ μm. The beam deflects under a distributed load with $W = 270$ μm)

coupling parameters can be simplified by using (2.44). Therefore, (2.44) is used in the following calculations.

For beams with stress-induced non-flat profiles, the commercially available finite-element software ANSYS [53] is utilized to simulate the deflection curves in both linear and nonlinear regimes. The beams are assumed to be subjected to imperfect

fabrication processes resulting in varying degrees of support inclination and thus varying effective beam lengths. The other dimensions are assumed to remain the same as designed. Therefore, we study the effects of the inclined supports by examining beams with their different inclination angles and different lengths as listed in Table 2.2. The beam width b and the span of pressure W in the case of distributed loading are assumed to scale proportionally to the beam length. The beams are made of nickel which has Young's modulus of $E_0 = 200$ GPa, Poisson's ratio of $\nu = 0.3$ and density of 8910 kg/m^3 [54]. A residual stress of -10 MPa is assumed for all beams. We use a 3-D 3-Node beam element BEAM 189 which includes the nonlinear effects of the axial stress due to residual stress and large displacements.The inclined supports and the horizontal beam are meshed with 50 and 200 beam elements, respectively, and nonlinear analyses are performed.

Table 2.2.
Beam dimensions for FEM simulations.

α	L [μm]	g_0 [μm]	h [μm]	b [μm]	W [μm]
10°/45°/90°	200	3	2	60	135
	400	3	2	120	270
	600	3	2	180	405

The beam deflection curves in both linear and nonlinear regimes are plotted and compared to FEM results for concentrated load in Fig. 2.5 (a)-(c), and for distributed load in Fig. 2.5 (d)-(f). Since the axial force P_x is solved numerically by assuming an accuracy constraint (0.5% in this model), the sensitivity of displacements to P_x is studied, which shows the displacement variation is $< 0.2\%$ when P_x changes by 0.5%. The predicted results from the beam model match the FEM results well with an average error of 1.1%. The effect of the support inclination manifests itself in the beam deflections as plotted in Fig. 2.5, and is explained as follows. When inclination angle of supports (α) is the only variable geometry, the boundary compliance and the

post-release stress change with the support inclination. The boundary compliance increases with α reduces according to (2.40) and (2.44), which leads to a larger beam deflection. On the other hand, the increased boundary compliance relaxes more compressive residual stress and leads to a smaller beam deflection. For short beams as in Fig. 2.5 (a) and (d), the increase of boundary compliance is dominant over the stress-relaxation, and therefore, beams with smaller α have larger deflections. However, for long beams as in Fig. 2.5 (c) and (f), the stress-relaxation is more dominant and beams with smaller α deflect less. It can be noticed from Fig. 2.5 that the stress-relaxation increases with longer beams and causes a larger stress-induced initial deflection which may cause bifurcation in the deflection curves. As shown in Fig. 2.5(c) and (f), bifurcation occurs in the calculated deflection curves, which show multiple solutions of beam displacement for a given load. However, the solutions plotted with the dashed lines are unstable, and when the load increases to a critical value, the beam will snap to the next stable position, which is referred to as the "snap-through" phenomenon [50]. For beams with all lengths, the effects of the support inclination are more prominent for shallow inclination angles ($\alpha < 45°$). From the analyses of the beam deflection curves, physical insights can be gained into the effects of the support inclination on the boundary compliance and axial stress state in the beam.

2.4.2 Results for Electrostatically Actuated Beams with Inclined Supports and Arbitrary Non-flatness

To verify the electromechanical model for beams with non-flat profiles, a full 3-D electromechanical simulation is performed in CoventorWare [55]. The beam is made of nickel with the same material properties as described in Section 2.4.1, and it has an initial stress (σ_0) of -8.2 MPa. Its dimensions are the same as the 400-μm-long beam in Table 2.2 with $\alpha = 10°$. The gold electrode is 270-μm wide, and it is covered with a 0.2-μm-thick silicon nitride film. The beam and the electrode are meshed with

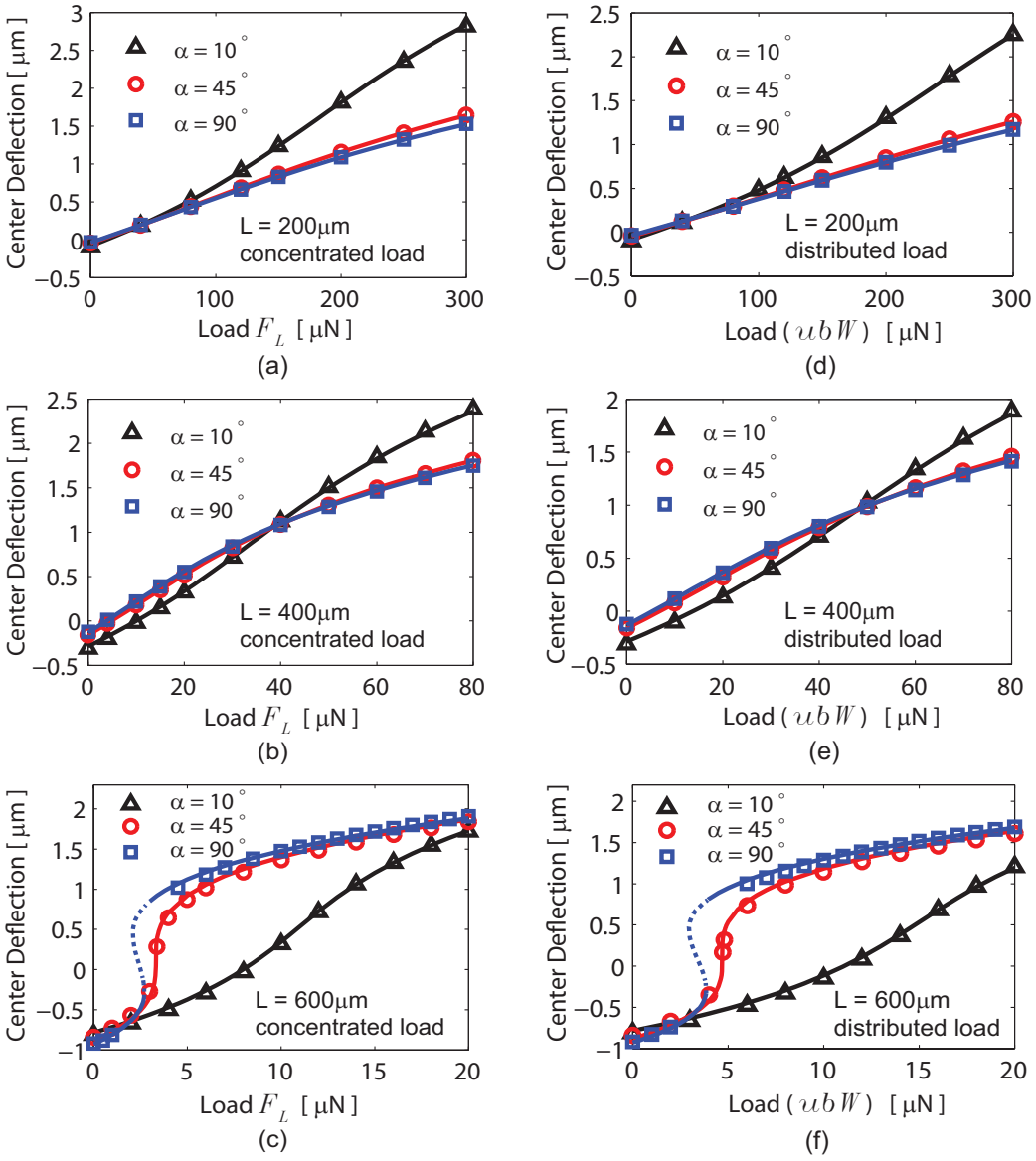

Fig. 2.5. Simulated deflection versus load curves for beams with (a), (d) L = 200μm, (b), (e) L = 400μm, (c), (f) L = 600μm. A compressive residual stress $\sigma_r = -10$ MPa is assumed. (a) - (c) are for concentrated load at the center of the beam, and (d) - (f) are for the partially distributed uniform load. The points represent ANSYS simulation results, and the solid lines represent results of the analytical model described in Section 2.2.

Manhattan brick elements with a size of 5μm × 5μm × 0.5μm. Fig. 2.6(a) shows the CoventorWare model, and the initially non-flat profile of the beam including the

inclined supports is recorded along the x-direction as plotted in Fig. 2.6(b). Since the beam profile is symmetric, only odd terms of the Fourier series are nontrivial. The approximated profiles of the horizontal beam with different numbers of Fourier modes using (2.51) are compared in Fig. 2.6(c), which shows that the beam profile can be accurately described by three Fourier modes (also see Fig. 2.7(a)).

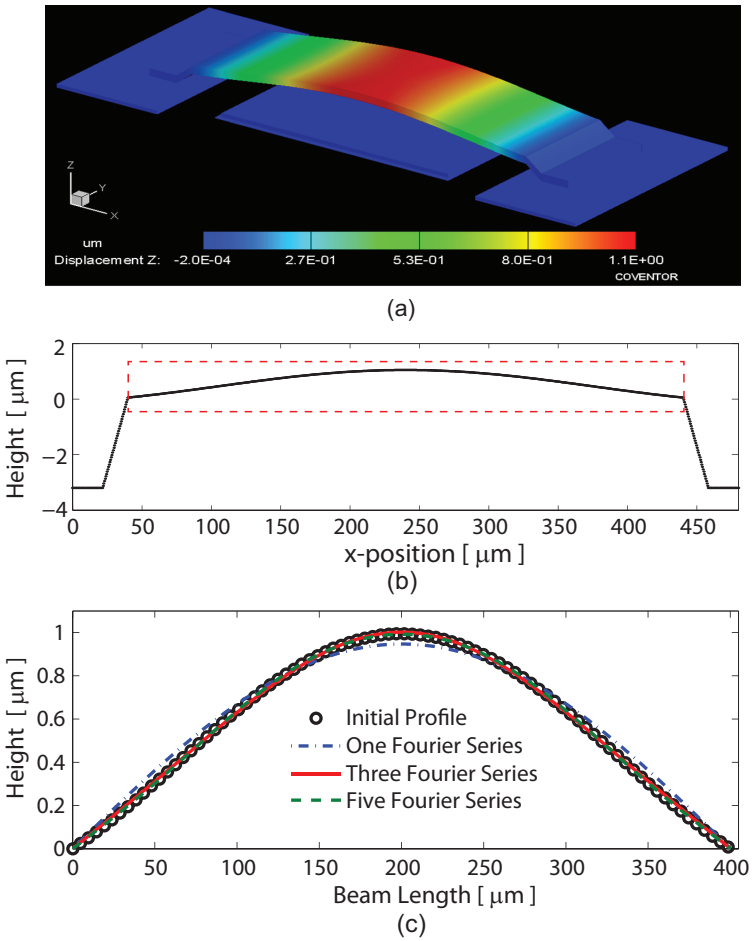

Fig. 2.6. (a) Model for beam with non-flat profile in CoventorWare [55], (b) initial profile of the beam, and (c) the approximated profiles of the horizontal beam in the red dashed box in (b) with different numbers of Fourier modes using (2.51).

The displacement-voltage curve from the electromechanical simulations in CoventorWare is plotted in Fig. 2.7(a), which predicts a pull-in voltage of 41.25 V. The displacement-voltage relationship is also calculated numerically using the model in

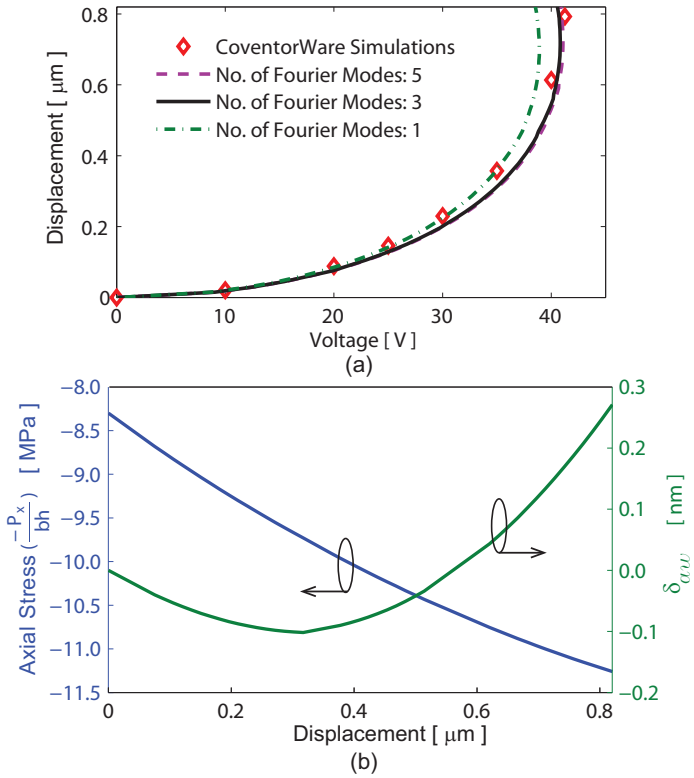

Fig. 2.7. (a) Calculated displacement vs. voltage curves compared to FEM simulations, and (b) axial stress vs. displacements.

Section 2.3 by employing different numbers of Fourier modes for describing the beam profile. As shown in Fig. 2.7(a), the numerical results reach convergence when three Fourier modes are used and the predicted pull-in voltage is 40.83 V, which agrees with the FEM results within 1.0%. Fig. 2.7(b) shows the total axial stress and the axial stress caused by the axial displacement of the support (δ_{tw}). The axial and translational displacements of the inclined supports are in the order of nanometers. However, an axial displacement of 1 nm corresponds to 0.52 MPa axial stress for a 400-μm-long beam. The change of axial stress due to the axial displacement is larger for short beams. Therefore, the axial compliance of the supports needs to be modeled, especially for short beams with low initial stress.

The reduced-order electromechanical model is more computationally efficient compared to FE simulations. For the beam in Fig. 2.6, the CoventorWare simulation

needs 28 minutes, while our reduced-order model only takes 1.9 minutes to obtain the displacement-voltage curve, which shows an improvement of 15× for the computational efficiency. In addition, the FE method requires extra time for building the 3D model, while our numerical model can automatically read in the geometrical data for simulations.

2.5 Experimental Results

In this section, the electromechanical model described in Section 2.3 is experimentally validated by applying it for the analysis of electrostatically actuated MEMS beams with inclined supports and non-flat profiles.

2.5.1 Fabrication Process and Measurements

The microbeams under test, as shown in Fig. 2.8, are fabricated on a p-type high-resistivity oxidized silicon substrate with a 500-nm-thick thermally grown silicon-dioxide film [56]. First, a 1-μm-thick Au film is sputtered and lifted-off to define the actuation electrodes and electrical connections of the beam. Then, a 0.2-μm-thick silicon nitride film is deposited and patterned to cover the actuation electrodes. The anchors are then patterned through a 3-μm-thick photoresist sacrificial layer. The sacrificial layer is hard baked at 190°C for 5 minutes. After a seed-layer of 50-nm sputtered Ti and 30-nm evaporated Ni is deposited on the whole sample, a 6-μm-thick photoresist layer is shaped to form the electroplating mold on the seed layer. The Ni electroplating is carried out in a nickel-sulfamate bath with pH value of 4 at 50°C. A 2-μm-thick Ni layer is selectively electroplated on the seed layer based on the photoresist mold. After the removal of the photoresist mold, the Ni and Ti seed layers are stripped with $HCl : H_2O = 1 : 1$ and $HF : H_2O = 1 : 20$ at room temperature, respectively. The photoresist sacrificial layer is removed by immersion in photoresist-stripper-2000 at 75°C for 24 hours. Finally, the fabrication process

is completed by drying in a critical-point-dryer. Beams with two different lengths (400 μm and 500 μm) are fabricated with the same width of 120 μm.

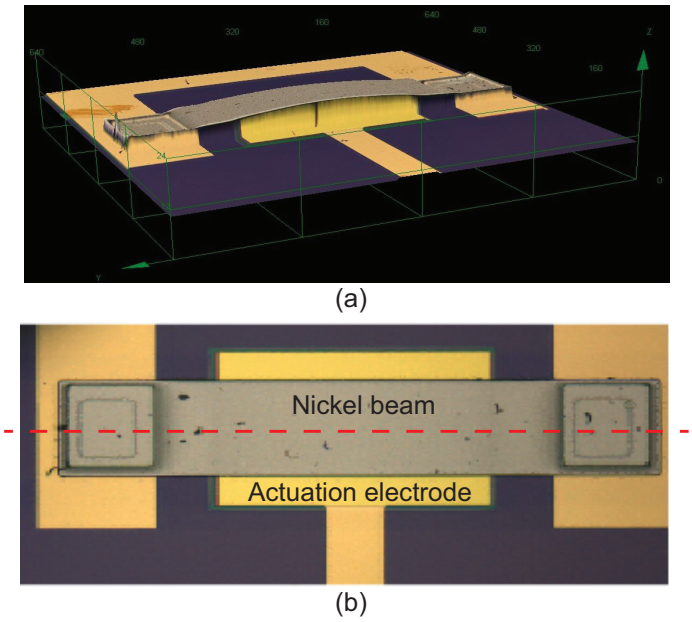

Fig. 2.8. (a) 3-D confocal-microscopy image, and (b) top view confocal-microscopy image of a fixed-fixed beam with inclined supports.

The ideal patterned photoresist layer shown in Fig. 2.9(a) is conformal with the underlying topology. However, the actual topology of photoresist sacrificial layer critically depends on the process conditions, and the inclination angles at the edges of the patterned photoresist are highly dependent on baking temperature and time [36–39]. The actual shape of the photoresist layer after reflow is suggested by Fig. 2.9(b), and the beam deposited on top follows this shape.

The geometric parameters are measured optically using a confocal laser scanning microscope LEXT OLS3100 from Olympus [57], which creates a high-quality 3-D image of the measured device by scanning discrete planes along z-axis with a lateral resolution of $\pm$ 60 nm. For a 20$\times$ objective with a numerical aperture of 0.46 used in our measurement, a vertical resolution of $\sim \pm$ 20 nm can be expected [58]. Higher resolution is available with higher magnification objectives, but the 20$\times$ objective is

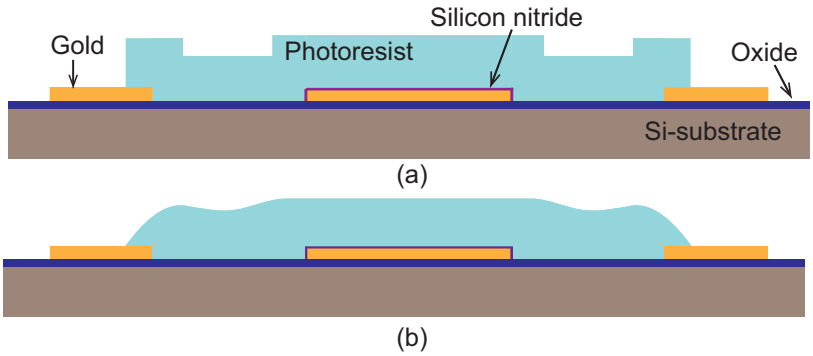

Fig. 2.9. (a) The ideal patterned photoresist layer, and (b) the actual photoresist layer.

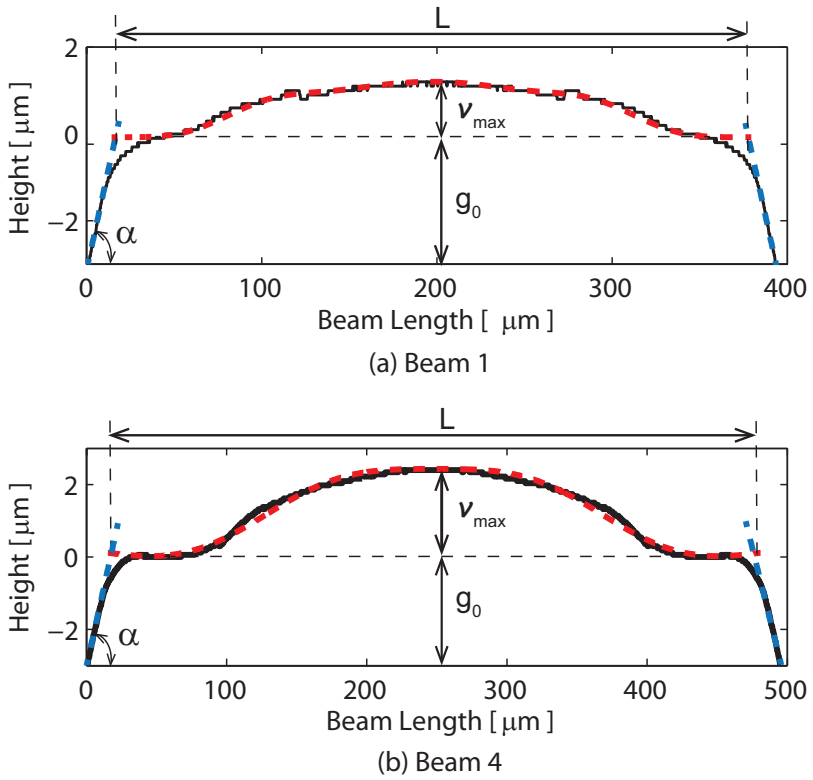

Fig. 2.10. Measured profiles of (a) a 400-μm-long beam and (b) a 500-μm-long beam (the red dashed lines are the approximated profiles using seven Fourier modes in (2.51)).

selected because of the working distance required for landing probes to apply voltages. The accuracy of the beam thickness and height is $\sqrt{2}\,(\pm\ 20\ nm) = \pm\ 28\ nm$ since a

subtraction for measuring the distance between two plane locations is needed. The gap between the beam and the actuation electrode cannot be shown explicitly in the 3-D image. Thus, in order to obtain the mid-point gap ($G_0 = g_0 + v_{max}$), we measured the height from the top of the beam to the actuation electrode at the mid-point of the beam, and subtracted the nickel thickness (h) from the measured height assuming that the electroplating is uniform. The indirect measurement leads to the accuracy of the gap to be $\sqrt{2}\,(\pm\ 28\ nm) = \pm\ 40\ nm$.

Table 2.3 summaries the measured geometric parameters for six beams studied in this chapter. The uncertainty indicates the systematic error due to the accuracy of the confocal microscope, without the random error included. The beam profiles are recorded along the beam as shown by the red dashed line in Fig. 2.8(b). Fig. 2.10 shows two examples of beam profiles. The approximated beam profiles are plotted in dashed lines, and the blue dashed lines are the tangent lines of the inclined supports at the points where the supports are fixed. The angle between the tangent line and the horizontal axis defines the inclination angle of the support. For the beams listed in Table 2.3, the uncertainty of the inclination angle (α) is $\pm\ 0.12^\circ$ depending on the lateral and vertical resolutions of the geometric measurements.

The displacement-voltage measurement is conducted by applying a DC voltage between the beam and the actuation electrode through two probes. The displacements are measured at the center of the beam for each voltage applied. The data collection for each beam is conducted automatically with the aid of a custom scripting software without moving the sample or changing any settings of the confocal microscope.

2.5.2 Displacement Curves and Effects of Support Compliance

The displacement-voltage curves are calculated by the beam model described in Section 2.3 using the measured geometric values listed in Table 2.3. The only unknown in the beam model is the initial stress σ_0 of the beam, and its value can be extracted by matching the predicted displacement from the beam model to the experimental

Table 2.3.
Measured geometrical data and material properties for fixed-fixed beams.

Parameter	Beam 1	Beam 2	Beam 3	Beam 4	Beam 5	Beam 6	Uncertainty
Designed Beam Length (L_0) [μm]	400	400	400	500	500	500	-
Designed Beam Width (b) [μm]	120	120	120	120	120	120	-
Beam Thickness (h) [μm]	1.78	1.74	1.99	2.03	1.73	1.83	$\pm$ 28 nm
Max. Initial Deflection (v_{max}) [μm]	1.55	1.32	1.28	2.04	1.87	1.22	$\pm$ 40 nm
Initial Flat Gap (g_0) [μm]	2.95	3.11	3.00	3.09	2.84	2.79	$\pm$ 40 nm
Inclination Angle of Supports (α)	10.1°	10.5°	9.9°	10.3°	10.2°	9.7°	$\pm$ 0.12°
Residual Stress (σ_0) [MPa]	-3.0	-2.9	-2.1	-3.5	-2.9	-2.0	-

result at a single voltage point. If all measured displacements are used instead of a single displacement measurement, taking Beam 1 for example, the extracted residual stress changes by -0.08 MPa, which leads to a variation of 0.1% in the predicted displacements. The displacement-voltage curve changes less than 0.2% corresponding to the measurement uncertainty of $\pm\ 0.12^{\circ}$ for the inclination angle. Fig. 2.11 shows the calculated and measured curves of displacement vs. actuation voltage, and they are in good agreement with an average error of 5.2%. All these beams have compressive initial stresses, which explains the upward deflected initial shapes of the beams. For beams with the same length and inclination angle of supports, higher compressive stress leads to higher initial deflection. Since the electrostatic force is proportional to the square of the gap, higher initial deflection leads to lower electrostatic force when the same voltage is applied, and consequently, smaller vertical displacement.

The effects of the inclined supports on beam deflections are illustrated in Fig. 2.12, in which three different types of boundary conditions are examined for Beam 3. The fixed boundary model implies that all degrees of freedom at the beam boundary are constraint to zero. The vertical support model in [45] used only a constant torsional stiffness at the boundary given by $k_T = 4EI/(g_0 + h)$. The resulting displacement-voltage curves are compared in Fig. 2.12(a). The fixed boundary model renders larger displacements compared with the inclined support model. It can be explained by examining the axial stress of the beam as plotted in Fig. 2.12(b). When the inclined support model is used, the axial force calculated by (2.47b) takes into account both the nonlinear stretching of the beam and the axial displacement δ_{aw} from the inclined support. However, the nonlinear stretching of the beam for the downward deflection shortens the arc-length of the beam compared with the initial position $v\,(x)$ and results in a compressive stress. The axial displacement δ_{aw} shown in Fig. 2.12(c) results in a relaxation of this compressive stress. The total axial stress is still compressive, but it is smaller than the fixed boundary case that ignores the δ_{aw} effect. In other words, in both the fixed boundary model and the vertical support model, it is assumed that there is no axial compliance ($\delta_{aw} = 0$), and the axial stress changes only

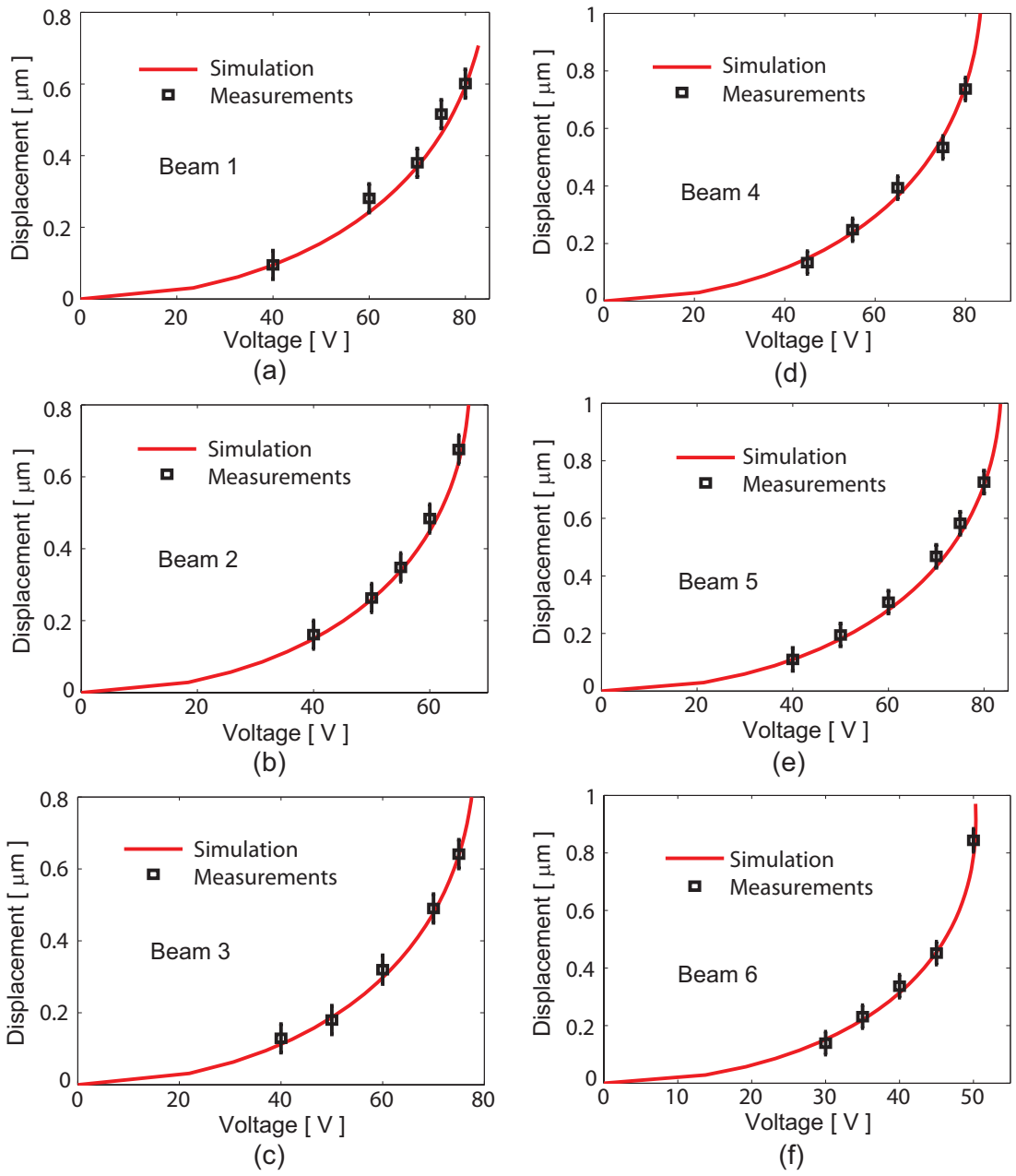

Fig. 2.11. Experimental and calculated displacement vs. voltage curves for (a) Beam 1, (b) Beam 2, (c) Beam 3, (d) Beam 4, (e) Beam 5, and (f) Beam 6. The error bars correspond to the measurement uncertainty of ± 40 nm.

by the nonlinear stretching of the beam. Therefore, the fixed boundary model and the vertical support model generate higher compressive stresses than the inclined support

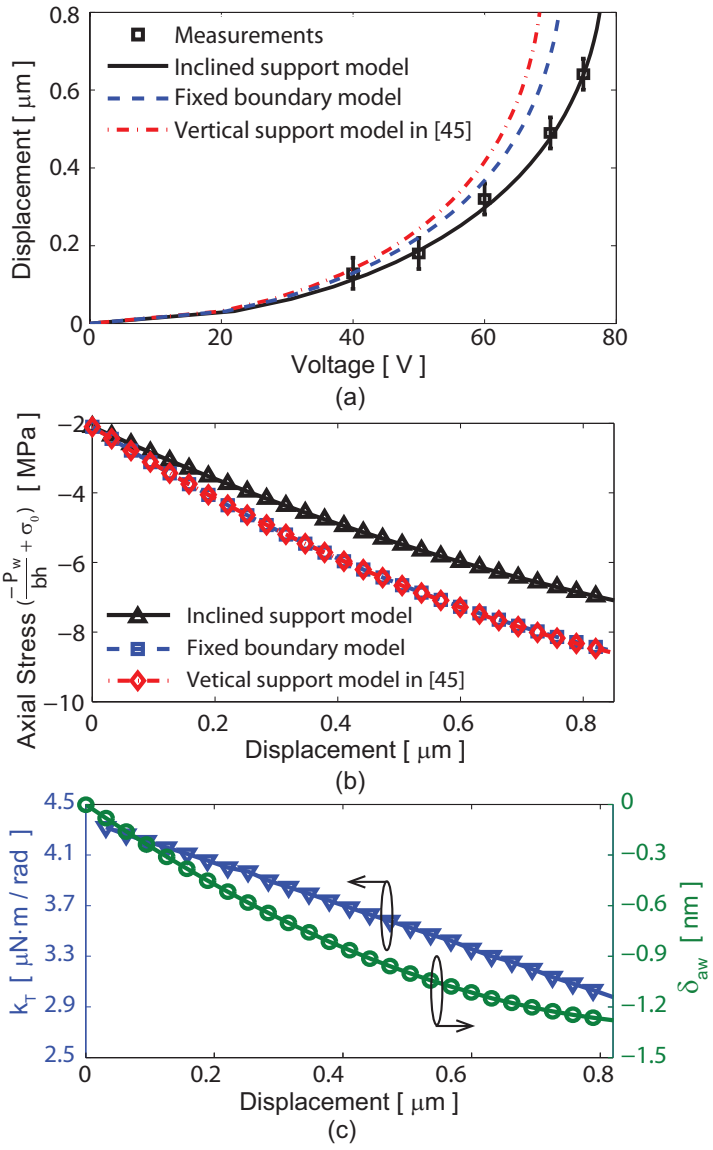

Fig. 2.12. Comparison for Beam 3 of (a) displacement curves, and (b) the axial stresses from different support models, and (c) the torsional boundary stiffness k_T and the axial displacement δ_{aw} of the inclined supports.

model as shown in Fig. 2.12(b), and consequently, larger displacements as shown in Fig. 2.12(a).

It is also worth noticing that the translation displacement at the beam boundary is linearly related to the axial displacement by $\delta_{tw} = \delta_{aw}/tan\,(\alpha)$, and therefore, δ_{tw} is

also in the nanometer scale. The torsional stiffness k_T at the beam boundary plotted in Fig. 2.12(c) is not constant. It is because the rotation angle at the beam boundary θ_{Bw} is caused by vertical load force, axial force, and moment as calculated in (2.58). With the increased actuation voltage, the rotation angle due to the electrostatic force increases and dominates, and therefore, by the definition of k_T in (2.61), k_T decreases.

2.6 Conclusion

This chapter presents an equation-based nonlinear model for inclined supports in MEMS fixed-fixed beams. The effects of the inclined-support compliance on the post-release stress relaxation and on the beam deflections are discussed. This model accounts for non-flat beam profiles caused by residual stress and/or an uneven sacrificial layer topology. The nonlinear effects due to stretching and residual stress are included. In the mechanical beam model, the inclined-support compliance can be represented by a constant coupling matrix whose value is independent of external loads. The support compliance causes stress-induced deflections which leads to stress relaxation. For the electromechanical beam model, the rotational support compliance is represented by a torsional stiffness which is employed by the Galerkin method for solving the model. We find that the torsional stiffness varies with the electrostatic loading, the stress state, and the initial beam profiles. We also show that the inclination angles of the supports have great effect on beam deflections, especially for shallow angles less than 45°. The calculated beam displacements agree with FEM simulations to within 1.1% in both the linear and nonlinear regimes. Furthermore, the displacement-voltage curves from the electro-mechanical beam model are experimentally validated with an average error of 5.2%.

3. RESIDUAL STRESS EXTRACTION OF MEMS BEAMS USING A WAFER-SCALE TECHNIQUE

3.1 Introduction

Thin films in MEMS devices tend to exhibit length-scale-dependent and process-dependent mechanical properties which are often quite different than bulk properties [59]. The performance of typical MEMS devices highly depends on the properties of their structural materials. For example, the residual stress in electrostatically actuated RF MEMS switches is a key parameter in determining the pull-in voltages and switching time [60]. Therefore, it is imperative to monitor the residual stress at wafer-scale level for predicting the performance and reliability of devices. This chapter reports on the extraction of residual stress in fixed-fixed beams using a wafer-scale technique.

A wafer-scale extraction technique requires automated testing, fast data acquisition and cost-effective implementation. Table 3.1 summarizes the limitations of the existing techniques for residual stress extraction. In general, these techniques were all nondestructive, since destructive tests cannot be repeated for verification and the debris could lead to potential failure of other active devices on the wafer. There are three main categories of residual stress extraction methods for free-standing thin-films: static mechanical, electrostatical/pull-in, and dynamic resonant. The first category using mechanical loads included bulge test [61–64], nanoindentation test [65, 66],and microtensile/microbending test [67–70]. The challenge of applying small mechanical loads with high resolution in microscale testing demanded for special sample preparations or special test fixtures, which increased the design complexity and characterization cost. Chen [71] reported an extraction method by measuring thermal deflections at different temperatures up to 103°C. However, this method was not

Table 3.1.
Comparison of methods for residual stress extraction.

References	Requires Special Sample Preparation and/or Test Fixtures	Requires Iterative FEM Simulations	Requires Multiple Testing Beams	Assumes a Flat Initial Profile	Presumes Profile Shapes	Requires High Temperature Measurements	Only Applicable to Compressive Stress	Assumes Ideally Fixed Anchors
[61–69]	✓	✗	✗	✓	✗	✗	✗	✓
[70]	✓	✓	✗	✗	✓	✗	✗	✓
[71]	✗	✓	✗	✗	✗	✓	✗	✓
[33]	✗	✗	✗	✗	✓	✗	✓	✗
[72]	✗	✗	✓	✓	✗	✗	✗	✓
[73, 74]	✗	✗	✗	✓	✗	✗	✗	✓
[34]	✗	✗	✓	✗	✓	✗	✗	✗
[75]	✗	✓	✗	✓	✗	✗	✗	✗
[76]	✗	✓	✗	✓	✗	✗	✗	✓
[77, 78]	✗	✗	✗	✓	✗	✗	✗	✓
[48]	✗	✗	✗	✗	✓	✗	✗	✗
This Work	✗	✗	✗	✗	✗	✗	✗	✗

applicable to devices which cannot sustain high temperatures, and the required iterative simulations of computationally expensive finite-element-model (FEM) made it impractical for wafer-scale measurements. In [33], Fachin presented an approach without any external loads required, and only the post-release beam deformations due to compressive stresses were measured, which precluded itself from extracting tensile stresses.

Electrical input signals utilized in the second category can be applied easily, and therefore are preferred in large-scale tests. The M-test proposed by Osterberg [72], which measured pull-in voltages of electrostatically actuated beams, achieved fast data acquisition by only using standard electrical test equipment and a microscope. However, the pull-in behavior led to contact wear and dielectric charging issues, and the test structures containing a group of beams occupied a large area on the wafer. To improve the verifiability of the test, the beam deformations below the pull-in limit were recorded for extracting the residual stress [34, 73, 74], but multiple beams were still required for these techniques. In [75], a method using a single beam was presented, but it relied on iterative FEM simulations. In addition, the initial beam curvature was not included in the beam model which degenerated the accuracy of the results. The last category involves dynamic tests, in which the test structures were powered into vibration, and the fundamental resonant frequency [76, 77] or multiple eigenmodes [48, 78] were measured to determine the residual stress. However, in [76–78], the effects of anchor compliance and non-flat initial profiles of test structures were neglected. The initial profile of the testing beam was taken into account in [48] by a presumed arc shape, which might not follow the actual irregular beam profiles and result in non-negligible errors of the extracted residual stress. In addition, the eigenmodes of the beam becomes less sensitive when boundary spring stiffness is small, and therefore, leading to larger errors of the predicted residual stress by the method in [48] for beams with small boundary stiffness.

In order to accurately quantify the residual stress at wafer-scale, an efficient extraction technique is developed in this chapter. It employs a comprehensive reduced-order

beam model and electrostatic measurements taken at room temperature with only one beam required. Neither modification to the regular fabrication processes nor special specimen preparation is required. The key to this technique lies in the recognition that for an electrostatically actuated fixed-fixed beam with a given value of residual stress, there exists a unique displacement-voltage curve. The residual stress is determined by iterating its value to match the simulated displacement-voltage curve to measurements. Non-ideal effects of beams, such as non-ideal anchor supports, initially curved beam profiles and electrostatic fringing fields, are characterized for accurate residual stress extraction. With the aid of a custom scripting software program collecting experimental data automatically, and an efficient optimization algorithm for automatic extraction, the wafer-scale characterization of residual stress can be achieved.

3.2 Extraction Methodology

3.2.1 Comprehensive Reduced-order Models and Characterization of Non-ideal Effects of Fixed-Fixed Beams

The extraction of the residual stress requires a large number of iterative simulations and thus an efficient simulation package is desirable for wafer-scale extraction implementation. A reduced-order numerical model as described in [50, 52] is used here. Compared to computationally expensive FEM codes, this model effectively predicts beam behaviors while being comprehensive enough to incorporate the multi-physics phenomena and non-ideal conditions including non-vertical supports, initially non-flat beam profiles, and electrostatic fringing fields.

The anchor supports in MEMS beams cannot be assumed ideally rigid, and additionally, these supports are not always vertical as assumed in most beam models [34, 45, 79, 80]. Instead, they can be inclined as illustrated in Fig. 3.1(a). This is often due to the shape of the sacrificial layer during fabrication. The topologies of the spin-on layers (e.g., photoresist) strongly depend on the process conditions. The compliance of these supports has nontrivial implications on beam performance, and

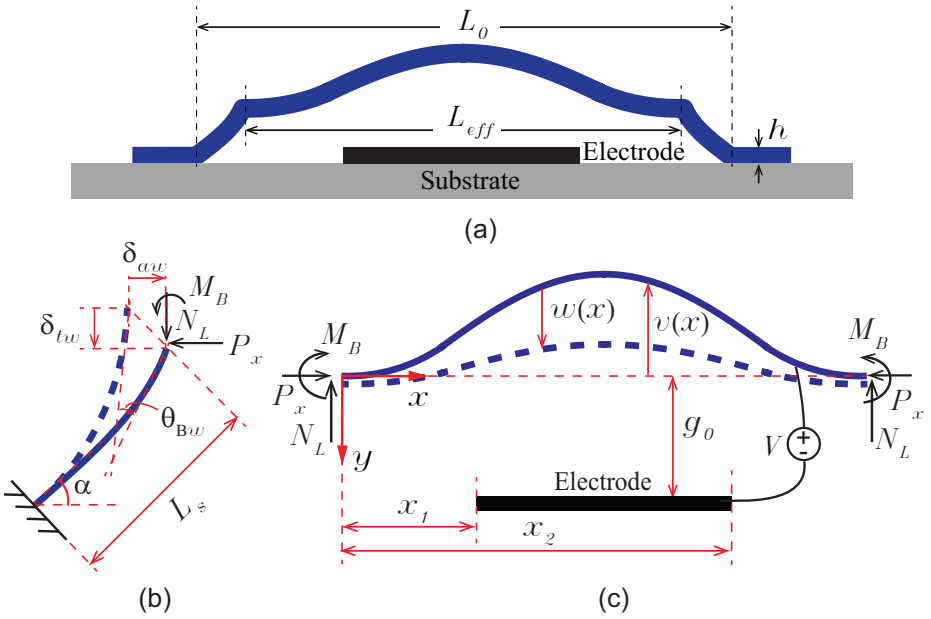

Fig. 3.1. (a) Schematic for a fixed-fixed beam with inclined supports and a non-flat profile, (b) model for the inclined support, and (c) model for the horizontal beam with a non-flat profile.

therefore, significant errors in extracting residual stress may occur if the supports are not properly modeled. Therefore, a model for inclined supports developed in [52] is used. The inclined supports are modeled as cantilever beams (Fig. 3.1(b)) connected to a horizontal beam with non-flat profiles (Fig. 3.1(c)). When the beam is actuated by an electrostatic force F_e, the beam deflects away from its initial post-release position $v\,(x)$. For a beam deflection $w\,(x)$, the support has relative axial displacement δ_{aw}, translational displacement δ_{tw} and angle rotation θ_{Bw} caused by the moment M_w, axial force P_w and reaction force $N_L = F_e/2$ at the joint node where the support connects to the horizontal beam. The Euler-Bernoulli equations for all beams are simultaneously solved to calculate the compliance of the supports as:

$$\begin{bmatrix} \delta_{aw} \\ \delta_{tw} \\ \theta_{Bw} \end{bmatrix} = \begin{bmatrix} K_{ij} \end{bmatrix} \begin{bmatrix} N_L \\ P_w \\ M_w \end{bmatrix} \tag{3.1}$$

where $[K_{ij}]$ is the coupling matrix as defined in [52], and $M_w = -EIw''(0)$. For a beam with thickness h and width b, $I = bh^3/12$ is the moment of inertia, and E is the effective Young's modulus. A beam is considered wide when the width is much larger than its thickness ($b \geq 5h$) and a plane strain condition is assumed with $E = E_0/(1-\nu^2)$, where E_0 is the Young's modulus and ν is the Poisson's ratio. For a narrow beam ($b < 5h$), $E = E_0$ [72]. It is worth to notice that M_w and P_w are the moments and axial force only due to the vertical beam displacement $w(x)$, respectively. With a residual stress σ_0, the total axial force is $P_x = P_w + \sigma_0 bh$.

To adapt to the Galerkin method for solving the beam model [49,50], a boundary torsional stiffness k_T is defined to present the rotational compliance of the supports which may vary with the beam displacement and residual stress:

$$k_T = -\frac{M_w}{\theta_{Bw}} \tag{3.2}$$

The inclination of supports not only changes the boundary compliance of the horizontal beam, but also shortens the effective length (L_{eff}) of the beam to:

$$L_{eff} = L_0 - 2\frac{g_c}{\tan\alpha} \tag{3.3}$$

where $g_c = g_0 + h/2$, and g_0 is the flat initial gap.

Another non-ideality is the non-flat initial profile of the beam, which can significantly affect the displacement-voltage relationship since the electrostatic force is a quadratic function of the gap between the beam and the actuation electrode. When considering an initially curved beam, most of the works assumed the shape of the beam [33, 81], but in this paper, we use a Fourier sine series which can approach any symmetric shape of beam profiles. When the initial beam profile is recorded as a function of position *v(x)*, where x is the axis along the beam, the Fourier series coefficients can be calculated by:

$$p_i = 2\int_0^1 v(x)\sin(i\pi x)\,dx \tag{3.4}$$

To accurately model the electrostatic force exerted on the beam, a modified electrode width, instead of its physical size ($W_0 = x_2 - x_1$) as shown in Fig. 3.1(c), is

used in the reduced-order model. Although the fringing fields in-plane with the beam cross sections has been included in the reduced-order model, the complex fringing effects arising from the finite width of the actuation electrode is neglected. In addition, the presence of the high dielectric-constant substrate distorts the electric fields compared to the case with dielectrics made of air or vacuum, and thus changes the electrostatic force. To compensate for these effects, an equivalent electrode width W is introduced, which is determined by matching the simulated capacitance and electrostatic force from the reduced-order model to the results of FEM simulations for the device structure.

3.2.2 Extraction of Residual Stress

The procedure of residual stress extraction starts with optical measurements of the geometric parameters of a beam. Then the gap at the center of the beam is measured when a DC actuation voltage is applied between the beam and the electrode. By changing the actuation voltage incrementally and recording the corresponding gap, a gap versus voltage curve is obtained.

The extraction technique for residual stress is illustrated by the flowchart in Fig. 3.2 [82]. Assuming all material properties expect the residual stress are known, with the experimental geometric data, the parameters modeling the non-ideal effects, namely, Fourier coefficients p_i, effective length L_{eff} and equivalent electrode width W, can be calculated accordingly. Then, starting from an initial guess for residual stress, the displacement-voltage curve is simulated by the reduced-order model, and the value of the residual stress (σ_0) is iterated using an optimization function implemented in MATLAB [83] until the best fit between the simulated and measured displacement-voltage curves with the smallest root-mean-square (RMS) fitting error is found, and this value is taken to be the best estimate of the residual stress. When a large number of beams are measured for wafer-scale extraction, the beams are numbered and the experimental data is tabulated in a spreadsheet. Simulation scripts

are developed which can read the input data and searching for the optimal value of residual stress automatically by specifying the beam numbers.

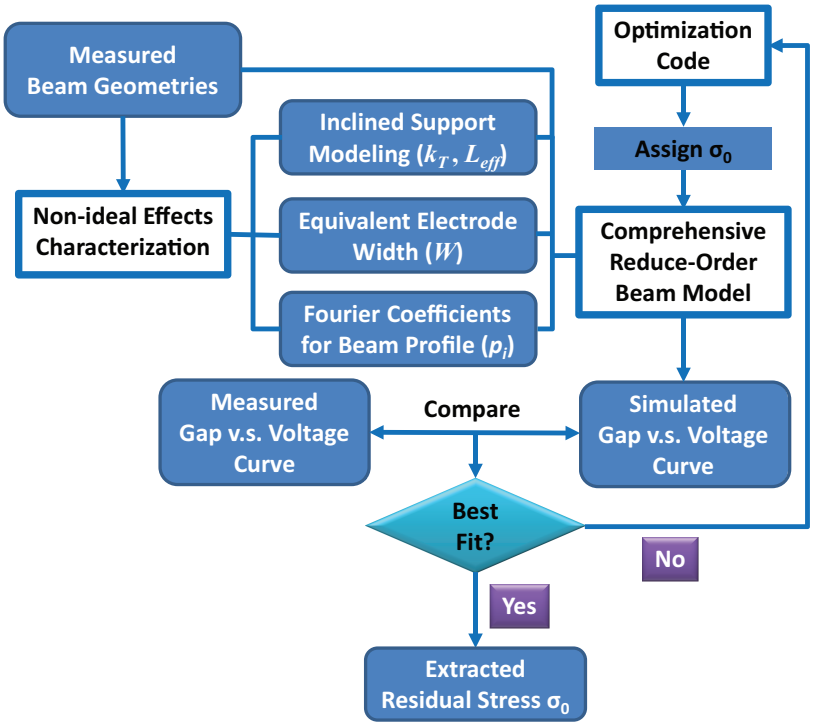

Fig. 3.2. Flow chart of the residual stress extraction technique.

3.3 Fabrication and Measurement

Typical RF MEMS capacitive beam switches as shown in Fig. 3.3(c) are fabricated using the same process described in Chapter 2. Beams with two different lengths (400 μm and 500 μm) are fabricated with the same width of 120 μm. The geometric parameters of the devices are measured optically using the confocal laser scanning microscope LEXT OLS3100 from Olympus. The geometric measurement methods and accuracy are the same as discussed in Chapter 2.

A measurement setup shown in Fig. 3.3 is used to collect the displacement-voltage curves. A Keithley 2410-C DC power supply is used to provide the actuation voltage between the beam and the actuation electrode through two probes. A custom

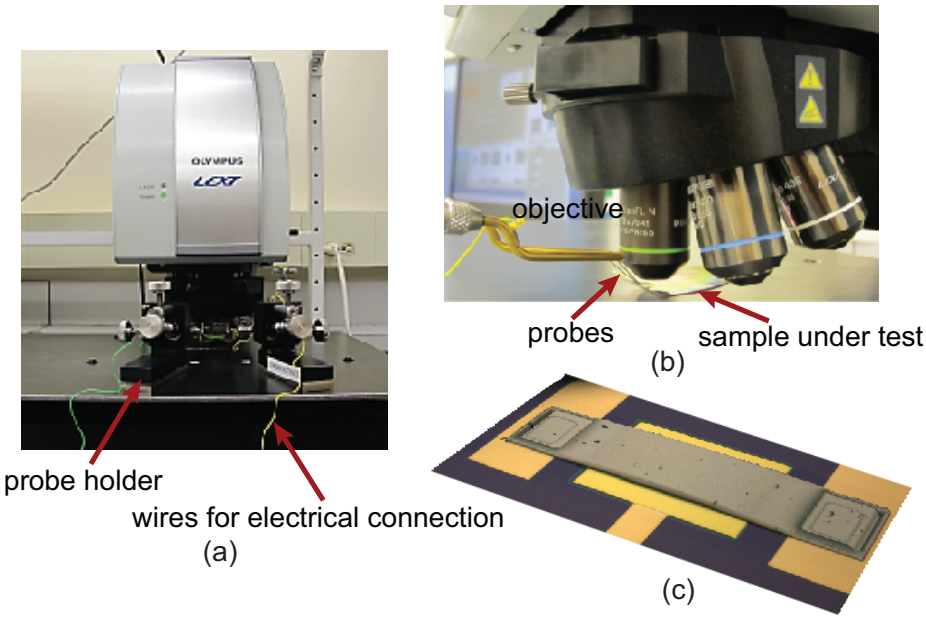

Fig. 3.3. (a) Measurement setup, (b) closeup of the objective and wafer, and (c) a 3-D image of the MEMS fixed-fixed beam.

scripting software program is developed to automate the data collection in the measurements. The power supply is controlled to change the DC voltage incrementally, and the confocal microscope is programmed to take a new scan once the voltage is increased.

3.4 Results and Discussion

3.4.1 Geometric Measurement Data

The geometric data of 87 beams on a quarter-wafer are measured using the LEXT confocal microscope and their mean values and standard deviations are summarized in Table 3.2, assuming that each parameter follows a normal distribution. L_0 is the physical beam length (Fig. 3.1(a)). As shown later in Section 3.4.2, the beam profile is symmetric but not initially flat across the length. Therefore, the initial mid-beam gap ($G_0 = g_0 + v_{max}$) is determined by both the initial flat gap (g_0) and the additional

gap (v_{max}) due to the non-flat profile. Among all geometric parameters, the beam thickness (h) and the initial mid-beam gap are the most important in determining the beam deflection. Their histograms for all measured beams are shown in Fig. 3.4. The nearly normal distribution of the measured beam geometries indicate the uncertainties due to the non-ideal fabrication process.

Table 3.2.
Geometric measurement data (± indicates one standard deviation level).

Geometric Parameter	Measurement Value
Beam Length (L_0)	495.10 ± 0.67 μm
	395.59 ± 0.79 μm
Beam Width (b)	122.79 ± 0.40 μm
Beam Thickness (h)	1.83 ± 0.28 μm
Initial Gap ($G_0 = g_0 + v_{max}$)	4.62 ± 0.57 μm
Initial Flat Gap (g_0)	2.84 ± 0.26 μm

3.4.2 Characterization of Non-ideal Effects

The non-ideal effects of the beams can be characterized with the measured geometric data as discussed in Section 3.2. Fig. 3.5 shows examples of measured beam profiles and the beam model used in the reduced-order numerical simulation for both 400 μm and 500 μm beams. The middle section of each beam profile curves up where there is an actuation electrode beneath it. The anchor supports are not ideally vertical, but are inclined towards the center of the beam. The blue dashed line in Fig. 3.5 is the tangent line of the inclined support at the point where the anchor is fixed, and the angle between the tangent line and the horizontal axis defines the inclined angle of the support α which is about 10°. The beam is assumed being anchored at the points where the horizontal level (the red dashed line) which indicates the initial flat

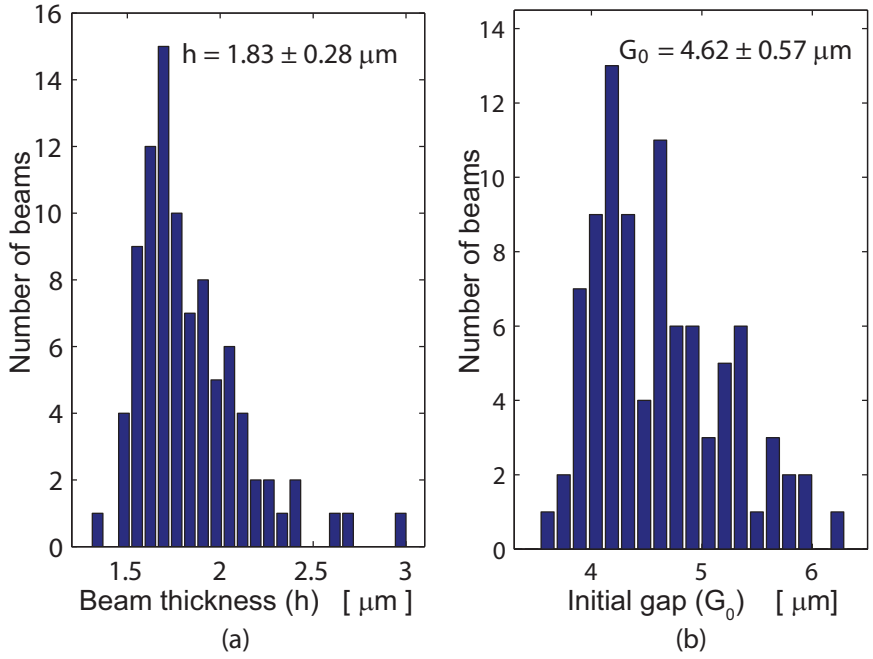

Fig. 3.4. Histogram of measured (a) beam thickness and (b) initial gap at the center of the beam.

gap (g_0) meets the two tangent lines of the supports at both sides of the beam. In the beam model, the effective beam length L_{eff} is calculated by (3.3).

The non-flat profile of the beam is approximated by a finite Fourier sinusoid series calculated from (3.4). A Fourier series with more modes describes the beam profile more accurately, and thus yields more accurate result of extracted residual stress. However, the computation time for the beam model increases with the increase of the Fourier modes used. Therefore, a Fourier series with 7 modes is used in simulations as a tradeoff between accuracy and computation efficiency (see Section 3.5.3). The profile for each beam model in Fig. 3.5 is constructed by these Fourier coefficients, which closely resembles the measured profiles.

The equivalent electrode width for accurate modeling of the electrostatic force is studied. The physical width of the electrode is designed to be $W_0 = 270$ μm. As shown in Fig. 3.6, the capacitance and electrostatic force from the reduced-order model are compared to the results of 3-D FEM simulations by CoventorWare [55].

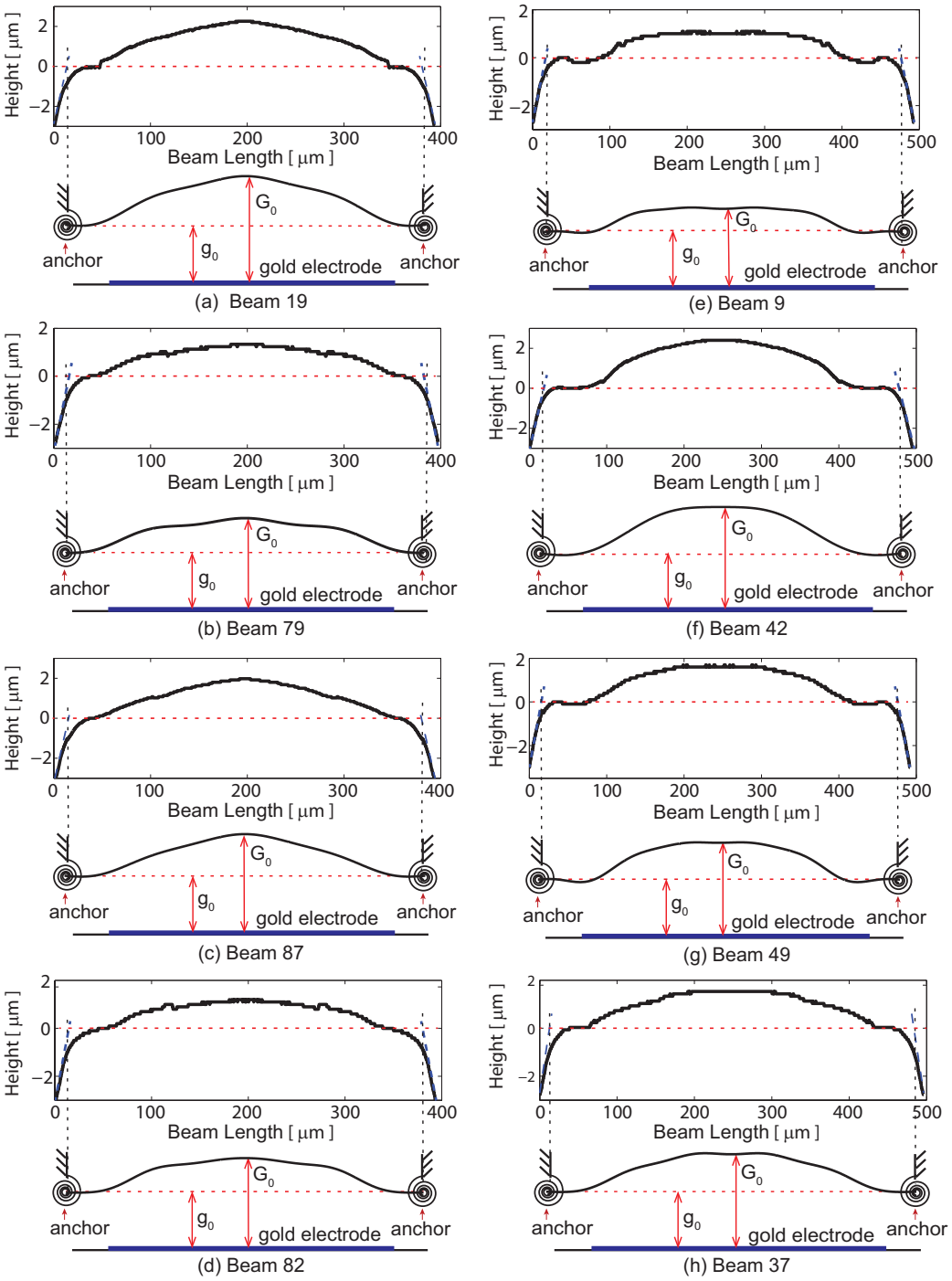

Fig. 3.5. Measured profiles and beam model with non-flat profiles and inclined supports.

The capacitance and the electrostatic force are best matched when the electrode width in the reduced-order model is increased by 6.36% and 4.19%, respectively. $W = 287.16$ μm (for electrostatic force matching) provides closer match of the gap versus voltage relationship between the reduced-order and 3-D models. Therefore, an equivalent electrode width of $W = 287.16$ μm is used in the reduced-order numerical model for the extraction of residual stress.

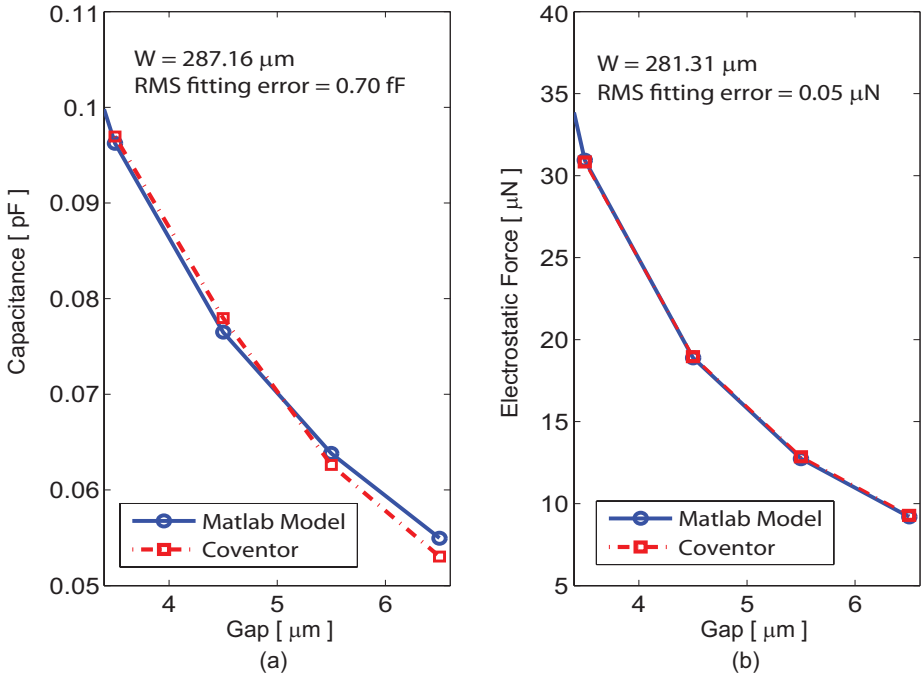

Fig. 3.6. Curve fitting for equivalent electrode width by matching (a) capacitance and (b) electrostatic force from reduced-order model to FEM simulations.

3.4.3 Results of Extracted Residual Stresses

The extraction of residual stress is performed for all 87 beams measured. The nickel beams have density of 8913 kg/m^3 and Poisson's ratio of $\nu = 0.3$. For any value of a fixed Young's modulus E_0, there must be a value of the residual stress (σ_0) that provides the best fit to the measured gap versus actuation voltage curve with the

smallest RMS fitting error as shown in Fig. 3.7(b). Therefore, the E_0 and σ_0 cannot be decoupled and extracted simultaneously by this method. For a electroplated nickel thin film, the value of E_0 differs from the bulk material value and is related to plating conditions [84]. For the nickel beams in our study, $E_0 = 199.9$ GPa is used which is determined in [54]. The searching for the optimal value of residual stress is illustrated by an example shown in Fig. 3.7(a). With the geometric data and other material properties determined, the reduced-order numerical model predicts a corresponding displacement-voltage curve for each value of residual stress. The best fit between the simulated and measured displacement-voltage curves gives the result of the extracted residual stress.

For all the 87 beams measured, the color-scaled results of the extracted residual stress (σ_0) ranging from -12.8 MPa to 13.6 MPa are shown with respect to the location of beams on the wafer in Fig. 3.8. A histogram of the extracted residual stress are plotted in Fig. 3.9. The positive values represent tensile stresses while negative ones are compressive stresses. The values of residual stress exhibit a nearly normal distribution with a mean value of -1.7 MPa and a standard deviation of 5.9 MPa which indicates the variability of the residual stresses on the wafer.

The stress level of the electroplated film depends practically on process conditions, such as bath composition, current density, and temperature [84]. Using a nickel sulfamate solution, the stress level of the nickel layer may be tuned from tensile to compressive stress by process parameters. The electroplating process described in Section 3.3 is developed for a low-stress nickel layer. The extracted values of residual stress (σ_0) fall in the expected range. As shown in Fig. 3.8, in the electroplating process, the cathode is clamped at the edge of the wafer for the electrical connection to a thin seed layer of 50-nm sputtered Ti and 30-nm evaporated Ni. The high resistance of the thin seed layer leads to larger current densities, thus higher residual stresses [84–86], near the cathode electrical contact.

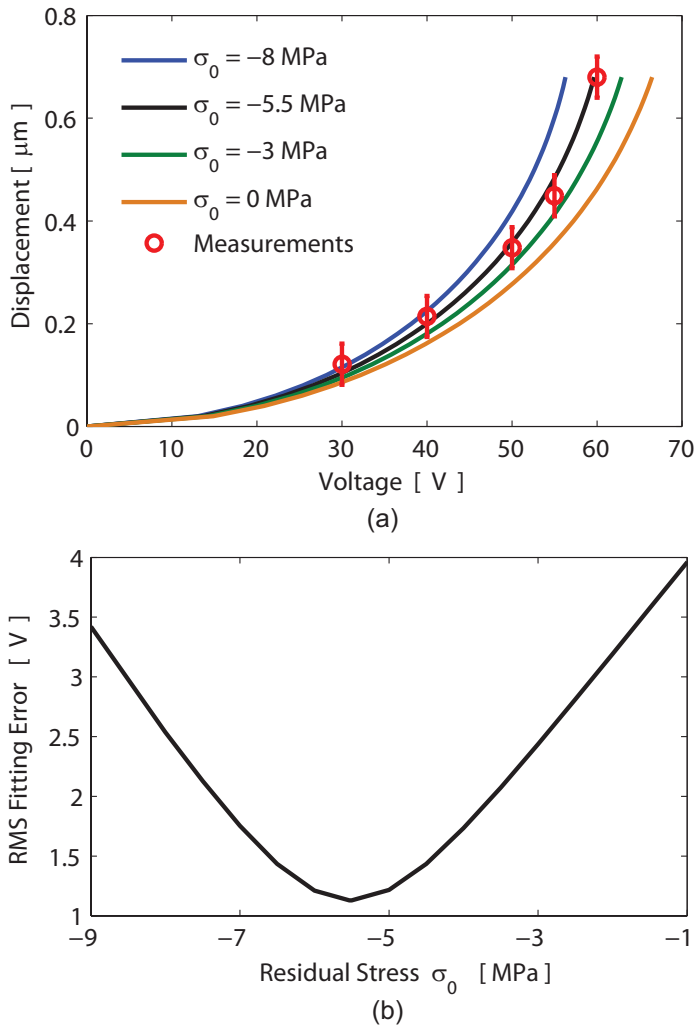

Fig. 3.7. An example of (a) the best fit of the simulated and measured displacement versus voltage curves with the optimal value of residual stress σ_0, and (b) the curve fitting error versus residual stress σ_0.

3.5 Uncertainty Analysis

The uncertainties of the extracted residual stress are analyzed by calculating the sensitivity of the results to the variations of input parameters. There are three main categories of uncertainties: the measurement uncertainty of the geometric parameters, the uncertainty of the material properties used, and the uncertainty in modeling the non-ideal effects. A 500 μm sample beam, with geometric data around the mean val-

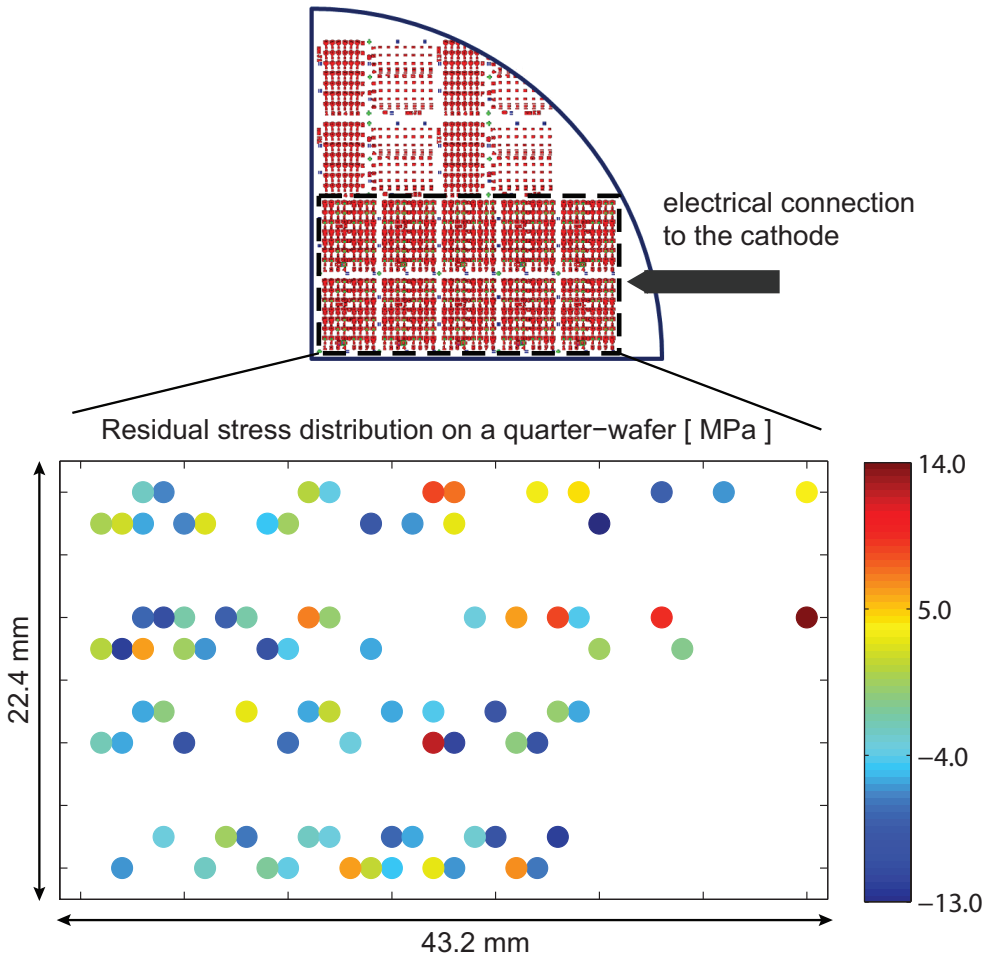

Fig. 3.8. Beam locations on the wafer and color-scaled results of the extracted residual stress σ_0.

ues listed in Table 3.2 and residual stress of −5.5 MPa, is selected for the uncertainty analysis of the stress extraction technique. The measured displacement-voltage curve is shown in Fig. 3.7(a). By varying each input parameter individually, the sensitivity of the extracted residual stress to each input parameter can be estimated.

3.5.1 Uncertainties Due to Geometric Measurements

The sensitivities of the extracted residual stress to the beam thickness (h) and the initial gap (g_0) are plotted in Fig. 3.10. The total initial gap (G_0) includes both

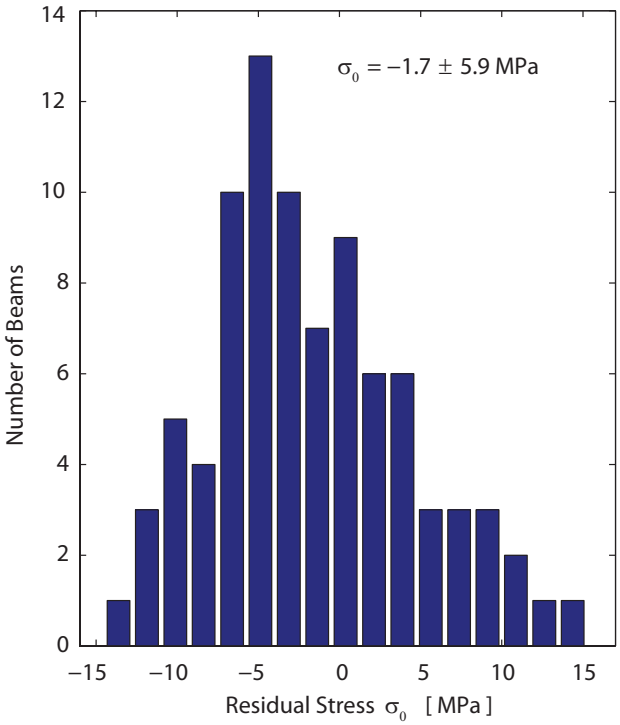

Fig. 3.9. Histogram of extracted residual stress σ_0 using the beam model in Fig. 3.5.

the initial flat gap (g_0) and the additional gap (v_{max}) due to the non-flat profile. The effects of the non-flat profile will be analyzed later in Section 3.5.3. The variations of the extracted residual stress due to the measurement uncertainties of the beam length and width are neglected, since the lateral measurement accuracy of $\pm$ 0.6 μm is small enough compared to the lateral beam geometries, which are 120 μm wide and 400/500 μm long.

By referring to the Euler-Bernoulli beam equation, we know that for an electrostatically actuated beam, its displacement is proportional to the 3rd order of the beam thickness h and is inversely proportional to the square of the gap between the beam and the actuation electrode. With the increase of thickness h, the beam becomes harder to bend, and therefore the extracted result of σ_0 decreases (a larger compressive stress) to match the measured displacement-voltage curve. According to

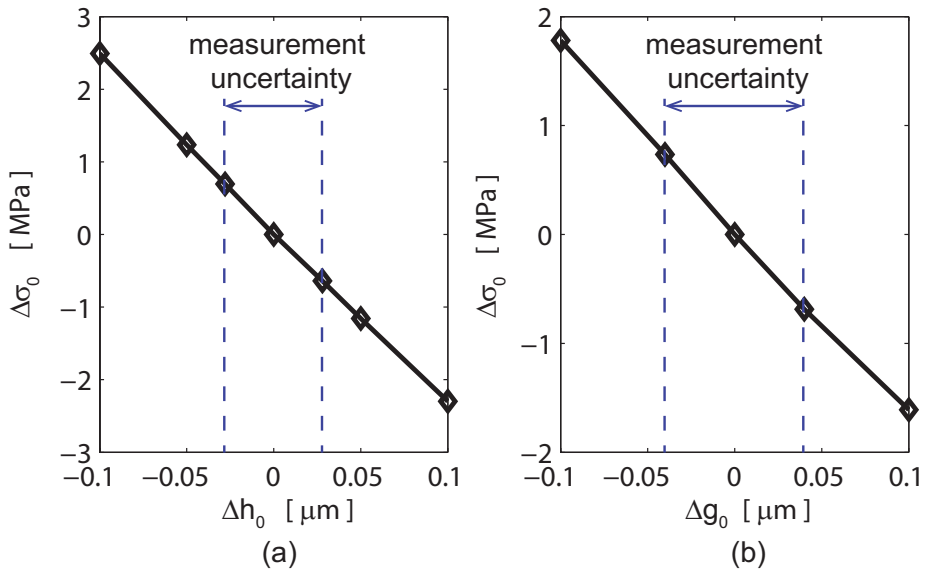

Fig. 3.10. Extracted residual stress versus the variation of (a) the beam thickness h and (b) the initial beam flat gap g_0.

Fig. 3.10(a), a measurement uncertainty of ± 28 nm for the beam thickness corresponds to ± 0.6 MPa variation of the extracted residual stress. Since the electrostatic force exerted on the beam is inversely proportional to the square of the gap, the beam defects less if the initial gap g_0 increases. As a results, a smaller residual stress is required to compensate for the decrease of the beam displacement. Fig. 3.10(b) indicates the uncertainty of the residual stress is ± 0.7 MPa due to the ± 40 nm measurement accuracy of the initial gap.

The residual stress is extracted by matching the simulated and measured displacement-voltage curves, and therefore, the variation of the measured displacements directly affect the results of the residual stress. Theoretically, only one measurement of the displacement at a certain voltage is necessary to determine the residual stress since it is the only unknown in the inputs to simulation the displace-voltage relationship. However, we measured beam displacements at multiple voltages and extracted residual stress by matching the simulations to the measured displacement-voltage curve (Fig. 3.7) to minimize the uncertainty of extracted stress due to the error of the dis-

placement measurements. In Fig. 3.11, the black curve shows that if only the last displacement is used for stress extraction, the variation of the displacement measurement ± 40 nm results in an uncertainty of ± 0.5 MPa for the extracted stress. This uncertainty reduces to ± 0.2 MPa when five measurements are used as indicated by the red curve in Fig. 3.11.

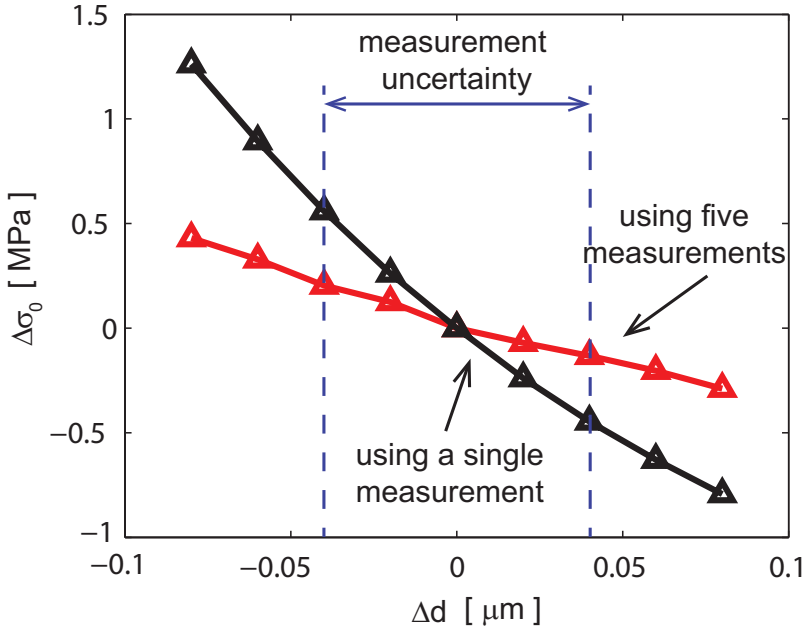

Fig. 3.11. Extracted residual stress versus the variation of measured beam displacements (the black curve presents the case when only the last displacement measurement in Fig. 3.7(a) is used for stress extraction, and the red curve presents the case when all five measurements are used).

3.5.2 Uncertainty Due to Material Properties

The residual stress extraction requires predetermined Young's modulus E_0 for the thin-film nickel, and therefore the uncertainty due to the accuracy of the experimental results of Young's modulus needs to be analyzed. Fig. 3.12 shows that, for E_0 = 199.9 GPa and with a variation of ± 10%, the extracted residual stress decreases linearly with the increase of E_0. If the variation of E_0 is kept within ± 1.1 GPa

(±0.55%) [54], the uncertainty of the residual stress due to E_0 is ± 0.1 MPa. The beams in this study is considered as wide beams ($b \geq 5h$) and a plane modulus $E = E_0/(1-\nu^2)$ is used in the simulation. If the plane strain condition is neglected, with $\nu = 0.3$, the extracted residual stress will have an error of 3.0 MPa.

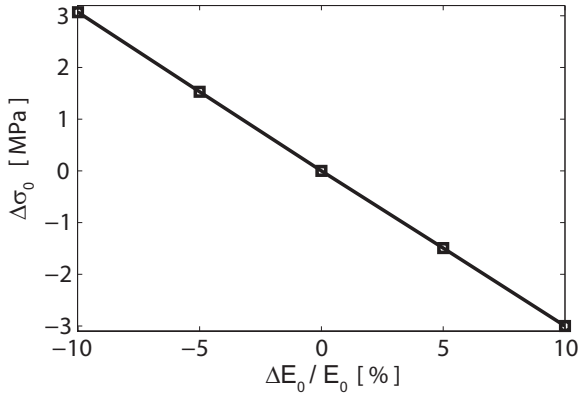

Fig. 3.12. Extracted residual stress versus the variation of Young's modulus E_0.

3.5.3 Uncertainties Due to Non-ideal Effects Modeling

The non-ideal effects are discussed in Section 3.4.2 and the uncertainties due to the non-ideal effects modeling are analyzed below. Fig. 3.13(a) indicates how the results of residual stress vary with the number of Fourier modes used to represent the beam profiles. According to (3.4), when i is even (i = 2, 4, 6, ...), the corresponding Fourier coefficient p_i is 0 for symmetric beam profiles, and therefore it has no impact on the shape of the profiles. Consequently, the results of residual stress are the same when the number of Fourier modes used in the simulation are n and *(n+1)* (n is an odd integer). The computation time for stress extraction increases exponentially with the number of Fourier modes used, therefore, there is a tradeoff between the accuracy and the computation efficiency. For small numbers of Fourier modes (<7), the extracted residual stress varies dramatically with the number of Fourier modes, which indicates the results are not convergent. The variation of the residual stress is

0.2 MPa when the number of Fourier modes increases to 9 from 7, and it is 0.1 MPa when the number of Fourier modes increases to 11 from 9. Therefore, we choose to use 7 Fourier modes. Most of the publications made assumptions about the shapes of the beams, such as a circular arch [81] or a sinusoidal shape [33], which were close to the case when only one Fourier mode is used to describe the beam profile in the reduced-order numerical model. The corresponding error of the residual stress is about 10.6 MPa due to the inaccurate modeling of the beam profile.

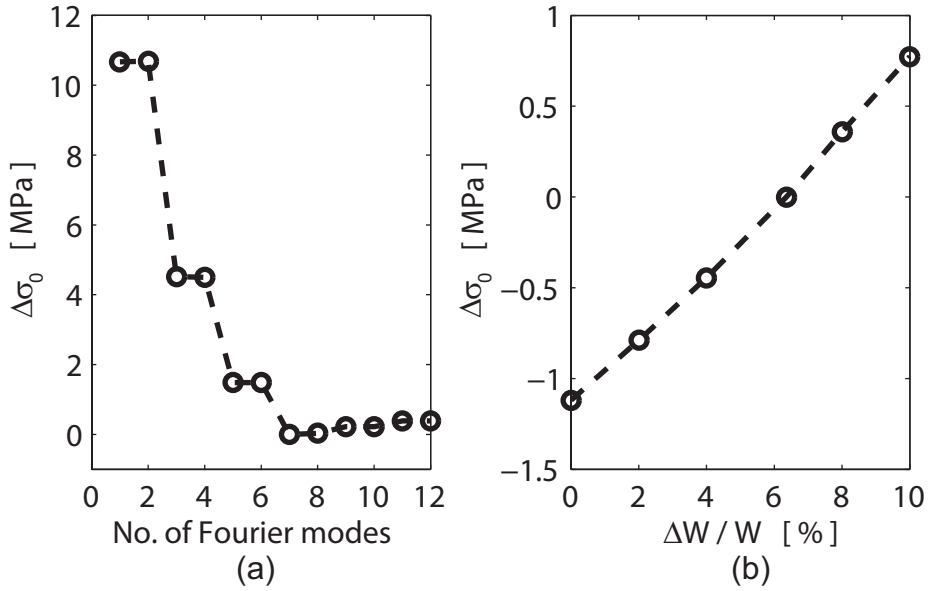

Fig. 3.13. Extracted residual stress versus the variation of (a) the number of Fourier modes describing the beam profile and (b) the equivalent electrode width.

In Section 3.4, it is shown that an equivalent electrode width which is 6.36% wider than its physical size is used in the simulation in order to account for the additional fringing field effect not included in the reduced-order model. Fig. 3.13(b) presents how the extracted residual stress changes with the value used for the electrode width. If the additional fringing field effect is neglected and the physical size of the electrode width is used ($\Delta W = 0$), the extracted residual stress will decrease by 1.1 MPa comparing to the case when the equivalent electrode width ($\Delta W = 6.36\%$) is used.

The modeling of the inclined supports provides the boundary conditions for solving the displacement-voltage curves of the horizontal beam, and therefore, directly affects the results of the extracted residual stress. The variation of σ_0 due to the inclination angle of the supports α is plotted in Fig. 3.14(a). It should be noticed that the variation of α not only changes L_{eff} but also affects the compliance of the supports [52]. If α varies by $\pm$ 1°, σ_0 will change by $\pm$ 0.4 MPa.

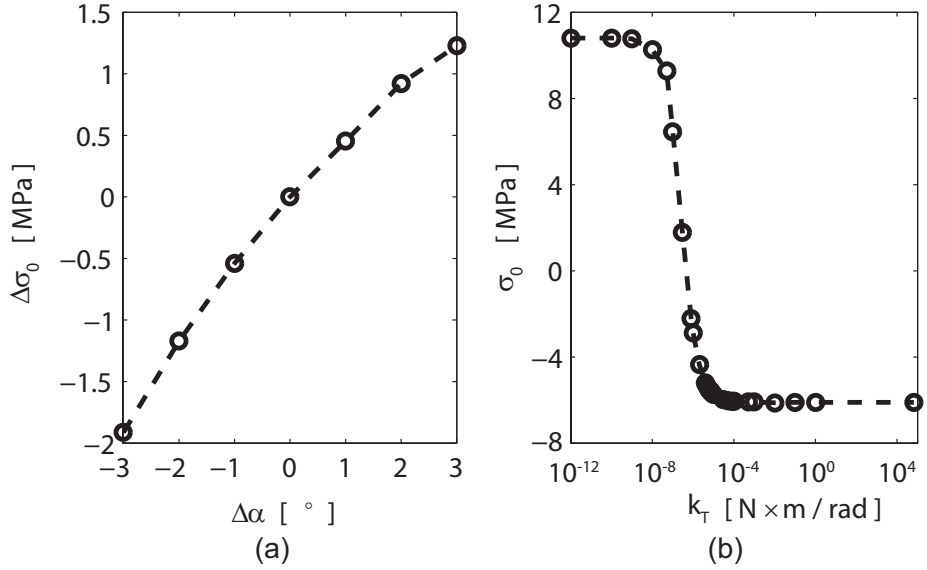

Fig. 3.14. Extracted residual stress versus the variation of (a) inclination angle α of the supports and (b) boundary torsion stiffness k_T.

In the complete model for the inclined supports in fixed-fixed beams, the boundary torsional stiffness k_T is not constant, but is a function of both the beam displacements and residual stress, as shown in Fig. 3.15. In the reduced-order numerical model, the most time-consuming step the is calculation of the beam's eigenmodes and eigenfrequencies for given boundary conditions and residual stress. Since k_T is calculated numerically which involves iterative computing of eigenmodes and eigenfrequencies, the stress extraction wouldn't be computationally efficient if the exact value of k_T is calculated at each displacement with each assumed residual stress in the iterative simulations. For this particular beam used for uncertainty analysis, with an initial

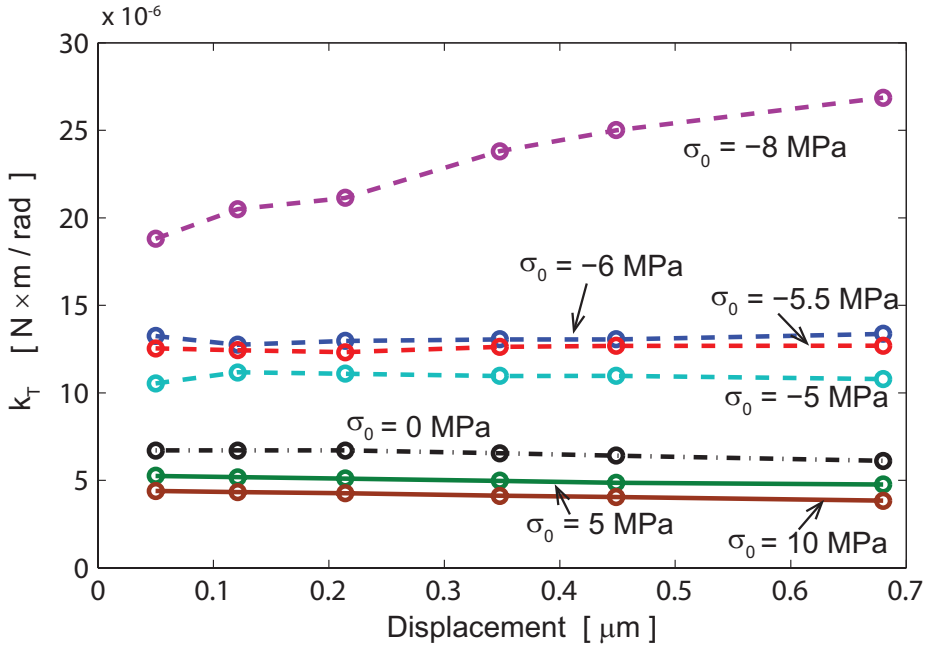

Fig. 3.15. The boundary torsion stiffness k_T as a function of beam displacements at different residual stresses.

stress value of −5 MPa assumed for the optimization code, the extraction of residual stress is −5.7 MPa, and it takes 7 hours and 48 minutes. Therefore, it is desirable that a constant torsion spring stiffness can be used without greatly compromising the accuracy of the extracted residual stress. If a constant torsion spring stiffness is used, the variation of the extracted residual stress due to the torsion-spring stiffness (k_T) is shown in Fig. 3.14(b). It shows that if k_T is small enough or large enough, the extracted residual stress is not sensitive to k_T. For the beams in our study, k_T falls within the range from $10^{-}6$ N×m/rad to $10^{-}5$ N×m/rad, which is large enough so that a constant value of k_T can be used to improve efficiency of the stress extraction. We choose to calculate the value of k_T for zero residual stress at the largest displacement. This simplification reduces the time of stress extraction by 24× with a result of −5.5 MPa which is 0.2 MPa smaller compared with the result when the complete model for the inclined supports is used. Therefore, it is valid that a constant torsional boundary stiffness for extracting residual stress.

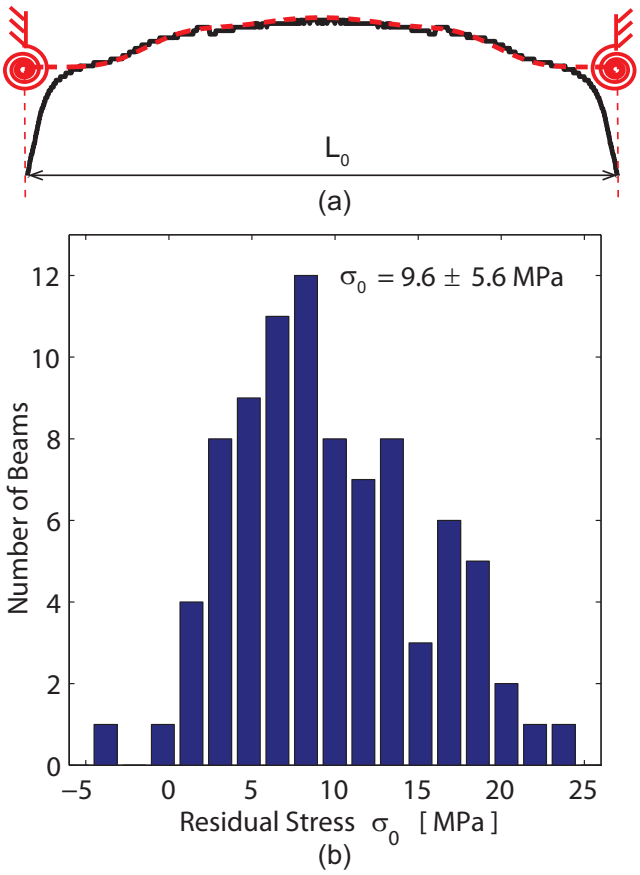

Fig. 3.16. (a) Beam model with vertical support model in [45], and (b) histogram of extracted values of residual stress σ_0 using vertical beam model in (a).

If the inclination of the supports is neglected and α is assumed to be 90°, the effective length is misinterpreted as the nominal design value ($L_{eff} = L_0$), as shown in Fig. 3.16(a). Using a boundary torsion stiffness calculated for vertical supports in [45], the mean value of extracted residual stresses for 87 beams increases to 9.6 MPa (Fig. 3.16(b)). Furthermore, if an ideal boundary model, as shown in Fig. 3.17(a), is used ($L_{eff} = L_0$, $k_T \to \infty$), the histogram for 87 beams plotted in Fig. 3.17(b) shows the mean value of the resulting residual stress extracted increases to 9.4 MPa.

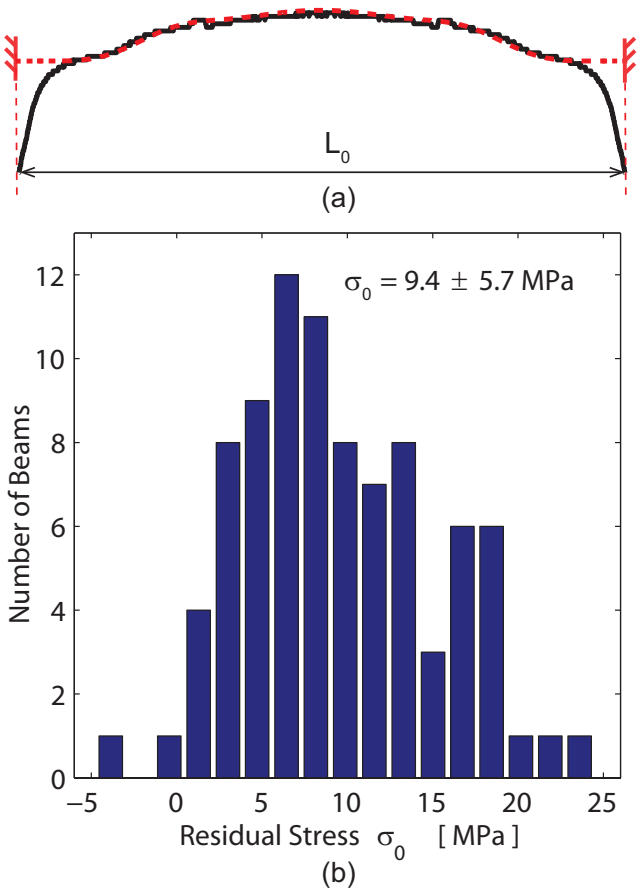

Fig. 3.17. (a) Beam model with ideally fixed boundary, and (b) histogram of extracted values of residual stress σ_0 using the beam model in (a).

3.6 Conclusion

A wafer-scale technique for extracting residual stress has been developed which employs a reduced-order computationally efficient beam model and requires only one beam itself for the extraction. Accurate extraction results are achieved by simultaneously incorporating non-idealities such as inclined supports, non-flat beam profiles and fringing fields in the reduced-order numerical model. Through the use of a custom scripting automation program, the geometries and displacement-voltage curves of fixed-fixed beams are measured using a confocal microscope. This technique has

been demonstrated by applying to 87 nickel beams on a 4-inch quarter wafer piece. For all the extracted residual stress, the distribution with respect to the location and the statistic distribution has been presented. The uncertainty analysis shows that accurate geometric measurements, especially the beam thickness and gap, and a comprehensive modeling of non-idealities are necessary to achieve accurate quantification of residual stresses.

4. UNIFORM MICRO-CORRUGATED DIAPHRAGM DESIGN FOR STRESS TOLERANT MEMS TUNERS

4.1 Introduction

Widely tunable filters with low insertion loss are essential components in realizing reconfigurable RF-front ends. Evanescent-mode cavity resonators/filters have been successfully demonstrated recently with advantages of wide tuning range, high quality factor, small size, and high power handling capability [18, 19, 21, 87]. It is evident in literature that resonant behavior for evanescent modes which is below the cutoff of the cavity waveguide is possible if appropriate loading conditions can be realized [88, 89]. Fig. 4.1 shows the side view of an evanescent-mode cavity resonator schematically. The conductor-walled cylinder cavity is loaded by a conductive post that serves as an effective shunt capacitor whose capacitance is determined by the gap between the post and the ceiling diaphragm. The post and the cavity sidewall can be modeled as a shorted coaxial line to provide an effective inductor [88, 90]. The resonant frequency is determined by the equivalent capacitance and inductance. Therefore, frequency tuning can be achieved by a diaphragm tuner which can be used to change the gap between the post and the diaphragm. Electrostatically actuated diaphragm tuner is favored for its high precision, high reliability, and near-zero hysteresis [90]. In the design of the electrostatic MEMS tuner, important parameters include tuning range, actuation voltage, and temperature stability [90]. In this chapter, we focus on the design optimization to achieve high tuning range while maintaining low actuation voltage. Temperature stability issue will be tackled in the next chapter.

The pull-in instability of electrostatic actuation dictates that the diaphragm cannot be continuously tuned through the entire gap between the diaphragm and bias

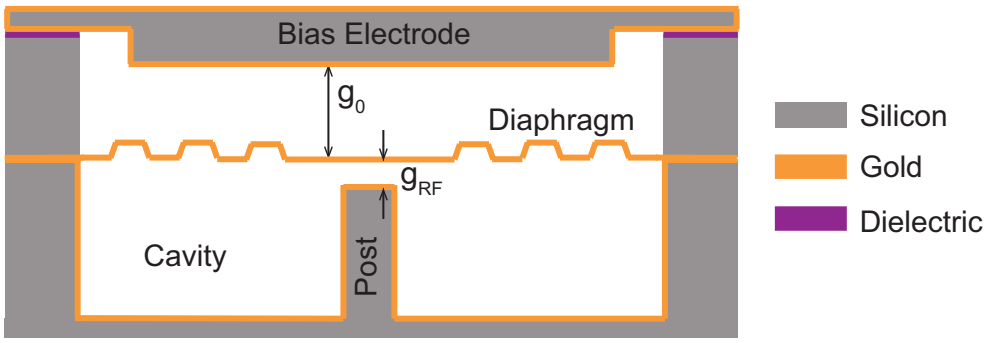

Fig. 4.1. Schematic side view of the tunable evanescent-mode resonator with capacitive RF MEMS tuner.

electrode. The maximum displacement the diaphragm can travel directly relates to the tuning ratio of the resonator which is roughly given by:

$$R_{max} \approx \sqrt{\frac{g_{RF} + w_m}{g_{RF}}} \tag{4.1}$$

where g_{RF} is the initial gap between the diaphragm and the capacitive post, and w_m is the maximum diaphragm displacement before pull-in occurs.

Given $g_{RF} = 2$ μm, to achieve a tuning ratio of $> 3:1$, a minimum w_m of 16 μm is required. Such large deflections present challenges to the design of the MEMS tuner especially when a reasonably low actuation voltage is required. Such large displacements many induce excessively high stretching in flat diaphragms which results in large stiffness and nonlinear behavior. In addition, the stiffness of a flat diaphragm is a strong function of the residual stress which is often unavoidable in fabrication process [7]. The large stiffness of the diaphragm also leads to a high actuation voltage of the tuner.

Corrugated diaphragms have been employed to alleviate the stress stiffening problem of flat diaphragms under residual stress and at large displacements [21, 91]. The corrugated structure elongates the profile length in the radial direction and thus effectively reduces the stretching stiffness in the radial direction due to residual stress and large displacements. Due to the geometric complexity of corrugated diaphragms,

only limited analytical models have been proposed for the prediction of the stiffness with respect to geometric parameters.

In this chapter, the stress-reduction effects of corrugated diaphragms are investigated through a systematic parametric study based on finite-element-model (FEM) simulations. The relationship between the stiffness of corrugated diaphragms and the geometric design of corrugations is investigated, and optimal designs are discussed.

4.2 Capacitive MEMS Tuner with Nonlinear Diaphragm Deformations

4.2.1 Linear and Nonlinear Stiffness of Diaphragms

For diaphragms designed to operate in the large deflection regime, both linear and nonlinear effects need to be investigated. In the case of small deflections, bending stiffness dominates and the load-deflection behavior can be described by a linear stiffness coefficient k_1. As deflection increases, the stretching-induced stress of the diaphragm can no longer be neglected. This stretching stiffness causes the nonlinearity in the large deflection regime and therefore, a nonlinear stiffness coefficient k_3 is introduced to account for this nonlinearity. In general, for a diaphragm with a radius R and under a uniformly distributed pressure P, the load-deflection behavior can be approximated by the following relationship [92]:

$$F_m = k_1(w - w_0) + k_3(w - w_0)^3 \tag{4.2}$$

where $F = \pi R^2 P$ is the total loading force on the diaphragm, w is the center displacement of the diaphragm, and w_0 is the residual-stress-induced initial center deflection. The stiffness coefficients k_1 and k_3 are functions of the diaphragm's geometry and material properties. The in-plane residual stress adds resistance to bending, and therefore, changes the linear stiffness coefficient k_1.

4.2.2 Analytical Models

The analytical models found in the literature for corrugated diaphragms are reviewed in this section. Fig. 4.2 shows common shapes of corrugation profiles. A list of important parameters for all corrugation shapes is as follows:

R	diaphragm radius
h	diaphragm radius
H_c	corrugation depth
R_c	radius of corrugated area from the anchor
L_c	corrugation wavelength
s	profile length of each corrugation

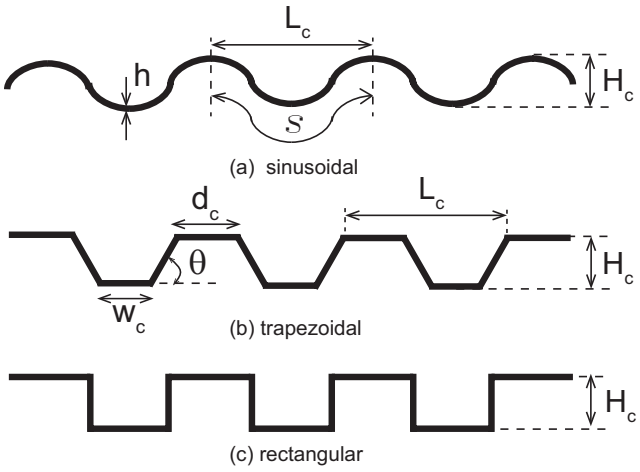

Fig. 4.2. Common shapes of corrugation profiles.

The effect of residual stress σ_r on the diaphragm stiffness has been investigated and the existing analytical models are summarized in Table 4.1.

Analytical Model for Flat Diaphragms

The case of a flat diaphragm is included as a comparison with the micro-corrugated diaphragms. For a flat circular diaphragm, which has clamped edges and without

Table 4.1.
Analytical models for stiffness of corrugated diaphragms.

	Analytical k_1 Models			Analytical k_3 Model
Model #	#1	#2	#3	–
Assumptions	$\sigma_r = 0$	$\sigma_r > 0$	$\sigma_r >> 0$	independent of σ_r
	$R_c \geq 0.85R$, independent of R_c		Any $R_c < R$ small H_c	$R_c \geq 0.85R$, independent of R_c
	sinusoidal corrugations		trapezoidal corrugations	sinusoidal corrugations

initial stress, the relationship between a uniform pressure P and the resulting center deflection w can be expressed by [92]:

$$\frac{PR^4}{Eh^4} = \frac{16}{3\left(1-\nu^2\right)}\left(\frac{w}{h}\right) + \frac{7-\nu}{3\left(1-\nu\right)}\left(\frac{w}{h}\right)^3 \tag{4.3}$$

where E, ν , R and h are the Young's modulus, Poisson's ratio, radius and thickness of the diaphragm, respectively. It can be seen from (4.3) that for small deflections ($w/h << 1$) the load-deflection is approximately linear. The nonlinear term becomes larger as the deflection increases.

With a tensile residual stress of σ_r, the general load-deflection expression in (4.3) is modified to account for the bending resistance due to the residual stress by adding an extra term, expressed as [7]:

$$\frac{PR^4}{Eh^4} = \left[\frac{16}{3\left(1-\nu^2\right)} + \frac{4R^2}{(1-\nu)Eh^2}\sigma_r\right]\left(\frac{w}{h}\right) + \frac{7-\nu}{3\left(1-\nu\right)}\left(\frac{w}{h}\right)^3 \tag{4.4}$$

The tensile residual stress in a flat diaphragm will not cause any out-of-plane displacement ($w_0 = 0$). The stiffness coefficients for flat diaphragms can be derived by recording (4.4):

$$k_1 = k_1' + k_1'' = \frac{16Eh^3\pi}{3\left(1-\nu^2\right)R^2} + \frac{4h\pi}{(1-\nu)}\sigma_r \tag{4.5}$$

$$k_3 = \frac{(7-\nu)Eh\pi}{3\left(1-\nu\right)R^2} \tag{4.6}$$

Analytical Model for Corrugated Diaphragm without Residual Stress

The available theory of the general load-deflection characteristics for a periphery-clamped circular corrugated diaphragm was derived based on the assumption that the diaphragm has negligible flat center zone ($R_c \geq 0.85R$) and has a sinusoidal corrugation profile [92, 93]. It is also assumed that there is no residual stress ($\sigma_r = 0$) in the diaphragm and thus there is no stress-induced initial deflection ($w_0 = 0$). The load-deflection equation is:

$$\frac{PR^4}{Eh^4} = A_p\left(\frac{w}{h}\right) + B_p\left(\frac{w}{h}\right)^3 \tag{4.7}$$

where A_p is the dimensionless linear coefficient of stiffness and B_p is the dimensionless non-linear tension coefficient especially defined for corrugated diaphragms as follows:

$$A_p = \frac{2(3+q)(1+q)}{3(1-\nu^2/q^2)} \tag{4.8}$$

$$B_p = \frac{32}{q^2-9}\left[\frac{1}{6} - \left(\frac{3-\nu}{(q-\nu)(q+3)}\right)\right] \tag{4.9}$$

and the corrugation profile factor q is determined by the corrugation depth H_c, corrugation spatial wavelength L_c and profile length for each corrugation s [92]:

$$q = \sqrt{\frac{s}{L_c}\left(1 + 1.5\frac{H_c^2}{h^2}\right)} \tag{4.10}$$

where s/L_c for a trapezoidal corrugation profile shown in Fig. 4.2(b) is:

$$\frac{s}{L_c} = \frac{L_c - 2H_c/\tan\theta + 2H_c/\sin\theta}{L_c} \tag{4.11}$$

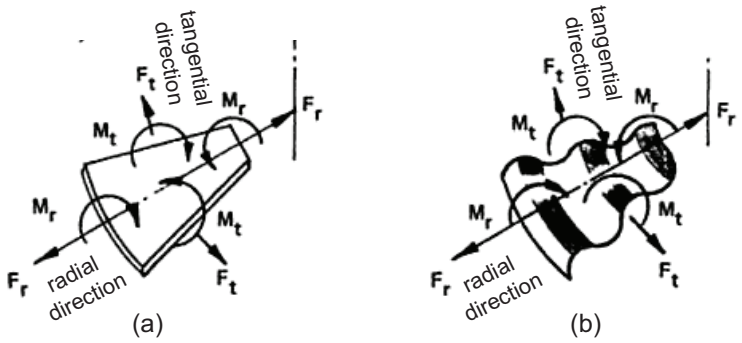

Fig. 4.3. An element of a (a) flat diaphragm and (b) corrugated diaphragm showing the bending and stretching in both radial and tangential directions [92].

While (4.10) is derived for a sinusoidal corrugation profile, for shallow corrugations, the shape of the corrugations has little influence on the profile factor q and the performance characteristics of the diaphragm [92].

The stiffness coefficients based on the analytical model in (4.7) are:

$$k_1 = k_1' = \frac{Eh^3\pi}{R^2} A_p \tag{4.12}$$

$$k_3 = \frac{Eh\pi}{R^2} B_p \tag{4.13}$$

As shown in Fig. 4.3, when loads are applied, the diaphragms are bent in both the radial and tangential directions. In the tangential direction, the bending stiffness of a corrugated diaphragm is much larger than that of a flat diaphragm. On the other hand, the stretching stiffness in the radial direction of a corrugated diaphragm is much smaller than that of a flat diaphragm. Therefore, when there is no residual stress, a corrugated diaphragm has a larger linear stiffness coefficient k_1 and a smaller nonlinear stiffness, compared to the case of a flat diaphragm in (4.5).

Analytical Model for Stress Reduction Effect of Corrugated Diaphragm

Although the deposition conditions are carefully controlled to lower the residual stress, extremely low stress ($\leq$5 MPa) is very difficult to achieve [7]. For both flat

and corrugated diaphragms, a tensile stress increases the resistance to bending (higher linear stiffness), while a compressive stress makes the diaphragms easier to bend and causes buckling when it exceeds a critical value. Typical micro-fabrication techniques result in tensile residual stress of a few tens of MPa [94], which has a nonnegligible influence on the stiffness of the diaphragms, and therefore, needs to be taken in to account. Despite the increased bending stiffness in the tangential direction due to the corrugated structure, it has been shown that when an initial residual stress exists, the corrugations can effectively reduce the stress stiffening effect from the residual stress. Therefore, a corrugated diaphragm with residual stress has lower stiffness than a flat diaphragm with the same residual stress for given geometric parameters and material properties [95–97]. Stress reduction of the corrugated structures has been investigated by Scheeper [98] and Fuldner [99]. Due to the complexity of corrugated diaphragm structures, these analytical models only provide rough estimations of the linear stiffness of corrugated diaphragms with residual stress. The nonlinear coefficients are assumed to be independent of residual stress.

In [98], a corrugated diaphragm with tensile residual stress σ_r is treated as the superposition of a linear model of a corrugated diaphragm without residual stress, and the linear flat diaphragm model with a reduced initial tensile stress $\sigma_r B_p/2.83$. The superposition is based on the assumption that the corrugated diaphragm can be approximated by a fictitious flat diaphragm, which locally has the same radial and tangential bending rigidity as the corrugated diaphragm, and the superposition is only valid in the linear regime. The deflection of a corrugated diaphragm with a residual stress σ_r in the linear regime was approximated by:

$$P = 4\frac{h^2}{R^2}\frac{w}{h}\left(\sigma_r\frac{B_p}{2.83} + \frac{A_p}{4}E\frac{h^2}{R^2}\right) \tag{4.14}$$

where A_p and B_p are defined in (4.8) and (4.9), respectively. Therefore, the linear stiffness coefficient is:

$$k_1 = k_1' + k_1'' = \frac{Eh^3\pi}{R^2}A_p + \frac{4\pi h B_p}{2.83}\sigma_r \tag{4.15}$$

In [99], a stress reduction ratio of a corrugated diaphragm with a trapezoidal profile is derived mathematically. The diaphragm is partially corrugated with N corrugations. This derivation assumes the corrugation depth H_c is much smaller than the bottom width of the trapezoidal profile w_c. A stress reduction ratio η is given by:

$$\eta = 1 + 6\sin(\theta)\left(\frac{H_c}{h}\right)^2 \frac{N w_c}{R - N(w_c + d_c)} \tag{4.16}$$

where θ is the sidewall angle of the trapezoidal corrugations and w_c, d_c are the corrugation width and distance of the trapezoidal profile, respectively.

This model assumes a high residual stress and shallow corrugations, and thus the increased bending stiffness due to corrugations in the tangential direction can be neglected. The corrugated diaphragm with residual stress σ_r is then approximated by a flat diaphragm with a reduced stress σ_r/η in equilibrium, and the linear stiffness is only determined by the stress as follows:

$$k_1 = k_1'' = \frac{4\pi h \sigma_r}{\eta} \tag{4.17}$$

These two analytical models for the stress-reduction effect of corrugated diaphragms neglect the stress-induced initial offset w_0. These analytical models will be compared to FEM simulations and their limitations are discussed in Section 4.4.

4.2.3 Electrostatic Tuning of Diaphragms with Nonlinearity

The capacitive MEMS tuner can be continuously tuned electrostatically when the actuation voltage is lower than the pull-in voltage (V_{pi}). It is in general desirable to keep the actuation voltage at a reasonably low value. The tuning range of the MEMS tuner is determined by the maximum displacement the diaphragm travels before pull-in occurs. The pull-in voltage and tuning range of MEMS tuners are derived in this section.

With the parallel plate capacitance approximation, the electrostatic force acting on the diaphragm for an actuation voltage V is given by [7]:

$$F_e = \frac{\varepsilon_0 \varepsilon_r \pi R^2 V^2}{2(g_0 - w)^2} \tag{4.18}$$

where ε_0 is the free-space permittivity, ε_r is the relative permittivity ($\varepsilon_r = 1$ for air), w is the center deflection of the diaphragm, and g_0 is the initial gap between the electrode and the diaphragm (as shown in Fig. 4.1). The mechanical restoring force of the diaphragm is given by (4.2) and the total force on the diaphragm should be zero:

$$F = F_e - F_m = \frac{\varepsilon_0 \varepsilon_r \pi R^2 V^2}{2\left(g_0 - w\right)^2} - \left[k_1(w - w_0) + k_3(w - w_0)^3\right] = 0 \tag{4.19}$$

By introducing the normalized parameters $\hat{w} = w/g_0$, $\hat{w}_0 = w_0/g_0$, $\hat{k}_1 = k_1 g_0$, and $\hat{k}_3 = k_3 g_0^3$, (4.19) can be re-written as:

$$F = \frac{\varepsilon_0 \varepsilon_r \pi R^2 V^2}{2g_0^2\left(1 - \hat{w}\right)^2} - \left[\hat{k}_1(\hat{w} - \hat{w}_0) + \hat{k}_3(\hat{w} - \hat{w}_0)^3\right] = 0 \tag{4.20}$$

When the displacement of the diaphragm increases to w_m, the restoring force cannot balance the electrostatic force and the pull-in phenomenon occurs. At the maximum tuning displacement $w = w_m$, the following equations are satisfied [7]:

$$\left.\frac{\partial F}{\partial \hat{w}}\right|_{\hat{w}=\hat{w}_m} = 0 \tag{4.21}$$

where $0 < \hat{w}_m = w_m/g_0 < 1$ is the tuning range of the diaphragm. By substituting (4.20) into (4.21), we can solve for $\hat{w}_m$ by:

$$\frac{2\left[\hat{k}_1(\hat{w}_m - \hat{w}_0) + \hat{k}_3(\hat{w}_m - \hat{w}_0)^3\right]}{1 - \hat{w}_m} = \left[\hat{k}_1 + 3\hat{k}_3(\hat{w}_m - \hat{w}_0)^2\right] \tag{4.22}$$

The maximum tuning displacement w_m is usually designed to be $> 10\mu$m for the evanescent-mode resonator/filter application. The stress-induced initial offset w_0 is $\sim$ 1-2 μm for a tensile stress of a few tens of MPa. We learn from (4.22) that when the nonlinear behavior of the diaphragm is dominant ($\hat{k}_3 >> \hat{k}_1$), $\hat{w}_m \to 3/5$; and when the linear behavior is dominant ($\hat{k}_3 << \hat{k}_1$), $\hat{w}_m \to 1/3$. The tuning range of the diaphragm ($\hat{w}_m = w_m/g_0$) is a function of the normalized nonlinear to linear stiffness coefficients ratio ($\hat{k}_3/\hat{k}_1$) as shown in Fig. 4.4.

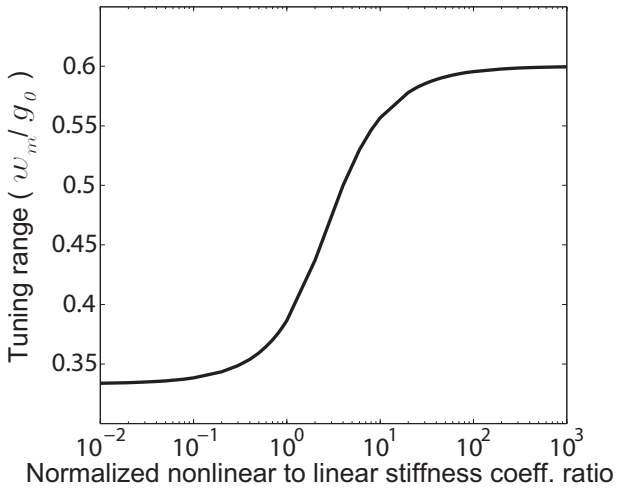

Fig. 4.4. Tuning range (w_m/g_0) versus the normalized nonlinear to linear stiffness coefficients ratio ($\hat{k_3}/\hat{k_1}$).

After determining the tuning range $\hat{w}_m$, we can substitute it back into (4.20) and solve for the pull-in voltage V_{pi}:

$$V_{pi} = \sqrt{\frac{2g_0^2\left(1-\hat{w}_m\right)^2\left[\hat{k}_1(\hat{w}-\hat{w}_0)+\hat{k}_3(\hat{w}-\hat{w}_0)^3\right]}{\varepsilon_0\varepsilon_r\pi R^2}} \tag{4.23}$$

In order to satisfy the design requirements for the tuning range and action voltage, we need to carefully choose the initial gap g_0 and design the diaphragm with proper stiffness.

4.3 Finite Element Model for Corrugated Diaphragms

4.3.1 Simulation Setup for Parametric Study

Due to the complex 3-D geometry of the corrugated diaphragm, FEM simulations are performed using ANSYS Parametric Design Language (APDL) [53]. The script-based simulation allows ANSYS program to be linked with MATLAB [83] program for systematically changing the geometric parameters of corrugated diaphragms as shown in the flowchart in Fig. 4.5 [100]. In this way, the parametric study can be performed efficiently.

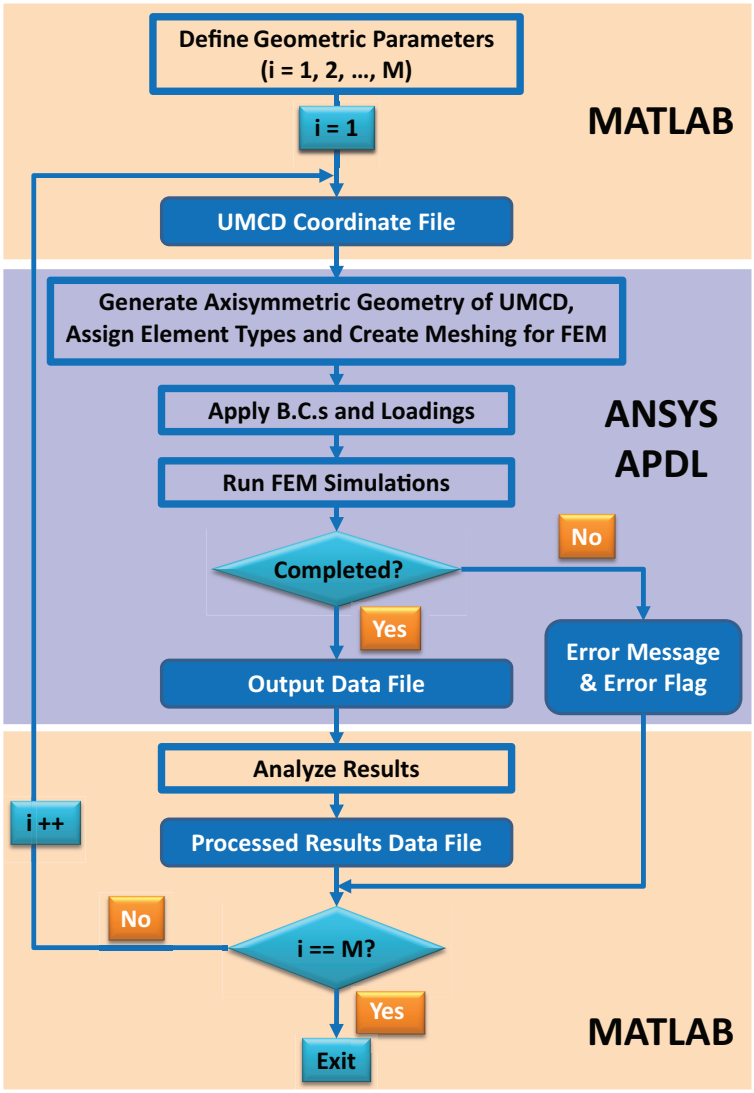

Fig. 4.5. Flow chart of parametric study for corrugated diaphragm stiffness based on FEM simulations.

In order to reduce the computation time, the axisymmetry of the diaphragm is utilized by choosing a higher order 2-D, 8-node element PLANE183 with the axisymmetric option activated. In the simulations, only the trapezoidal corrugations are considered and a meshed axisymmetric model for a corrugated diaphragm is shown in Fig. 4.6. Appropriate boundary conditions are assigned: the surface where the

diaphragm attached to the substrate at the outter rim edge of the diaphragm is fixed in both horizontal direction (x-axis) and vertical direction (y-axis).

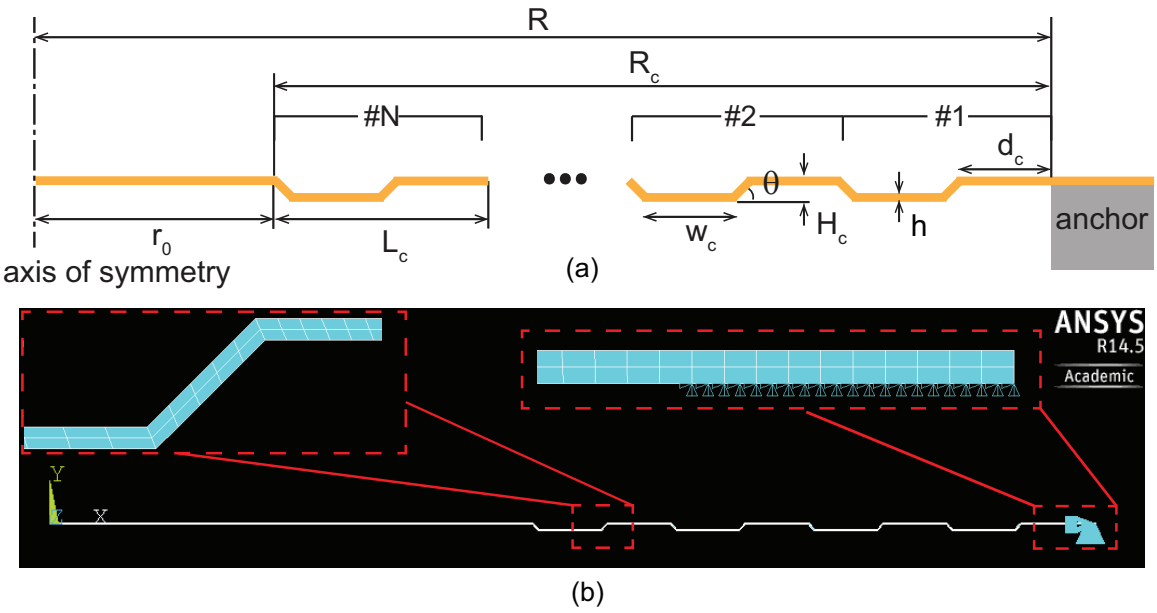

Fig. 4.6. (a) Schematic model for micro-corrugated diaphragm showing the geometric parameters, and (b) finite element model in ANSYS showing the axisymmetric element and meshing.

The geometric and material properties assumed in the simulations are listed in Table 4.2, unless stated otherwise. The stiffness coefficients can be extracted by fitting (4.2) to the simulated load-deflection curves, as shown by the example in Fig. 4.7.

4.3.2 Comparison of FEM with Analytical Models

The stiffness of corrugated diaphragms from the analytical models summarized in Table 4.1 are compared to FEM simulations for diaphragms both with and without residual stress.

Table 4.2.
Dimensions and material properties used in FEM simulations for micro-corrugated diaphragms.

	Parameter	Value
Geometric Attributes	Radius R	900 μm
	Thickness h	1 μm
	Corrugation Depth H_c	5 μm
	Corrugation Range R_c	400 μm
	Corrugation Wavelength L_c	100 μm
	Corrugation Number N	4
	Corrugation Sidewall Angle θ	45 $^\circ$
	Corrugation width (w_c)	$\frac{1}{2}\left(L_c - 2H_c/\tan\theta\right)$
	Corrugation distance (d_c)	$\frac{1}{2}\left(L_c - 2H_c/\tan\theta\right)$
Material Properties	Young's Modulus E	57 GPa
	Poisson's ratio ν	0.42
	Residual Stress σ_r	30 MPa

Corrugated Diaphragms without Residual Stress

First, in the case of stress-free corrugated diaphragms, the analytical k_1 model #2 regresses to model #1, but model #3 will generate zero linear stiffness since it assumes that the linear stiffness only depends on the stress term. Therefore, for linear stiffness coefficient, only the k_1 model #1 in (4.12) is compared to the extracted results from the FEM simulations. In addition, the k_1 model #1 and the k_3 model assume that the corrugations span almost across the whole diaphragm ($R_c \geq 0.85R$), and therefore, $R_c = 800$ μm is used in simulations.

The stiffness coefficients are plotted for different corrugation depths in Fig. 4.8. A zero corrugation depth implies a flat diaphragm. The model by (4.12) underestimates

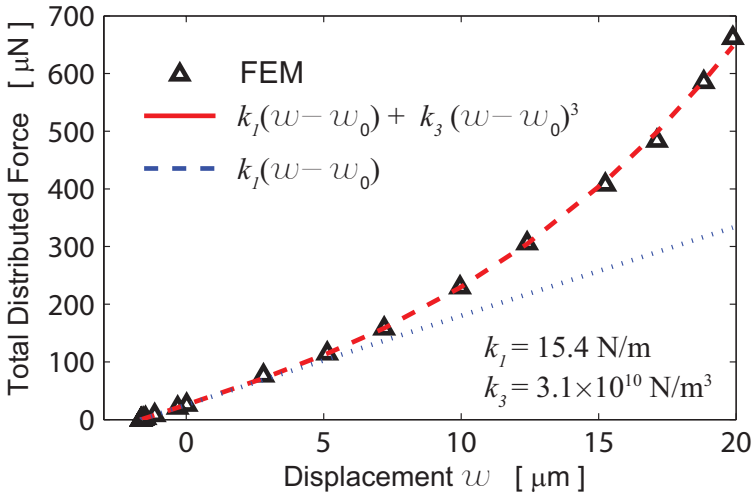

Fig. 4.7. An example of load-deflection curve and curve fitting for extracting linear and nonlinear stiffness coefficients.

the linear stiffness coefficient k_1 and yields an error of $\sim 45\%$ at $H_c = 5$ μm. This difference might be due to the fact that the analytical model assumes a sinusoidal corrugation shape, while trapezoidal corrugations are used in FEM simulations. The nonlinear coefficient from (4.13) agrees with FEM results well in this case.

From (4.12) and (4.13), we learn that the only decisive geometry-related parameter for the analytical stiffness coefficients of stress-free corrugated diaphragms is the corrugation profile factor q, which highly depends on H_c/h, and is not related to R_c. However, FEM simulations show that both k_1 and k_3 vary with the range of the corrugations R_c (Fig. 4.9). FEM results in Fig. 4.10 show that the stiffness coefficients are less sensitive to the change of the corrugation wavelength with a fix range of corrugations. From (4.11), we know that the corrugation profile factor $q \approx 1$ for shallow corrugations, and therefore, the change of L_c will not affect the stiffness coefficient significantly.

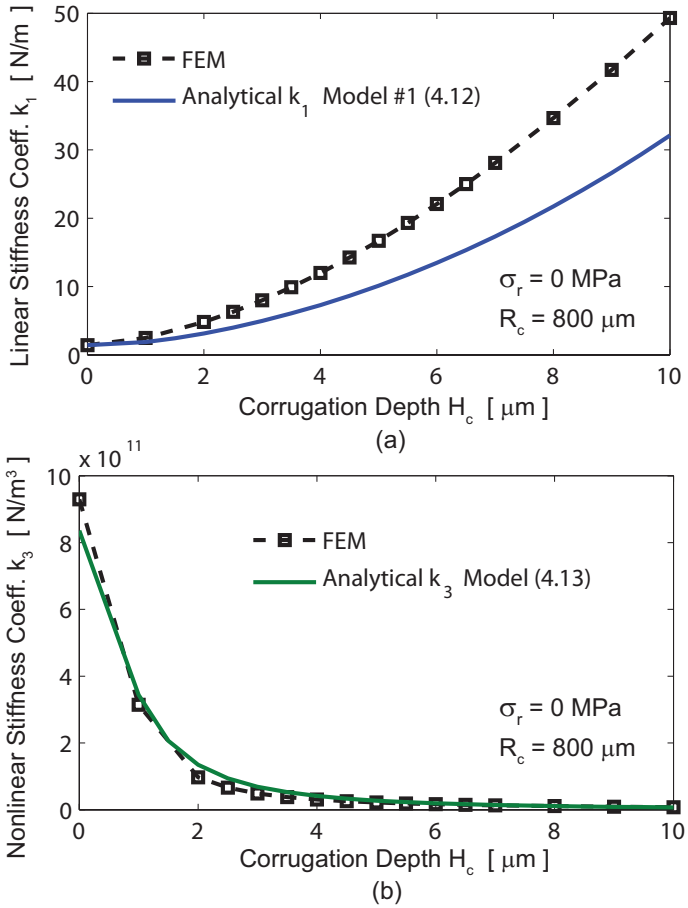

Fig. 4.8. Comparison of FEM and analytical model for (a) linear stiffness coefficient and (b) nonlinear stiffness coefficient versus corrugation depth H_c with $\sigma_r = 0$ MPa and $R_c = 800$ μm.

Corrugated Diaphragms with Residual Stress

With the presence of residual stress, (4.12) is not valid since the assumption $\sigma_r = 0$ doesn't holds, and therefore, only the analytical k_1 models in (4.15) and (4.17) are compared with FEM results. For the nonlinear stiffness coefficient k_3, it is assumed to be independent of the residual stress, and thus (4.13) is also used for the diaphragms with residual stress. It is worth to notice that in all analytical models, the stress-induced deformation of the diaphragm is neglected. However, the corrugated

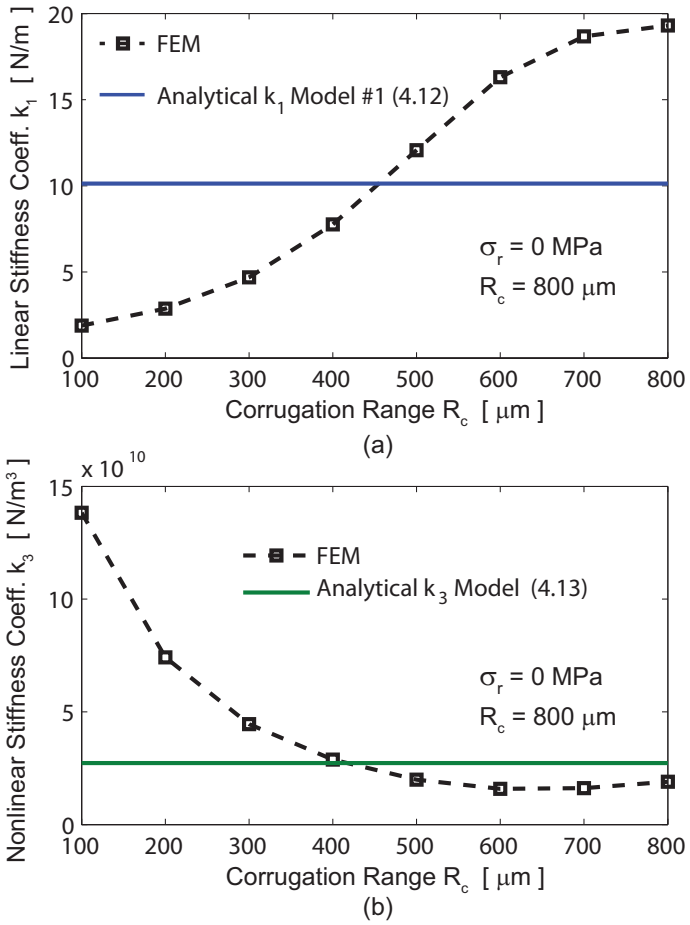

Fig. 4.9. Comparison of FEM and analytical model for (a) linear stiffness coefficient and (b) nonlinear stiffness coefficient versus corrugation range R_c with $\sigma_r = 0$ MPa and $R_c = 800$ μm.

diaphragm cannot keep its initial corrugated shape due to the residual stress, and this deformation may affect the stiffness of the diaphragm.

The linear and nonlinear stiffness coefficients from analytical models are compared with FEM results with varying corrugation depth in Fig. 4.11. For small H_c, the analytical k_1 models in (4.15) and (4.17) both show that larger H_c has higher stress reduction effect and thus lower k_1, which agrees with the trend of FEM simulations shown in Fig. 4.11(a). If H_c increases further, k_1 model #2 and the FEM results show slight increase of k_1, which is due to the increasing bending stiffness of the corrugations in tangential direction. Since k_1 model #3 only accounts for the stiffness caused by

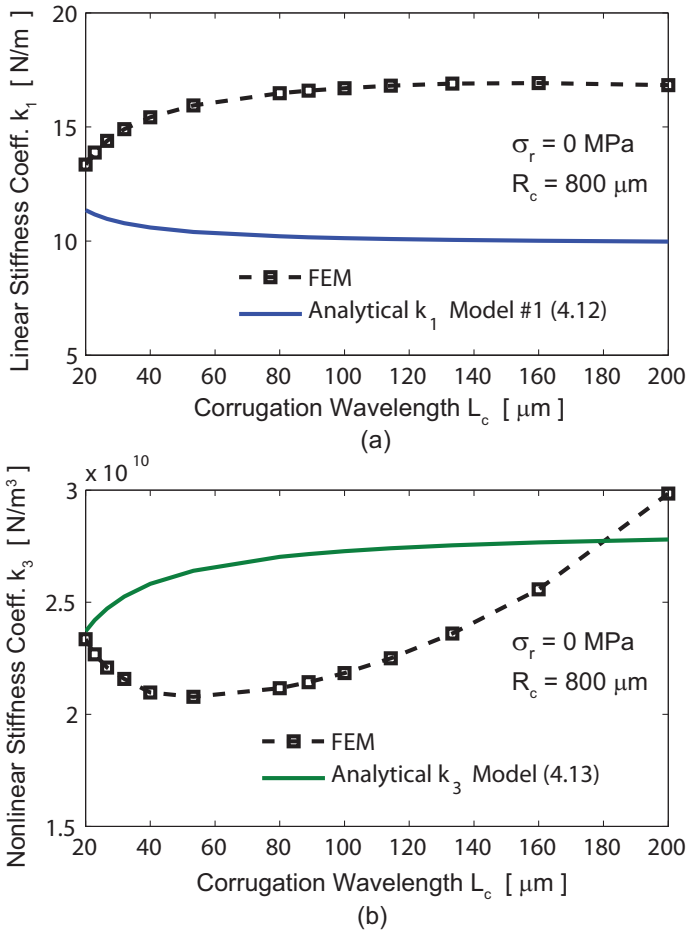

Fig. 4.10. Comparison of FEM and analytical model for (a) linear stiffness coefficient and (b) nonlinear stiffness coefficient versus corrugation wavelength L_c with $\sigma_r = 0$ MPa and $R_c = 800$ μm.

the residual stress while neglecting the stiffness due to the corrugations, it cannot predict this trend. Although the nonlinear stiffness k_3 is assumed to be independent of residual stress, FEM simulations in Fig. 4.11(b) indicate that k_3 does increase if there is a tensile residual stress, especially when H_c is small. Therefore, (4.13) cannot be applied to the case of stressed diaphragm with shallow corrugations.

In Fig. 4.12, when the corrugation range R_c increases up to 400 μm, both simulated k_1 and k_3 decrease, but k_1 increases if the corrugations span a larger range $R_c >$ 400 μm due to the increase bending stiffness of the corrugations. The results from

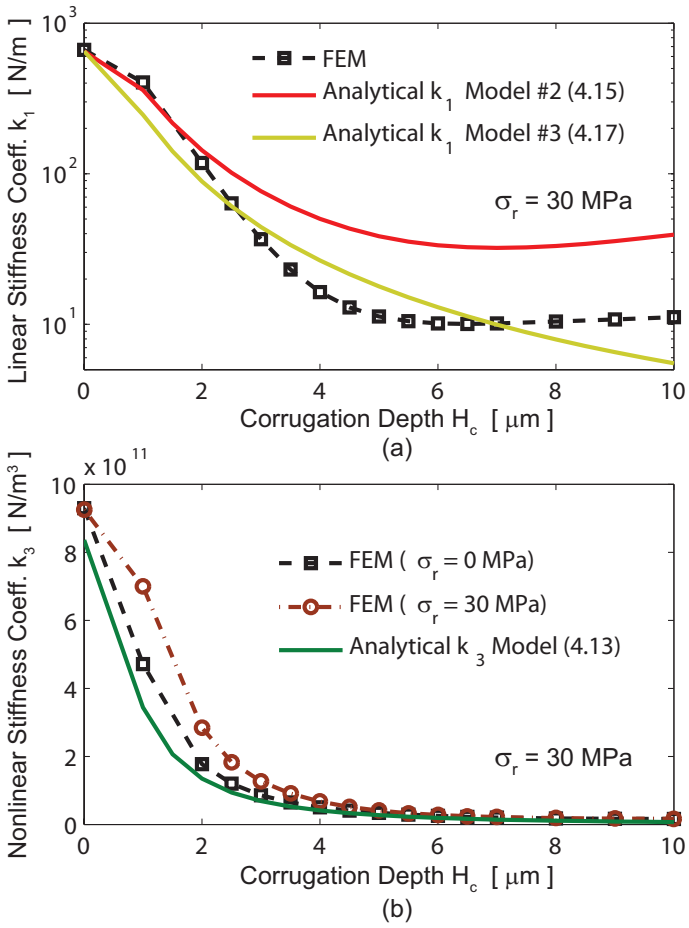

Fig. 4.11. Comparison of FEM and analytical model for (a) linear stiffness coefficient and (b) nonlinear stiffness coefficient versus corrugation depth H_c with $\sigma_r = 30$ MPa.

(4.15) and (4.13) are constant since R_c is not a variable included in two equations, but they provide close approximation to FEM simulations for larger R_c where the assumption $R_c \geq 0.85R$ holds. The result by (4.17) shows the same trend as FEM simulations for $R_c < 400$ μm, but it shows further increase of k_1 for larger R_c since it neglects the stiffness due to the corrugations.

The effects of different corrugation wavelengths are studied for two cases of fixed corrugation range: $R_c = 400$ μm, and $R_c = 800$ μm, as plotted in Fig. 4.13 and Fig. 4.14, respectively. The analytical results by (4.15) and (4.13) are closer to FEM simulations for the case of $R_c = 800$ μm since it satisfies the assumption of $R_c \geq 0.85R$.

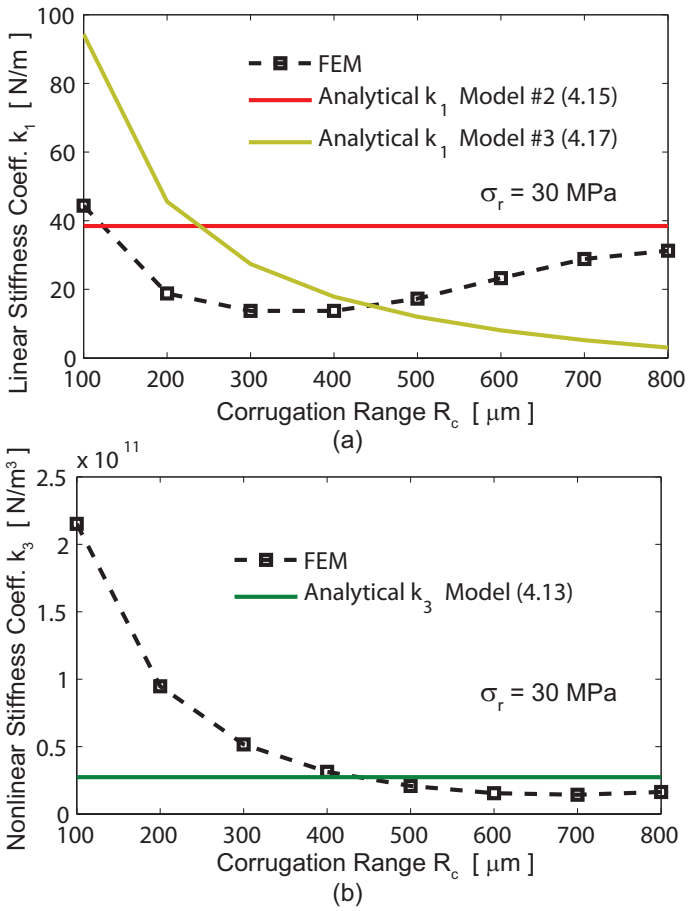

Fig. 4.12. Comparison of FEM and analytical model for (a) linear stiffness coefficient and (b) nonlinear stiffness coefficient versus corrugation range R_c with $\sigma_r = 30$ MPa.

But (4.17) shows closer approximation simulation for the case of $R_c = 400$ μm since further increase of R_c will lead to larger bending stiffness of corrugations which is neglected in the model by (4.17). Furthermore, (4.17) is derived based on the beam theory instead of the plate theory. Therefore, it cannot model the effect of L_c well.

In conclusion, because of the assumptions and simplifications made in analytical models, they cannot simultaneously model the effects of all geometric parameters and the residual stress accurately. To systematically study the effects of geometric parameters for design optimization, a parametric study based on FEM simulations is performed.

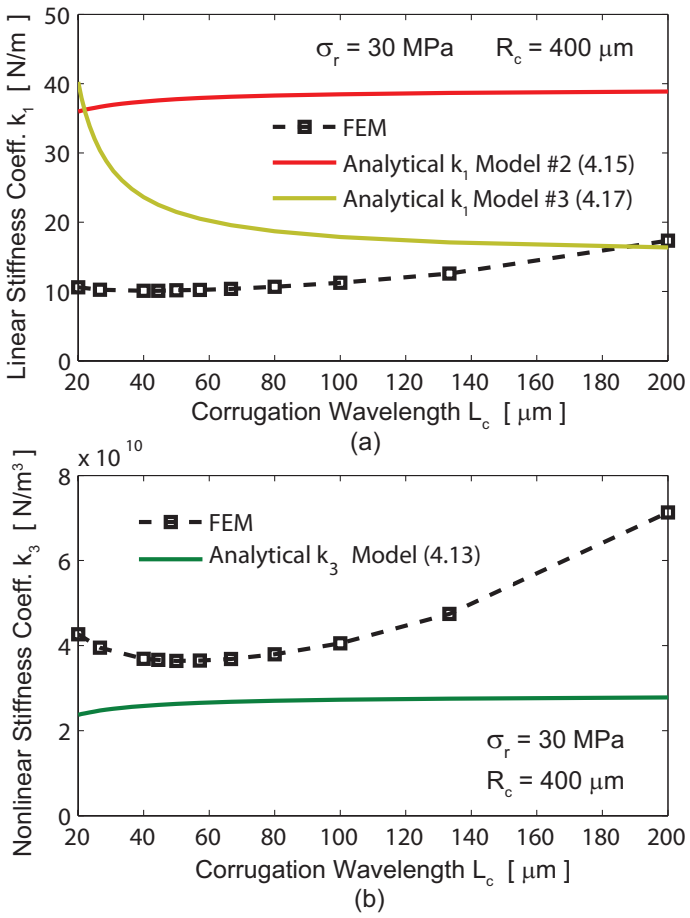

Fig. 4.13. Comparison of FEM and analytical model for (a) linear stiffness coefficient and (b) nonlinear stiffness coefficient versus corrugation wavelength L_c with $\sigma_r = 30$ MPa and $R_c = 400$ μm.

4.4 Parametric Study for Design Optimization

In this section, a parametric study of the uniform micro-corrugated diaphragm is performed to show the dependence of diaphragm stiffness on geometric parameters. The parametric study provides guidelines for design optimization of low-voltage, high-tuning-range capacitive MEMS tuners.

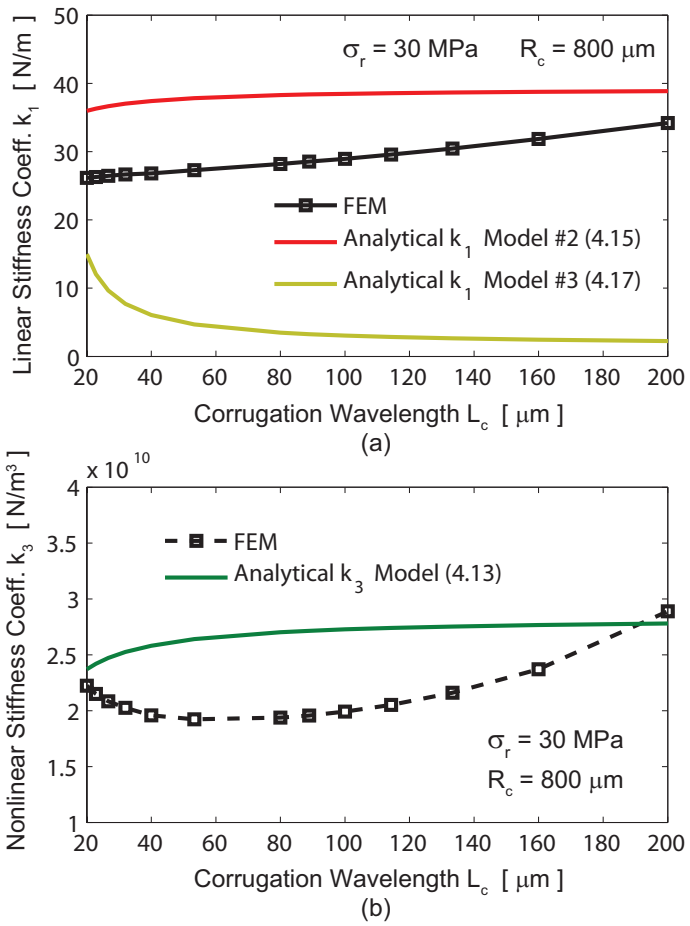

Fig. 4.14. Comparison of FEM and analytical model for (a) linear stiffness coefficient and (b) nonlinear stiffness coefficient versus corrugation wavelength L_c with $\sigma_r = 30$ MPa and $R_c = 800$ μm.

4.4.1 Stiffness versus Corrugation Depth

The dependence of the linear and nonlinear stiffness coefficients on the corrugation depth is shown in Fig. 4.15 for diaphragms with different residual stresses. The linear stiffness can be effectively reduced by increasing the corrugation depth up to an optimal value. Further increase of the corrugation depth will result in large linear stiffness due to the increased bending stiffness of the corrugations in the tangential direction. Large residual stress requires a larger optimal value of H_c to reach the min-

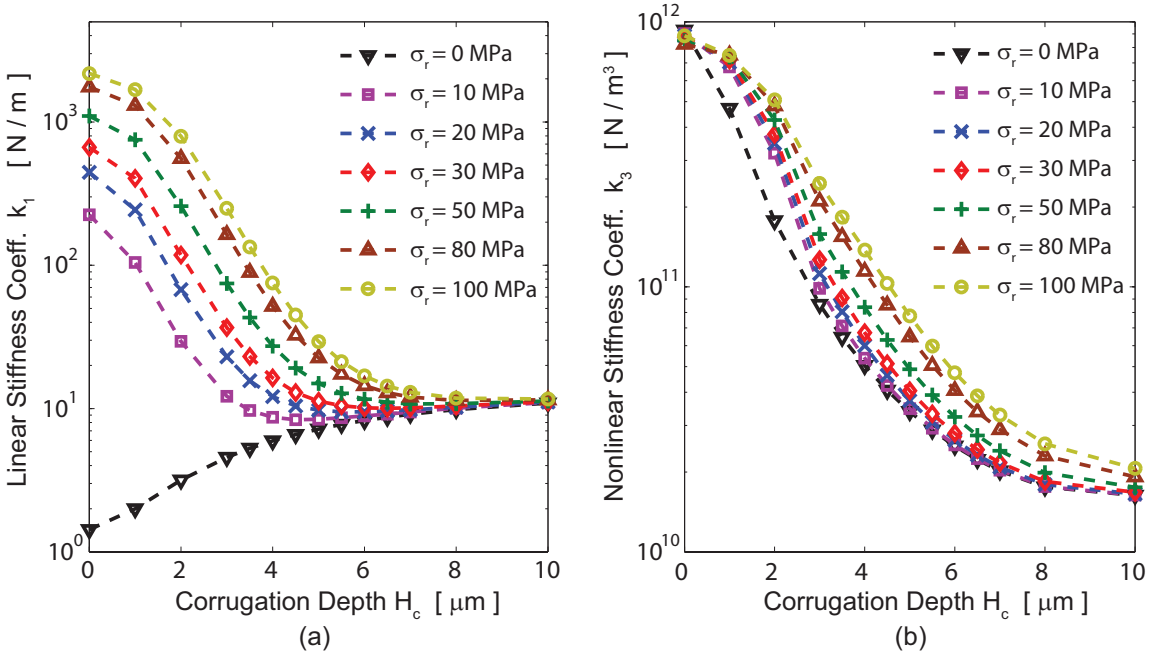

Fig. 4.15. (a) Linear stiffness coefficient and (b) nonlinear stiffness coefficient versus corrugation depth H_c with different residual stress σ_r.

imum linear stiffness, as shown in Fig. 4.16. This optimal value of H_c also decreases with the increase of the corrugation range R_c.

The nonlinear stiffness can be reduced by increasing the corrugation depth H_c. In analytical models, it is assumed that k_3 is independent of the residual stress. However, Fig. 4.15(b) shows that k_3 changes with the residual stress, which might be due to the deformed initial shape of the corrugated diaphragms caused by the residual stress.

4.4.2 Stiffness versus Corrugation Range

The range of corrugation R_c is another important design parameter in determining the stiffness of the diaphragms. The linear and nonlinear stiffnesses are plotted as a function of both R_c and H_c in Fig. 4.17. For a given H_c, there is an optimal value of R_c to minimize the linear stiffness. This indicates that a small corrugation range is

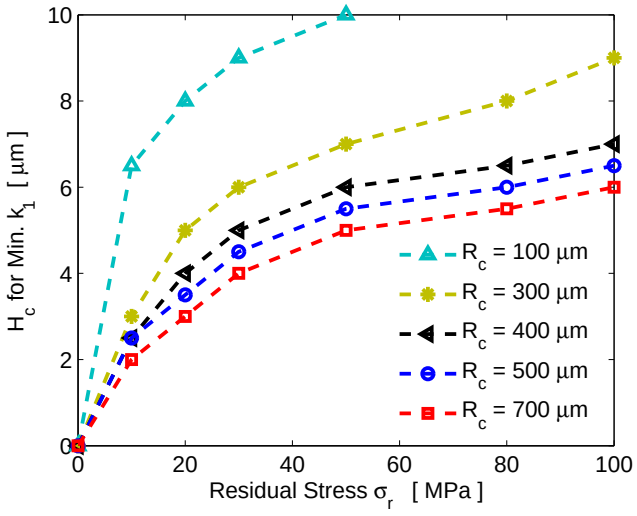

Fig. 4.16. H_c for minimum linear stiffness k_1 versus residual stress with different corrugation range R_c.

not sufficient to release the residual stress, but if the corrugation range is too wide, the bending stiffness of corrugations will be dominant and leads to an increase of k_1. Therefore, we don't want the corrugations to span over the whole diaphragm, but choose a value just sufficient for stress reduction. The nonlinear stiffness k_3 decreases with the increase of R_c for any value of H_c. It is also worth to notice that the corrugation range R_c is less influential than the corrugation depth H_c on the diaphragm stiffness. Therefore, more attention should be paid on choosing the right value of H_c and on controlling the geometry uncertainty during fabrication process.

4.4.3 Stiffness versus Corrugation Wavelength

For a given corrugation range, varying the corrugation wavelength L_c changes the number of corrugations within the fixed range. Fig. 4.18 shows that for shallow corrugations ($H_c = 1$ μm), denser corrugations (*i.e.* smaller L_c) can reduce both k_1 and k_3. However, the bending stiffness of corrugations in the tangential direction increases with deeper corrugations. Therefore, for $H_c \geq 3$ μm, k_1 raises slightly if the

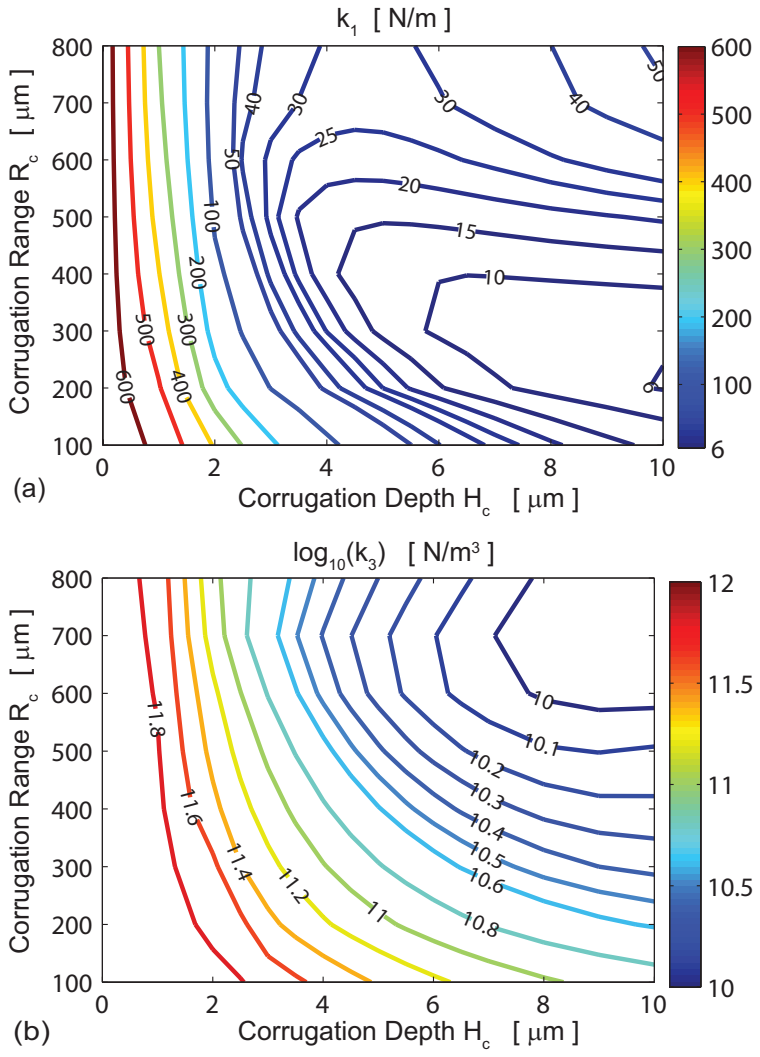

Fig. 4.17. (a)Linear stiffness coefficient and (b) nonlinear stiffness coefficient versus corrugation range R_c and corrugation depth H_c.

corrugations are too dense. The change of stiffness due to the corrugation wavelength is negligible for deeper corrugations $H_c \geq 5$ μm since the corrugation depth is large enough to release residual stress.

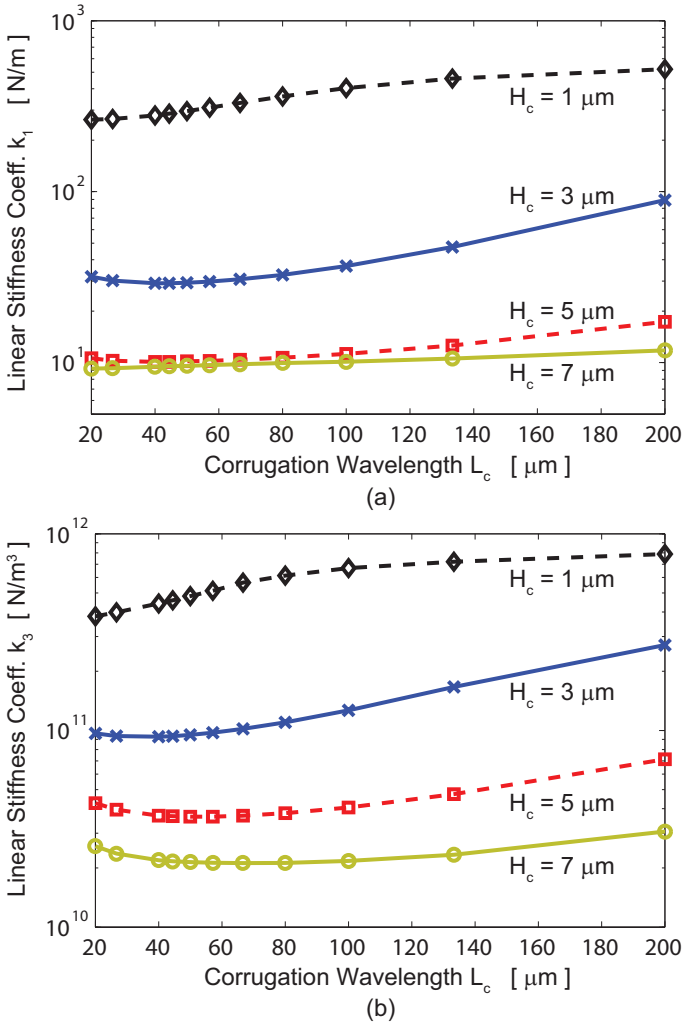

Fig. 4.18. Linear and nonlinear stiffness coefficients versus corrugation wavelength L_c within in a fixed range $R_c = 400$ μm.

4.4.4 Effect of Corrugation Shapes

The sidewall angles of the corrugations alters the shape of the corrugations from a rectangular profile to a trapezoidal one. These corrugation profiles are most practical in micro-fabrication. Fig. 4.19 shows that corrugations with shallow sidewall angles ($\theta < 20°$) are less efficient in relaxing stress. When the corrugations approach a vertical profile, they become harder to bend in the tangential direction, and therefore, k_1 increases. Corrugations with sidewall angles within $20° \leq \theta \leq 50°$ are most efficient

for stress relaxation. Comparing to other geometric parameters, the change of stiffness due to the sidewall angle can be neglected for $\theta \geq 20°$.

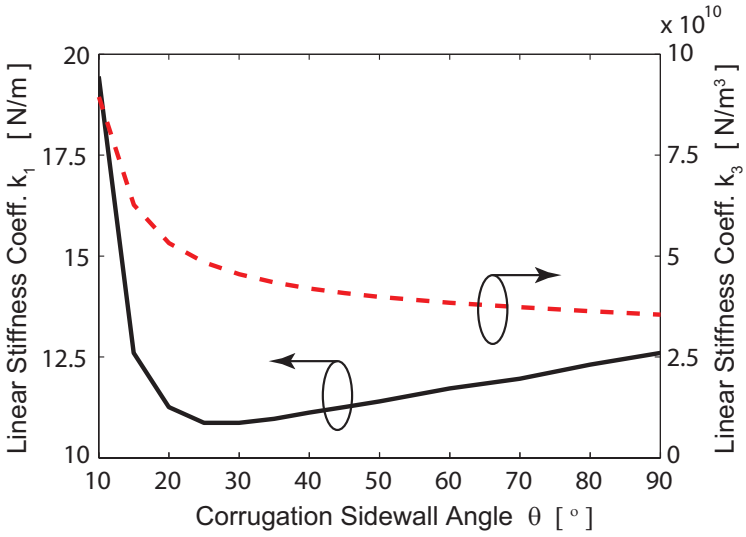

Fig. 4.19. Linear and nonlinear stiffness coefficients versus corrugation sidewall angle θ.

4.5 Tradeoff Between Tuning Range and Pull-in Voltage

By using the linear and nonlinear coefficients extracted from FEM simulations, we can calculate the tuning range and pull-in voltage of the MEMS tuners using (4.22) and (4.23), respectively. The parametric study shows that the corrugation depth H_c and the corrugation range R_c are the two most important geometric parameters in determining the stiffness of corrugated diaphragms. Therefore, the pull-in voltage and tuning range are plotted against H_c and R_c as shown in Fig. 4.20 assuming a residual stress of $\sigma_r = 30$ MPa, and a initial DC gap of $g_0 = 35\mu$m.

It is clear that there is a tradeoff between the pull-in voltage and tuning range. We cannot simultaneously achieve the minimum pull-in voltage and the maximum tuning range. If the minimum pull-in voltage is required, $H_c = 6$ μm and $R_c = 400$ μm, which yields a pull-in voltage of 104.8 V and a normalized tuning range of 0.44. If the

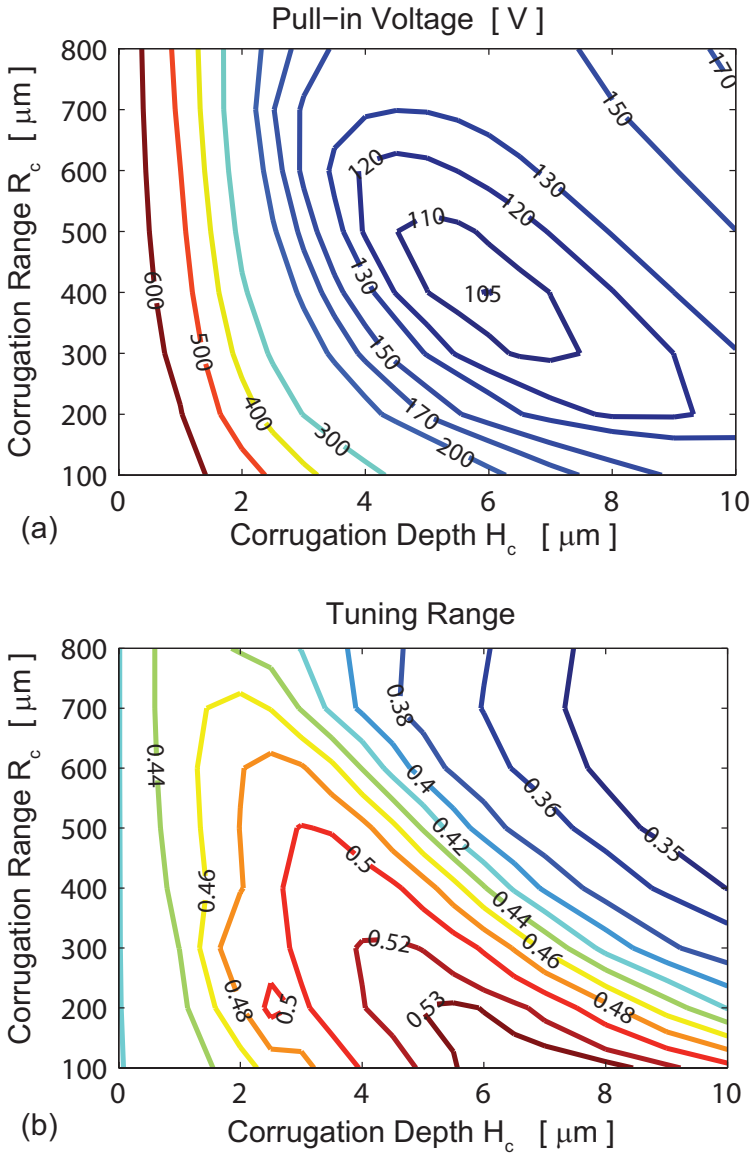

Fig. 4.20. Contour plots of (a) pull-in voltage V_{pi} and (b) tuning range (w_m/g_0) versus corrugation depth H_c and corrugation range R_c for g_0 = 35 μm.

maximum tuning range is needed, $H_c = 7$ μm and $R_c = 100$ μm, which corresponds to a pull-in voltage of 179.1 V and a normalized tuning range of 0.54. According to (4.1), in order to achieve a tuning ratio of $> 3:1$, $w_m > 16$ μm is required, assuming $g_{RF} = 2$ μm. To allow some design margin, we target for a tuning range of $w_m/g_0 \geq 0.5$. From the contour plot in Fig. 4.20, we can find that the lowest pull-in voltage is

110.1 V for $w_m/g_0 = 0.5$ required by choosing $H_c = 5$ μm and $R_c = 400$ μm. This design provides a good compromise between the pull-in voltage and the tuning range. If a flat diaphragm with the same size is used, the pull-in voltage is as high as 677.6 V with a tuning range of 0.41. Therefore, corrugated diaphragms with proper design can efficiently reduce the pull-in voltage while maintaining a high tuning range.

4.6 Conclusions

By introducing corrugated structures into the diaphragm design, the stiffening effects caused by the residual stress can be alleviated and the nonlinear stiffness of the diaphragm under large deflection can be greatly reduced by properly choosing corrugation geometries. With the aid of automated batch mode FEM simulations, a parametric study has been performed and it shows that the corrugation depth and the corrugation range are the most important geometric parameters in corrugated diaphragm design. Using the linear and nonlinear stiffness coefficients extracted from simulations, the tradeoff between the pull-in voltage and the tuning range of the capacitive MEMS tuner has been analyzed. The systematic study of the effects of corrugation geometries on the pull-in voltage and the tuning range provides guidelines for design optimizations.

5. THERMAL-STABLE NONUNIFORM MICRO-CORRUGATED CAPACITIVE MEMS TUNER

5.1 Introduction

Uniform micro-corrugated diaphragms (UMCDs) have been successfully demonstrated as MEMS tuners for evanescent-mode cavity resonators/filters with high tuning range and low tuning voltage [21, 87]. As shown in Fig. 5.1, the micro-corrugated structure effectively relaxes stresses, and thus, reduces the sensitivity of the tuner's stiffness to stress and temperature [21, 87, 92]. However, this stress reduction is accompanied by a stress-induced vertical displacement which becomes prominent under compressive stresses. The fabricated diaphragm has a typical tensile residual stress of a few tens of MPa, and thus exhibits a relatively flat profiles with a center displacement of 1$\sim$2 μm. The residual stress changes over temperature due to the mismatch of the thermal coefficient of expansion (TCE) between the MEMS material and substrate. In most practical cases, the residual stress becomes compressive at high temperatures, and causes a large temperature-induced offset with respect to the diaphragm position at the reference temperature. This offset is > 10 μm for a stress of -30 MPa (Fig. 5.1). Such a significant downward offset may directly alter the frequency response of resonators/filters and greatly reduce the tuning range. Therefore, stable diaphragm position over temperature is a key factor in design robust MEMS tuners, which is critical in achieving temperature-stable resonators/filters. Thermally-stable diaphragms in literature have been designed only for small displacements (< 1 μm) [10, 101, 102], and moreover, the temperature-induced offsets at high temperatures haven't been fully characterized.

In this chapter, we present the first thermally-stable nonuniform micro-corrugated diaphragms (NMCD) designed for a capacitive MEMS tuner with a large tuning

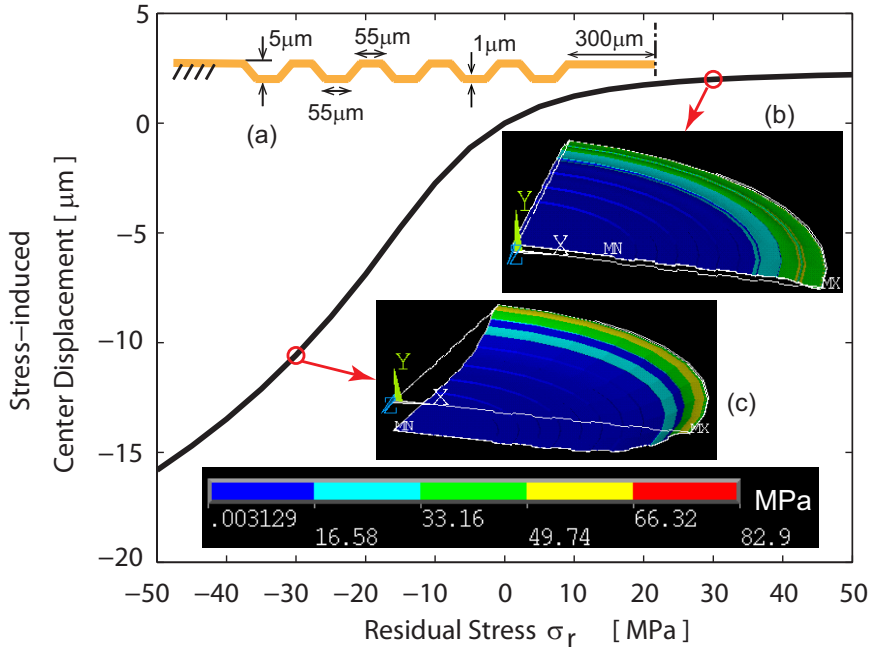

Fig. 5.1. Stress-induced center displacement versus stress for UMCD. The inserts illustrate (a) the dimensions of the UMCD, and the stress distribution for the UMCD under (b) 30 MPa (tensile stress) and (c) −30 MPa (compressive stress). The deformations are shown with ten times magnification.

displacement (> 10 μm). This NMCD has measured center offset < 1.1 μm with a temperature variation of $\Delta T = 100$ °C, which is reduced by 13.5 times compared with the case of UMCDs. Experimental results show that the enhanced thermal stability of NMCD allows its operation in environments with large temperature variations.

5.2 Design of Nonuniform Micro-corrugated Diaphragms

5.2.1 Optimization of Dimensions for Minimizing Temperature Offsets

The microscopy images and the schematic of the symmetric cross-section for the circular NMCD are shown in Fig. 5.2 (a) and (d) [103]. Improved thermal stability is achieved by introducing a deep corrugation closest to the anchor of the diaphragm. This corrugation is optimized to generate an opposite temperature-induced offset to

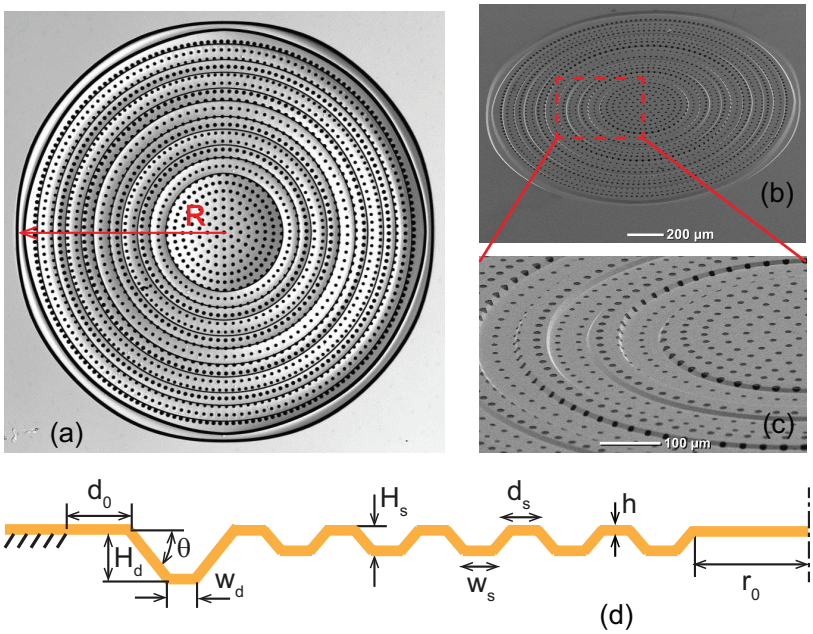

Fig. 5.2. (a) Microscopy image showing the top view, (b) SEM image showing the side view with zoom-in image in (c) showing the corrugations, and (d) schematic view of half of the symmetric cross-section of NMCD.

the one caused by all the other uniform corrugations, and consequently, minimizes the offset of the diaphragm.

This technique is demonstrated by a diaphragm designed for an evanescent-mode resonator operating in K/Ka band. In order to optimize the dimensions of the first deep corrugation, finite-element (FE) simulations of the NMCD are performed in ANSYS [53]. This circular diaphragm is made of a 1-μm-thick gold layer with a radius of $R = 900$ μm, and is anchored at the surface attached to the substrate. There are five shallow uniform corrugations designed for stress reduction with a corrugation depth of $H_s = 5$ μm, and equal corrugation width and corrugation distance of $w_s = d_s = 55$ μm. The corrugation sidewall is inclined with $\alpha = 45$ ° due to the etching process. The simulation model assumes a Young's modulus of $E_0 = 57$ GPa and a Poisson's ratio of $\nu = 0.42$ for gold diaphragm [104].

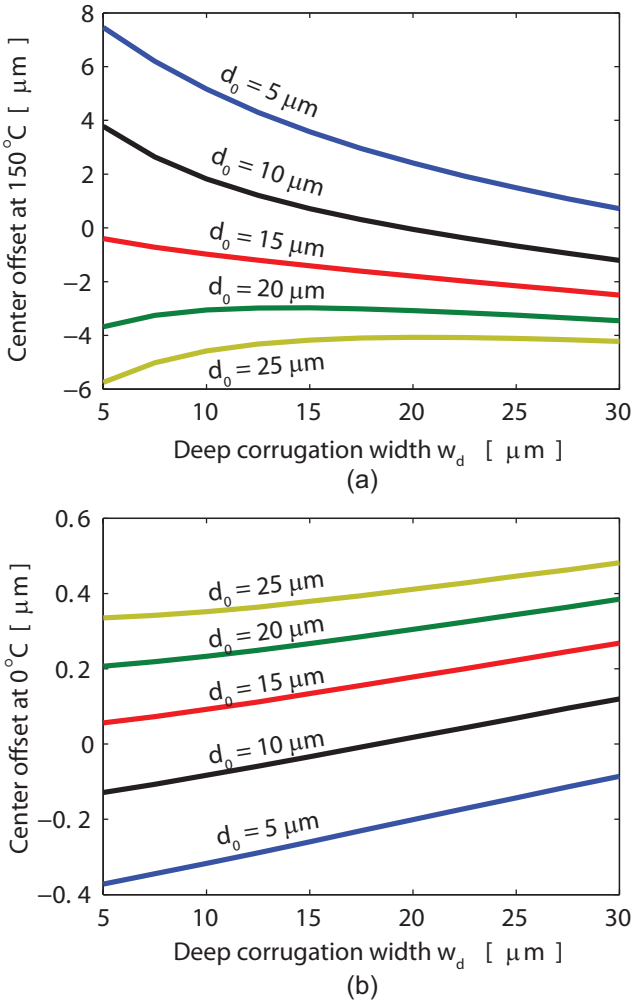

Fig. 5.3. Simulated center offset versus the deep corrugation width (w_d) with different d_0 at (a) 150 °C and (b) 0 °C ($H_d = 15$ μm, $T_0 = 22$ °C).

Simulation results in Fig. 5.3 show that the temperature-induced center offset is a function of both the deep corrugation width (w_d) and the different distance of the large corrugation to the anchor (d0). With a deep corrugation depth $H_d = 15$ μm, there is an optimal value of w_d for a given value of $d_0 \leq 15$ μm for minimizing the offset at both low temperatures (0 °C) and high temperatures (150 °C). This optimal value doesn't exist for $d_0 \geq 20$ μm. This can be explained as follows: the stress of diaphragm is much larger close to the anchor than close to the center (Fig. 5.1(b) and

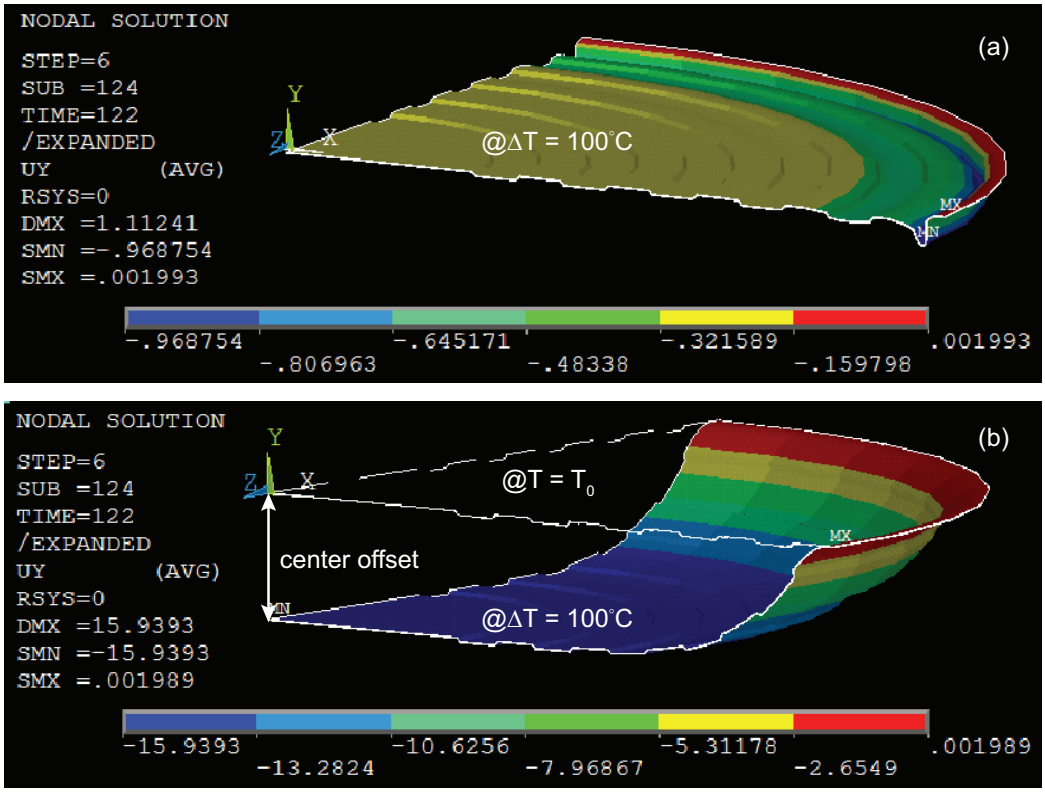

Fig. 5.4. Quarter-symmetry model showing the deformed shapes of (a) NMCD and (b) UMCD at $\Delta T = 100$ °C ($T_0 = 22$ °C). The deformations are magnified by five times.

(c)), and the force and moment due to the stress cause the deformation of the non-planar corrugated structure. Therefore, if the deep corrugation is not placed close enough to the anchor, the deformation from the deep corrugation cannot compensate the offset caused by other uniform corrugations. The distance $d_0 = 15$ μm is chosen for our design to guarantee that the deep corrugation can be fully released during the fabrication, and thus the optimal value for the deep corrugation width is $w_d = 5$ μm. The simulated center offset for this design is < 0.5 μm in the temperature range from 0 °C to 150 °C. The simulated shape of NMCD (Fig. 5.4 (a)) and UMCD (Fig. 5.4 (b)) intuitively show that the NMCD is more stable than the UMCD under a large temperature variation.

5.3 Fabrication Process

The advanced micro-fabrication process for the capacitive MEMS tuner with NMCD is done by ZhengAn Yang. Both NMCDs and UMCDs are fabricated on the same wafer with the same fabrication process shown in Fig. 5.5. Starting with a 300-μm-thick double-side-polished and oxidized silicon wafer (Fig. 5.5(a)), the top oxide layer is first patterned and 5-μm uniform shallow corrugation profile is defined by TMAH etching (Fig. 5.5(b)). After thermal oxidation, a 15-μm deep corrugation is etched using the same technique (Fig. 5.5(c) and (d)). UMCD samples are fabricated on the same wafer without having deep corrugation feature on the second mask. Buffered-oxide-etching removes the top oxide layer and then sputtering a 1-μm-thick gold layer forms the diaphragm with the shape of corrugations transferred from the Si substrate (Fig. 5.5(e)). Releasing holes were patterned on the diaphragm area followed by backside silicon deep reactive ion etching (DRIE) to create a tunnel for bias electrode insert and approach the diaphragm. DRIE was stopped with a thin layer of silicon remained under the gold film (Fig. 5.5(f)). The diaphragm is released using XeF_2 to remove the thin layer of silicon underneath the center of the diaphragm. The diaphragm is fixed to the silicon substrate at its perimeter (Fig. 5.5(g)). During the last step, a backside electrode made of a gold-coated silicon piece with a DRIE etched post is inserted (Fig. 5.5(h)).

5.4 Experimental Results

5.4.1 Measurements of Temperature-Induced Center Offset

The center offsets with respect to the unbiased initial position of the diaphragms at room temperature ($T_0 = 22$ °C) were measured using a confocal microscope for both NMCD and UMCD with a temperature variation up to $\Delta T = 100$ °C. The UMCD and NMCD were placed on a ceramic micro-hotplate at the same time for temperature control. The hotplate was placed under a confocal microscope, and heat-insulation

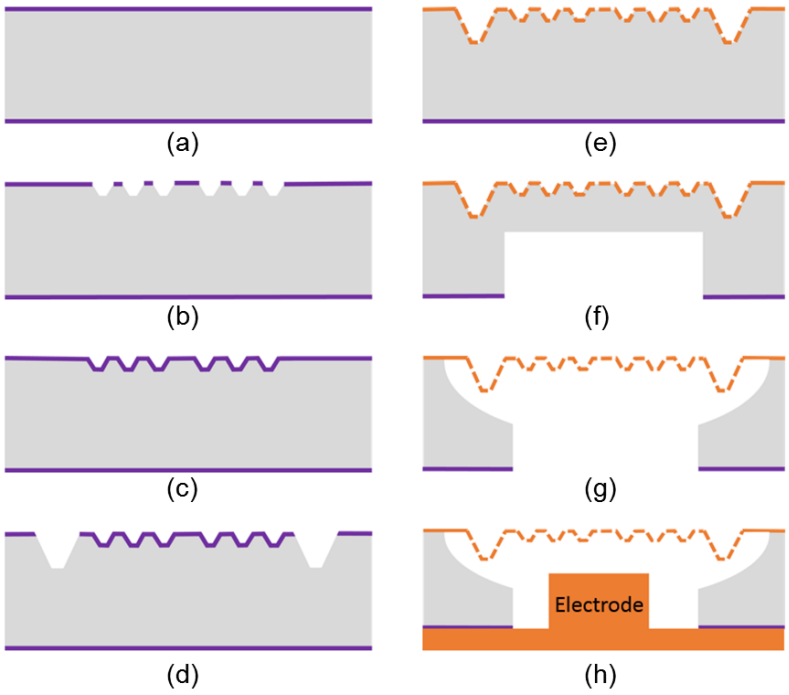

Fig. 5.5. Fabrication flow of the capacitive MEMS tuner with NMCD: (a) silicon wafer with double side SiO_2, (b) TMAH etching, (c) thermal oxidation, (d) TMAH etching, (e) sputter and etch release holes, (f) deep reactive ion etch (DRIE), (g) XeF_2 silicon etch, and (h) insert back side electrode.

pad was placed underneath the hotplate. When temperature is increased gradually from room temperature $T_0 = 22$ °C, the confocal microscope scanned a 3-D image of the device at each temperature, and the height difference between the center of the diaphragm and the gold on the substrate was recorded. The temperature-induced center offset was obtained by calculating the change of the center height with respect to the value at reference temperature $T_0 = 22$ °C. Because of the releasing hole at the center of the diaphragm (Fig. 5.2(a)), measurements cannot be taken exactly at the center but was taken around that releasing hole.

The temperature-induced center offsets were measured from room temperature up to $T = 122$ °C. The results for NMCD and UMCD are compared to ANSYS simulations and are plotted in Fig. 5.6. The measurements show a good agreement to the

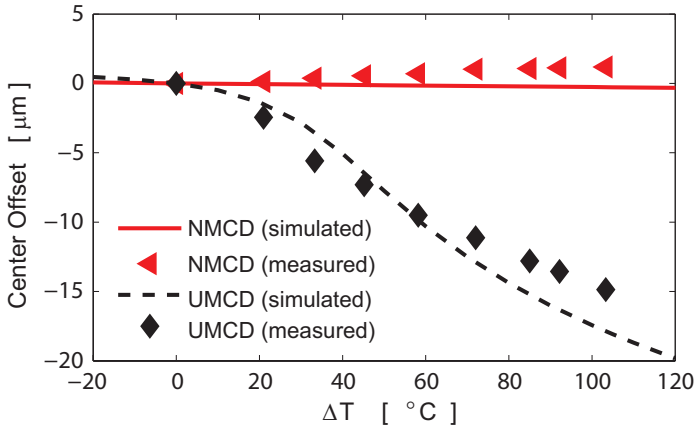

Fig. 5.6. Simulated and measured center offset for NMCD and UMCD ($\Delta T = T - T_0$, with $T_0 = 22$ °C).

simulation results. With a temperature variation of $\Delta T = 100$ °C, the UMCD has a measured downward center offset about 14.9 μm, while the NMCD shows an improvement of 13.5× with an upward center offset around 1.1 μm. Therefore, the deep corrugation with optimized dimensions in NMCD effectively reduces the temperature-induced offset or, in other words, greatly increases the stability of the diaphragm's center position and thus stability of the resonator/filter's performance in an environment with a large temperature variation.

5.4.2 Electrostatic Tuning of the MEMS Tuners

When the MEMS tuner is assembled into an evanescent-mode cavity resonator, the center of the diaphragm is aligned with the loading post in the conductor-walled cavity [21, 87]. The gap between the post and the diaphragm determines the loading capacitance and therefore the resonant frequency. The resonator is calibrated with respect to the initial position of the diaphragm at the reference temperature ($T = T_0$). To achieve frequency tuning, the MEMS tuner is actuated electrostatically by an inserted backside electrode (Fig. 5.5(h)) to change the gap between the loading post and the diaphragm. When an actuation voltage is applied between the diaphragm

and the backside electrode, the consequent electrostatic force deforms the diaphragm away from its initial position towards the backside electrode and away from the post. The increased gap between the post and the diaphragm leads to a decreased loading capacitance, and consequently an increased resonant frequency. Therefore, stabilizing the diaphragm's displacements over temperature variation is the key factor in improving the temperature stability of the resonator.

The electrostatic measurements were conducted by using two probes mounted on the stage of the microscope and adapted to fit into the working distance of the microscope. The same setup used for the measurements of center offset described above was used for temperature control. The displacement versus actuation voltage curves were measured at the reference room temperature T_0 22 °C and at increased temperature with $\Delta T = 45$ °C. As shown in Fig. 5.7(a), the displacement of NMCD changes continuously as the actuation voltage increases, and the voltage required for a 10-μm tuning displacement is 240 V at the room temperature ($T = T_0$). With a temperature increase of $\Delta T = 45$ °C, its center position shifts upwards by 0.3 μm (also shown in Fig. 5.6). Since this small temperature-induced offset is upward, it can be compensated by a small bias voltage and therefore the NMCD can still be tuned over the entire desired tuning range. At the increased temperature, the NMCD requires an actuation voltage of 215 V to reach a 10-μm tuning displacement, which changes by 10.4%. The decrease of the required voltage is due to the reduced diaphragm stiffness. As temperature increases, the residual stress in the diaphragm becomes more compressive which leads to a reduced diaphragm stiffness.

The MEMS tuner with UMCD is also measured for comparison as shown in Fig. 5.7 (b). At $\Delta T = 45$ °C, the UMCD has a downward center offset of 7.5 μm. Such a large downward offset cannot be compensated by the bias voltage and thus greatly reduces the tuning range by 75% compared with the desired range. If the temperature is further increased, the center offset will make the diaphragm deforms out of the desired range, and thus lead to the resonator's failure of operation in the desired frequency range. In addition, the required voltage to tune the UMCD to a 10-μm

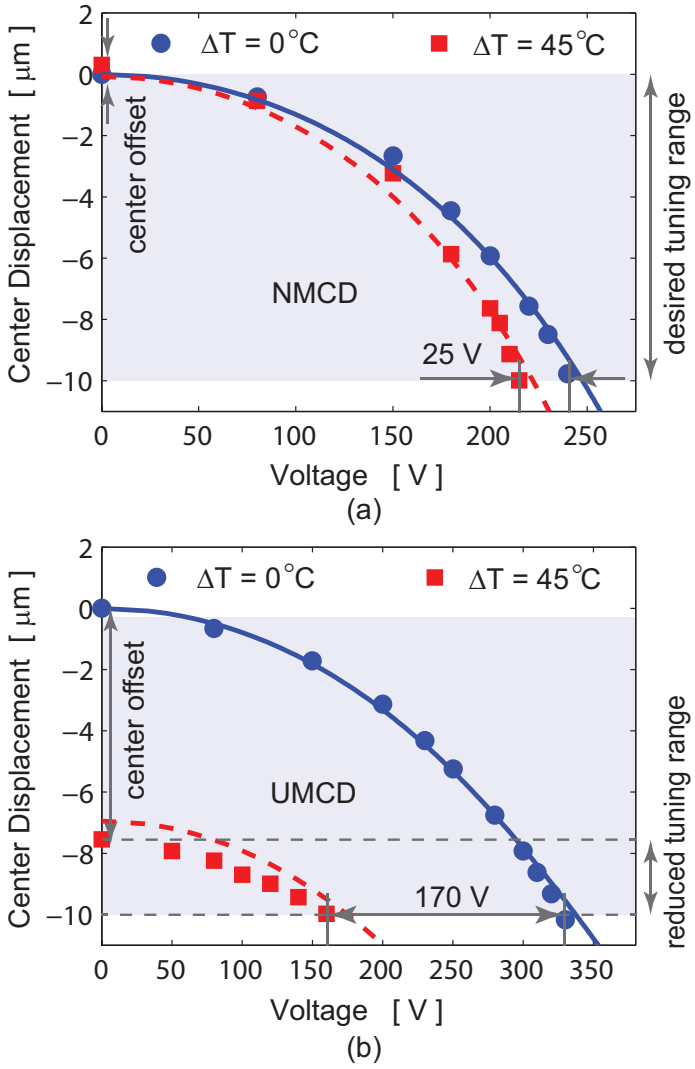

Fig. 5.7. Measured and calculated tuning displacement versus actuation voltage curves for capacitive tuners with (a) NMCD, and (b) UMCD ($\Delta T = T - T_0$, with $T_0 = 22$ °C). The blue solid lines and the red dashed lines are calculated results by using (4.19) for the case of $\Delta T = 0$°C and $\Delta T = 45$°C, respectively.

displacement (with respect to the initial position at $T = T_0$) changes by 51.5% from 330 V (at $T = T_0$) to 160 V (at $\Delta T = 45$ °C).

The measured tuning displacement versus actuation voltage curves are compared to calculated results as shown in Fig. 5.7. With the stiffness coefficients k_1 and k_3 and the initial offset w_0 obtained by ANSYS simulations, the displacement-voltage

relationship can be calculated using (4.19). The experimental results show a good agreement with the calculated results. Therefore, it confirms that the parallel-plate model described by (4.19) provides a good approximation of the displacement-voltage relationship for the capacitive MEMS tuner.

5.5 Conclusions

In this chapter we propose a thermally-stable capacitive MEMS tuner with a large tuning displacement for evanescent-mode cavity resonators/filters. Through the optimization of the proposed NMCD by FE simulations, the temperature stability of the tuner can be great improved. This design of MEMS tuner with NMCD is experimentally validated. The temperature-induced center offsets of the diaphragms are measured at a series of high temperatures. With $\Delta T = 100$ °C, the center offset of the NMCD is 1.1 μm which is reduced by 13.5 times compared with that of a UMCD. The measured electrostatic tuning of the capacitive MEMS tuners demonstrates that the thermally-stable NMCD allows the diaphragm to be continuously tunable in its full desired range with a reduced variation of actuation voltage over a wide temperature range.

6. SUMMARY

6.1 Dissertation Summary

Non-idealities in RF MEMS tuners cause performance degradation or even device failure. To design RF MEMS tuners with high performance and reliability, this dissertation presents the modeling and characterization of non-ideal effects of non-perfect anchors, in-plane residual stress and temperature sensitivity. With the awareness of the unavoidable non-ideal effects arising from the fabrication uncertainties and environmental variations, this dissertation further present the design optimization to alleviate residual stress issues and temperature sensitivity of RF MEMS diaphragm tuners.

The non-ideal effects of inclined supports in fixed-fixed MEMS beams arising from practical fabrication have been investigated by an equation-based nonlinear model. The calculated beam displacements agree with FEM models to within 1.1% in both the linear and nonlinear regimes. Furthermore, experimentally-obtained displacements of six fabricated beams with inclined supports agree to within 5.2% with the presented model. With this comprehensive model developed, the wafer-scale extraction technique for residual stress technique based on electrostatically actuated fixed-fixed beam structures has been demonstrated. The ~ 90 beams on a 4-inch quarter wafer piece have been characterized and the extracted residual stress values vary between -12.8 MPa and 13.6 MPa. The residual stresses for these beams follow a nearly normal distribution with a mean value of -1.7 MPa and a standard deviation of 5.9 MPa which represents the variability of the residual stresses across the wafer. Detailed uncertainty analysis reveals that inaccurate modeling of the non-ideal effects, especially the non-flat profile and the inclined supports, will result in significant errors in the extracted residual stress. To alleviate the residual stress ef-

fects, design optimization has been conducted for a MEMS diaphragm tuner used in cavity resonators/filters. The tradeoff between pull-in voltage and tuning range of the capacitive RF MEMS tuner has been analyzed through a parametric study. The systematic study of the effects of corrugation geometries on the pull-in voltage and the tuning range provides guidelines for design optimizations. Furthermore, a thermally-stable capacitive RF MEMS tuner is proposed based on a circular NMCD suitable for resonators/filters which require a large tuning displacement (> 10 μm). The measured temperature-induced center offset of the NMCD is reduced by 13.5 $\times$ with a temperature variation of ΔT = 100°C compared with the case of UMCDs, which allows the NMCD to be continuously tunable in its full desired range. Moreover, the change of actuation voltage required for maintaining a 10-μm diaphragm deflection is reduced from 51.5% to 10.4% with ΔT = 45°C.

6.2 Contributions

The contributions of this dissertation are listed as follows:

- Chapter 2: The presence of the inclined supports and the resulting non-ideal effects have been brought into attention. We have modeled the mechanical and electromechanical effects of inclined supports for the first time. This proposed model calculates and validates the effects of residual stress and loading on the post-release beam behavior including their nonlinear large-displacement characteristics. The non-flat beam profiles caused by residual stress and/or a non-flat sacrificial layer profile has also be accounted for in this model.

- Chapter 3: A wafer-scale extraction technique for residual stress based on electrostatically actuated fixed-fixed beam structures has been demonstrated and the wafer-scale extraction results have been reported for the first time. The statistical distribution and spatial distribution of the residual stress on a quarter-wafer piece have been presented. Detailed uncertainty analysis reveals that inaccurate modeling of the non-ideal effects, especially the non-flat profile and

the inclined supports, will result in significant errors in the extracted residual stress.

- Chapter 4: The design optimization for RF MEMS tuners based on corrugated diaphragms has been conducted through systematic parametric study and tradeoff analysis. It has been shown that the corrugation depth and the corrugation range are the most important geometric parameters in corrugated diaphragm design. The design tradeoff between the tuning voltage and tuning range needs to be taken into consideration during design process.

- Chapter 5: The first thermally-stable capacitive MEMS tuner based on a circular NMCD has been demonstrated. This MEMS tuner is suitable for application requiring a large tuning displacement (> 10 μm), such as the evanescent-mode resonators/filters. The enhanced temperature stability allows the RF MEMS tuner to be continuously tunable in the full desired range with a reduced variation of required actuation voltage.

6.3 Future Work

6.3.1 Full Characterization of Thermally-Stable Cavity Filters Based on RF MEMS Tuner

The temperature-stability of the diaphragm RF MEMS tuner presented in Chapter 5 has been experimentally validated. As an RF MEMS tuner is used in high-Q resonators/filters, a full characterization is necessary. Since the RF MEMS tuner is used to tune the capacitance between the diaphragm and the loading post in the cavity, instead of the capacitance between the diaphragm and the biasing electrodes, the RF characterization of the tuner needs to be conducted by assembling the tuner with the cavity. The insertion loss [105] and intermodulation [106] need to be characterized.

With the temperature-stable diaphragm RF MEMS tuner demonstrated with continuous tunability over a wide temperature range, it can be employed to design cavity resonators/filters with enhanced temperature stability. The frequency response of the tunable resonators/filters can be measured when temperature varies to validate the design. Special attention should be paid to the design of measurement setup to minimize the frequency shift caused by the temperature sensitivity of the test setup other than that of the diaphragm itself.

6.3.2 Uncertainty Quantification of RF MEMS Tuners

In Chapter 4, the performance of the RF MEMS tuners has been analyzed with respective to the variations of each geometric parameters separately. This study allows the determination of the important design parameters. To further evaluate the uncertainty of the tuning voltage and tuning range of the RF MEMS tuners under a given variability in geometric parameters and material properties, it is necessary to perform uncertainty quantification analysis.

Since stochastic simulations are required for uncertainty quantification analysis, it is essential to develop computation-efficient modeling of the tuner devices. An closed-form analytical model with sufficient accuracy is ideal. One solution is to modify the existing analytical model by adding fitted coefficients to increase its accuracy. On the other hand, more efficient sampling algorithm should be chosen to reduce the number of simulations needed for obtaining the output probability density functions (PDFs).

6.3.3 Automated Wafer-Scale Test Methodology for RF MEMS Tuners

The wafer-scale evaluation of geometric parameters and material properties is desired to efficiently characterize the fabrication variabilities. With experimentally-obtained data, device simulations can be done with process corners to ensure adequate design margin. In Chapter 3, a methodology for residual stress extraction technique has been presented which is suitable for automated wafer-scale applications. Other

material properties such as Young's modulus may also vary from batch-to-batch, wafer-to-wafer, or even within a wafer piece. Therefore, automated wafer-scale test methodologies for geometric parameters and material properties need to be developed.

REFERENCES

REFERENCES

[1] "Mobile communications overview: An evolving wireless landscape." [Online]. Available: http://wispry.com/mobile-communications-overview.php

[2] "Teardown.com analysis: The Apple iPhone 6 & 6 plus." [Online]. Available: http://www.techinsights.com/teardown.com/apple-iphone-6/

[3] H. Tilmans, W. De Raedt, and E. Beyne, "MEMS for wireless communications: from RF-MEMS components to RF-MEMS-SiP," *Journal of Micromechanics and Microengineering*, vol. 13, no. 4, p. S139, 2003.

[4] E. Brown, "RF-MEMS switches for reconfigurable integrated circuits," *IEEE Transactions on Microwave Theory and Techniques*, vol. 46, no. 11, pp. 1868–1880, 1998.

[5] G. Rebeiz, K. Entesari, I. Reines, S. Park, M. El-Tanani, A. Grichener, and A. Brown, "Tuning in to RF MEMS," *Microwave Magazine, IEEE*, vol. 10, no. 6, pp. 55–72, 2009.

[6] "Smartphone using discrete switches or antenna switch modules." [Online]. Available: http://www.skyworksinc.com/downloads/block_diagrams/smartphone.pdf

[7] G. M. Rebeiz, *RF MEMS: Theory, Design, and Technology*, 1st ed. New York: Wiley-Interscience, 2003.

[8] C. Goldsmith, J. Ehmke, A. Malczewski, B. Pillans, S. Eshelman, Z. Yao, J. Brank, and M. Eberly, "Lifetime characterization of capacitive RF MEMS switches," in *IEEE MTT-S International Microwave Symposium Digest*, vol. 1, May 2001, pp. 227–230 vol.1.

[9] S. Majumder, J. Lampen, R. Morrison, and J. Maciel, "A packaged, high-lifetime ohmic MEMS RF switch," in *IEEE MTT-S International Microwave Symposium Digest*, vol. 3, June 2003, pp. 1935–1938 vol.3.

[10] I. Reines, B. Pillans, and G. M. Rebeiz, "Thin-film aluminum RF MEMS switched capacitors with stress tolerance and temperature stability," *Journal of Microelectromechanical Systems*, vol. 20, no. 1, pp. 193–203, Feb. 2011.

[11] I. Borwick, R.L., P. Stupar, J. DeNatale, R. Anderson, and R. Erlandson, "Variable MEMS capacitors implemented into RF filter systems," *IEEE Transactions on Microwave Theory and Techniques*, vol. 51, no. 1, pp. 315–319, Jan 2003.

[12] H.-T. Kim, S. Jung, K. Kang, J.-H. Park, Y.-K. Kim, and Y. Kwon, "Low-loss analog and digital micromachined impedance tuners at the ka-band," *IEEE Transactions on Microwave Theory and Techniques*, vol. 49, no. 12, pp. 2394 –2400, Dec. 2001.

[13] J. Papapolymerou, K. Lange, C. Goldsmith, A. Malczewski, and J. Kleber, "Reconfigurable double-stub tuners using MEMS switches for intelligent RF front-ends," *IEEE Transactions on Microwave Theory and Techniques*, vol. 51, no. 1, pp. 271 – 278, Jan. 2003.

[14] D. Peroulis and L. Katehi, "Electrostatically-tunable analog RF MEMS varactors with measured capacitance range of 300%," in *IEEE MTT-S International Microwave Symposium Digest*, vol. 3, June 2003, pp. 1793–1796 vol.3.

[15] K. Entesari and G. Rebeiz, "A 12-18GHz three-pole RF MEMS tunable filter," *IEEE Transactions on Microwave Theory and Techniques*, vol. 53, no. 8, pp. 2566–2571, 2005.

[16] A. Pothier, J.-C. Orlianges, G. Zheng, C. Champeaux, A. Catherinot, D. Cros, P. Blondy, and J. Papapolymerou, "Low-loss 2-bit tunable bandpass filters using MEMS DC contact switches," *IEEE Transactions on Microwave Theory and Techniques*, vol. 53, no. 1, pp. 354–360, Jan. 2005.

[17] K. Entesari and G. Rebeiz, "A differential 4-bit 6.5-10ghz RF MEMS tunable filter," *IEEE Transactions on Microwave Theory and Techniques*, vol. 53, no. 3, pp. 1103–1110, Mar. 2005.

[18] X. Liu, L. Katehi, W. Chappell, and D. Peroulis, "High-Q tunable microwave cavity resonators and filters using SOI-based RF MEMS tuners," *Journal of Microelectromechanical Systems*, vol. 19, no. 4, pp. 774–784, Aug 2010.

[19] M. Arif and D. Peroulis, "All-silicon technology for high-Q evanescent mode cavity tunable resonators and filters," *Journal of Microelectromechanical Systems*, vol. 23, no. 3, pp. 727–739, June 2014.

[20] D. Peroulis, E. Naglich, M. Sinani, and M. Hickle, "Tuned to resonance: Transfer-function-adaptive filters in evanescent-mode cavity-resonator technology," *IEEE Microwave Magazine*, vol. 15, no. 5, pp. 55–69, July 2014.

[21] Z. Yang and D. Peroulis, "A 23-35 GHz MEMS tunable all-silicon cavity filter with stability characterization up to 140 million cycles," in *IEEE MTT-S International Microwave Symposium (IMS)*, June 2014, pp. 1–4.

[22] R. Stefanini, J. Martinez, M. Chatras, A. Pothier, V. Boria, and P. Blondy, "Ku band high-Q tunable surface-mounted cavity resonator using RF MEMS varactors," *IEEE Microwave and Wireless Components Letters*, vol. 21, no. 5, pp. 237–239, May 2011.

[23] J. Small, M. Arif, A. Fruehling, and D. Peroulis, "A tunable miniaturized RF MEMS resonator with simultaneous high-q (500-735) and fast response speed ($< 10 - 60\mu$s)," *Journal of Microelectromechanical Systems*, vol. 22, no. 2, pp. 395–405, Apr. 2013.

[24] P. Osterberg and S. Senturia, "M-TEST: A test chip for MEMS material property measurement using electrostatically actuated test structures," *Journal of Microelectromechanical Systems*, vol. 6, no. 2, pp. 107–118, Jun. 1997.

[25] W. Van Spengen, R. Puers, R. Mertens, and I. De Wolf, "A comprehensive model to predict the charging and reliability of capacitive RF MEMS switches," *Journal of Micromechanics and Microengineering*, vol. 14, no. 4, p. 514, 2004.

[26] J. DeNatale and R. Mihailovich, "RF MEMS reliability," in *12th International Conference on Transducers, Solid-State Sensors, Actuators and Microsystems*, vol. 2, June 2003, pp. 943–946.

[27] H.-H. Hsu, "Characterization and modeling of creep in RF-MEMS tunable components and circuits," Ph.D. dissertation, Purdue University, West Lafyatte, IN, May 2011.

[28] D. Peroulis, "RF MEMS devices for multifunctional integrated circuits and antennas," Ph.D. dissertation, University of Michigan, Ann Arbor, 2003.

[29] E. Brown, "RF-MEMS switches for reconfigurable integrated circuits," *IEEE Trans. Microw. Theory Tech.*, vol. 46, pp. 1868–1880, Nov. 1998.

[30] C. Goldsmith, Z. Yao, S. Eshelman, and D. Denniston, "Performance of low-loss RF MEMS capacitive switches," *Microwave and Guided Wave Letters, IEEE*, vol. 8, no. 8, pp. 269–271, Aug. 1998.

[31] F. Bannon, J. Clark, and C.-C. Nguyen, "High-Q HF microelectromechanical filters," *IEEE J. Solid-State Circuits*, vol. 35, no. 4, pp. 512–526, Apr. 2000.

[32] J. Lopez, J. Verd, A. Uranga, J. Giner, G. Murillo, F. Torres, G. Abadal, and N. Barniol, "A CMOS MEMS RF-tunable bandpass filter based on two high-Q 22-MHz polysilicon clamped-clamped beam resonators," *IEEE Electron Device Letters*, vol. 30, no. 7, pp. 718–720, July 2009.

[33] F. Fachin, S. A. Nikles, J. Dugundji, and B. L. Wardle, "Analytical extraction of residual stresses and gradients in MEMS structures with application to CMOS-layered materials," *J. Micromech. Microeng.*, vol. 21, no. 9, p. 095017, Sep. 2011.

[34] M. Baker, M. de Boer, N. Smith, L. Warne, and M. Sinclair, "Integrated measurement-modeling approaches for evaluating residual stress using micromachined fixed-fixed beams," *Journal of Microelectromechanical Systems*, vol. 11, no. 6, pp. 743 – 753, Dec. 2002.

[35] E. Chan, K. Garikipati, and R. Dutton, "Characterization of contact electromechanics through capacitance-voltage measurements and simulations," *Journal of Microelectromechanical Systems*, vol. 8, no. 2, pp. 208–217, Jun. 1999.

[36] Z. Fan, J. Engel, J. Chen, and C. Liu, "Parylene surface-micromachined membranes for sensor applications," *Journal of Microelectromechanical Systems*, vol. 13, no. 3, pp. 484–490, June 2004.

[37] S. Soulimane, F. Casset, P.-L. Charvet, C. Maeder, and M. Aid, "Planarization of photoresist sacrificial layer for MEMS fabrication," *Microelectronic Engineering*, vol. 84, no. 5-8, pp. 1398 – 1400, 2007, proceedings of the 32nd International Conference on Micro- and Nano-Engineering.

[38] S. C. Saha, H. Sagbergb, E. Poppe, G. U. Jensen, T. A. Fjeldly, and T. Sthera, "Tuning of resist slope with hard-baking parameters and release methods of extra hard photoresist for RF MEMS switches," *Sensors and Actuators A: Physical*, vol. 143, no. 2, pp. 452 – 461, 2008.

[39] C. Villeneuve, P. Pons, V. Puyal, and R. Plana, "Planarization optimization of RF-MEMS switches with a gold membrane," *Journal of Micromechanics and Microengineering*, vol. 20, no. 6, p. 064013, 2010.

[40] C. O'Mahony, M. Hill, R. Duane, and A. Mathewson, "Analysis of electromechanical boundary effects on the pull-in of micromachined fixed fixed beams," *J. Micromech. Microeng.*, vol. 13, pp. S75–S80, Jul. 2003.

[41] J.-Y. Gill, L. Ngo, P. Nelson, and C.-J. Kim, "Elimination of extra spring effect at the step-up anchor of surface-micromachined structure," *Journal of Microelectromechanical Systems*, vol. 7, no. 1, pp. 114–121, Mar. 1998.

[42] R. Mullen, M. Mehregany, M. Omar, and W. Ko, "Theoretical modeling of boundary conditions in microfabricated beams," in *IEEE Micro Electro Mechanical Systems, MEMS '91, Proceedings. An Investigation of Micro Structures, Sensors, Actuators, Machines and Robots.*, 30 Jan.-2 Feb. 1991, pp. 154–159.

[43] Q. Meng, M. Mehregany, and R. Mullen, "Theoretical modeling of microfabricated beams with elastically restrained supports," *Journal of Microelectromechanical Systems*, vol. 2, no. 3, pp. 128–137, Sep. 1993.

[44] B. D. Jensen, F. Bitsie, and M. P. de Boer, "Interferometric measurement for improved understanding of boundary effects in micromachined beams," in *Society of Photo-Optical Instrumentation Engineers (SPIE) Conference Series*, vol. 3875, Sep. 1999, pp. 61–72.

[45] Y.-C. Hu, P.-Z. Chang, and W.-C. Chuang, "An approximate analytical solution to the pull-in voltage of a micro bridge with an elastic boundary," *J. Micromech. Microeng.*, vol. 17, no. 9, pp. 1870–1876, Sep. 2007.

[46] M. Kobrinsky, E. Deutsch, and S. Senturia, "Effect of support compliance and residual stress on the shape of doubly supported surface-micromachined beams," *Journal of Microelectromechanical Systems*, vol. 9, no. 3, pp. 361 –369, Sep. 2000.

[47] E. Chan, K. Garikipati, and R. Dutton, "Characterization of contact electromechanics through capacitance-voltage measurements and simulations," *Journal of Microelectromechanical Systems*, vol. 8, no. 2, pp. 208–217, Jun. 1999.

[48] R. C. Tung, A. Garg, A. Kovacs, D. Peroulis, and A. Raman, "Estimating residual stress, curvature and boundary compliance of doubly clamped MEMS from their vibration response," *Journal of Micromechanics and Microengineering*, vol. 23, no. 4, p. 045009, Apr. 2013.

[49] M. G. Snow and A. K. Bajaj, "Comprehensive reduced-order models of electrostatically actuated MEMS switches and their dynamics including impact and bounce," *ASME Conference Proceedings*, vol. 2010, no. 44120, pp. 579–588, 2010.

[50] M. G. Snow, "Comprehensive modeling of electrostatically actuated MEMS beams including uncertainty quantification," Master's thesis, Purdue Univeristy, West Lafayette, IN, 2010.

[51] S. Alkharabsheh and M. Younis, "Dynamics of MEMS arches of flexible supports," *Journal of Microelectromechanical Systems*, vol. 22, no. 1, pp. 216–224, Feb. 2013.

[52] J. Zeng, A. Kovacs, A. Garg, A. K. Bajaj, and D. Peroulis, "An equation-based nonlinear model for inclined supports in non-flat MEMS fixed-fixed beams," June 2014, under review.

[53] "ANSYSAcademic Research, Release 14.5, help system, ANSYS mechanical APDL structural analysis, ANSYS, inc," 2014. [Online]. Available: http://ansys.com

[54] C. R. Patrick, "A quantitative study of the microstructure and crystallographic fiber texture in nickel electrodeposits used in radio-frequency MEMS switches, including a new transmission electron microscopy (TEM) technique for polycrystalline films," Ph.D. dissertation, Purdue University, West Lafayette, IN, 2011.

[55] *MEMS Design and Analysis Tutorials, vol.1*, Coventor, Inc., Cary, NC, 2010.

[56] H.-H. Hsu and D. Peroulis, "An experimental investigation on viscoelastic behavior in tunable planar RF-MEMS resonators," in *IEEE MTT-S International Microwave Symposium Digest (MTT)*. IEEE, May 2010, pp. 1150–1153.

[57] "Olympus confocal laser scanning microscope LEXT OLS3100," 2007. [Online]. Available: http://industrial-microscope.olympus-global.com/en/ga/product/ols3100/sp.cfm

[58] R. Artigas, *Imaging Confocal Microscopy*. Springer Berlin Heidelberg, 2011, ch. 11, pp. 237–286.

[59] V. Srikar and S. Spearing, "A critical review of microscale mechanical testing methods used in the design of microelectromechanical systems," *Experimental Mechanics*, vol. 43, pp. 238–247, Feb. 2003.

[60] R. E. Strawser, K. D. Leedy, R. Cortez, J. L. Ebel, S. R. Dooley, C. F. H. Abell, and V. M. Bright, "Influence of metal stress on RF MEMS capacitive switches," *Sensor and Actuators A: Physical*, vol. 134, no. 2, pp. 600 – 605, Mar. 2007.

[61] M. K. Small and W. Nix, "Analysis of the accuracy of the bulge test in determining the mechanical properties of thin films," *Journal of Materials Research*, vol. 7, pp. 1553–1563, Jun. 1992.

[62] V. Ziebart, O. Paul, U. Munch, J. Schwizer, and H. Baltes, "Mechanical properties of thin films from the load deflection of long clamped plates," *Journal of Microelectromechanical Systems*, vol. 7, no. 3, pp. 320–328, Sept. 1998.

[63] T. Harder, T.-J. Yao, Q. He, C.-Y. Shih, and Y.-C. Tai, "Residual stress in thin-film parylene-c," in *The Fifteenth IEEE International Conference on Micro Electro Mechanical Systems*, 2002, pp. 435–438.

[64] J. Mitchell, C. Zorman, T. Kicher, S. Roy, and M. Mehregany, "Examination of bulge test for determining residual stress, young's modulus, and poisson's ratio of 3C-SiC thin films," *Journal of Aerospace Engineering*, vol. 16, no. 2, pp. 46–54, 2003.

[65] W. Nix, "Mechanical properties of thin films," *Metallurgical and Materials Transactions A*, vol. 20, pp. 2217–2245, Nov. 1989.

[66] E. G. Herbert, W. C. Oliver, M. P. de Boer, and G. M. Pharr, "Measuring the elastic modulus and residual stress of freestanding thin films using nanoindentation techniques," *Journal of Materials Research*, vol. 24, pp. 2974–2985, Sept. 2009.

[67] H. D. Espinosa, B. C. Prorok, and M. Fischer, "A methodology for determining mechanical properties of freestanding thin films and MEMS materials," *Journal of the Mechanics and Physics of Solids*, vol. 51, no. 1, pp. 47 – 67, Jan. 2003.

[68] Y. Zhou, C.-S. Yang, J.-A. Chen, G.-F. Ding, W. Ding, L. Wang, M.-J. Wang, Y.-M. Zhang, and T.-H. Zhang, "Measurement of young's modulus and residual stress of copper film electroplated on silicon wafer," *Thin Solid Films*, vol. 460, no. 1-2, pp. 175–180, Jul. 2004.

[69] M. Haque and M. Saif, "A review of MEMS-based microscale and nanoscale tensile and bending testing," *Experimental Mechanics*, vol. 43, no. 3, pp. 248–255, 2003.

[70] H. Espinosa, Y. Zhu, M. Fischer, and J. Hutchinson, "An experimental/computational approach to identify moduli and residual stress in MEMS radio-frequency switches," *Experimental Mechanics*, vol. 43, pp. 309–316, Sept. 2003.

[71] S. Chen, T. Baughn, Z. Yao, and C. Goldsmith, "A new in situ residual stress measurement method for a MEMS thin fixed-fixed beam structure," *Journal of Microelectromechanical Systems*, vol. 11, no. 4, pp. 309 – 316, Aug. 2002.

[72] P. Osterberg and S. Senturia, "M-TEST: A test chip for MEMS material property measurement using electrostatically actuated test structures," *Journal of Microelectromechanical Systems*, vol. 6, no. 2, pp. 107 –118, Jun. 1997.

[73] M. P. de Boer, F. W. DelRio, and M. S. Baker, "On-chip test structure suite for free-standing metal film mechanical property testing, part I - analysis," *Acta Materialia*, vol. 56, no. 14, pp. 3344 – 3352, Aug. 2008.

[74] M. P. de Boer, A. D. Corwin, P. G. Kotula, M. S. Baker, J. R. Michael, G. Subhash, and M. J. Shaw, "On-chip laboratory suite for testing of freestanding metal film mechanical properties, part II - experiments," *Acta Materialia*, vol. 56, no. 14, pp. 3313–3326, Aug. 2008.

[75] C. O'Mahony, M. Hill, M. Brunet, R. Duane, and A. Mathewson, "Characterization of micromechanical structures using white-light interferometry," *Measurement Science and Technology*, vol. 14, pp. 1807–1814, Oct. 2003.

[76] A. SomA and A. Ballestra, "Residual stress measurement method in MEMS microbeams using frequency shift data," *Journal of Micromechanics and Microengineering*, vol. 19, no. 9, p. 095023, 2009.

[77] C.-W. Baek, Y.-K. Kim, Y. Ahn, and Y.-H. Kim, "Measurement of the mechanical properties of electroplated gold thin films using micromachined beam structures," *Sensors and Actuators A: Physical*, vol. 117, no. 1, pp. 17 – 27, Jan. 2005.

[78] J.-F. Manceau, L. Robert, F. Bastien, C. Oytana, and S. Biwersi, "Measurement of residual stresses in a plate using a vibrational technique-application to electrolytic nickel coatings," *Journal of Microelectromechanical Systems*, vol. 5, no. 4, pp. 243 –249, Dec. 1996.

[79] Q. Meng, M. Mehregany, and R. Mullen, "Theoretical modeling of microfabricated beams with elastically restrained supports," *Journal of Microelectromechanical Systems*, vol. 2, no. 3, pp. 128 –137, Sept. 1993.

[80] M. Kobrinsky, E. Deutsch, and S. Senturia, "Effect of support compliance and residual stress on the shape of doubly supported surface-micromachined beams," *Journal of Microelectromechanical Systems*, vol. 9, no. 3, pp. 361 –369, Sept. 2000.

[81] Y. J. Hu, J. Yang, and S. Kitipornchai, "Pull-in analysis of electrostatically actuated curved micro-beams with large deformation," *Smart Material Structures*, vol. 19, no. 6, p. 065030, Jun. 2010.

[82] J. Zeng, A. Garg, A. Kovacs, A. K. Bajaj, and D. Peroulis, "Residual stress extraction of MEMS beams using a wafer-scale technique," Oct. 2014, under review.

[83] MATLAB, *version 7.11.0 (R2010b)*. Natick, Massachusetts: The MathWorks Inc., 2010.

[84] J. K. Luo, M. Pritschow, A. J. Flewitt, S. M. Spearing, N. A. Fleck, and W. I. Milne, "Effects of process conditions on properties of electroplated Ni thin films for microsystem applications," *Journal of The Electrochemical Society*, vol. 153, no. 10, pp. D155–D161, Jul. 2006.

[85] G. Ritter, P. McHugh, G. Wilson, and T. Ritzdorf, "Two- and three-dimensional numerical modeling of copper electroplating for advanced ULSI metallization," *Solid-State Electronics*, vol. 44, no. 5, pp. 797 – 807, May 2000.

[86] Matovic and J, "Application of Ni electroplating techniques towards stress-free microelectromechanical system-based sensors and actuators," *Proceedings of the Institution of Mechanical Engineering, Part C: Journal of Mechanical Engineering Science*, vol. 220, no. 11, pp. 1645–1654, Nov. 2006.

[87] E. Naglich, M. Sinani, S. Moon, and D. Peroulis, "High-Q MEMS-tunable W-band bandstop resonators," in *IEEE MTT-S International Microwave Symposium (IMS)*, June 2014, pp. 1–3.

[88] G. Craven and C. Mok, "The design of evanescent mode waveguide bandpass filters for a prescribed insertion loss characteristic," *IEEE Transactions on Microwave Theory and Techniques*, vol. 19, no. 3, pp. 295–308, Mar. 1971.

[89] R. Snyder, "New application of evanescent mode waveguide to filter design," in *IEEE MTT-S International Microwave Symposium Digest*, June 1977, pp. 294–297.

[90] X. Liu, "High-Q RF-MEMS tunable resonators and filters for reconfigurable radio frequency front-ends," Ph.D. dissertation, Purdue University, West Lafayette, IN, 2010.

[91] W. Irshad, "Liquid metal droplet and micro corrugated diaphragm RF-MEMS for reconfigurable rf filters," p. 206, 2013.

[92] D. Giovanni, *Flat and Corrugated Diaphragm Design Handbook*, ser. MECHANICAL ENGINEERING. New York: Marcel Dekker, 1982.

[93] J. A. Haringx, "The rigidity of corrugated diaphragms," *Applied Scientific Research*, vol. 2, no. 1, pp. 299–325, Jan. 1951.

[94] D. Peroulis, S. Pacheco, K. Sarabandi, and L. Katehi, "Electromechanical considerations in developing low-voltage RF MEMS switches," *IEEE Transactions on Microwave Theory and Techniques*, vol. 51, no. 1, pp. 259–270, Jan. 2003.

[95] C. van Mullem, K. Gabriel, and H. Fujita, "Large deflection performance of surface micromachined corrugated diaphragms," in *International Conference on Solid-State Sensors and Actuators, Digest of Technical Papers.*, June 1991, pp. 1014 –1017.

[96] K. Wise, "Performance of nonplanar silicon diaphragms under large deflections," *Journal of Microelectromechanical Systems*, vol. 3, no. 2, pp. 59–68, June 1994.

[97] F. Ke, J. Miao, and Z. Wang, "A wafer-scale encapsulated RF MEMS switch with a stress-reduced corrugated diaphragm," *Sensors and Actuators A: Physical*, vol. 151, no. 2, pp. 237–243, April 2009.

[98] P. Scheeper, W. Olthuis, and P. Bergveld, "The design, fabrication, and testing of corrugated silicon nitride diaphragms," *Journal of Microelectromechanical Systems*, vol. 3, no. 1, pp. 36–42, Mar. 1994.

[99] M. Fu, A. Dehe, and R. Lerch, "Analytical analysis and finite element simulation of advanced membranes for silicon microphones," *IEEE Sensors Journal*, vol. 5, no. 5, pp. 857–863, Oct. 2005.

[100] J. Zeng and D. Peroulis, "Design consideration of large-displacement RF MEMS tuners under fabrication uncertainties," Nov. 2014, under review.

[101] Y. Shim, Z. Wu, and M. Rais-Zadeh, "A high-performance, temperature-stable, continuously tuned MEMS capacitor," in *IEEE 24th International Conference on Micro Electro Mechanical Systems (MEMS)*, Jan 2011, pp. 752–755.

[102] M. A. Philippine, O. Sigmund, G. M. Rebeiz, and T. W. Kenny, "Topology optimization of stressed capacitive RF MEMS switches," *Journal of Microelectromechanical Systems*, vol. 22, no. 1, pp. 206–215, Feb. 2013.

[103] J. Zeng, Z. Yang, and D. Peroulis, "Nonuniform micro-corrugated capacitive MEMS tuner with thermal stability," Nov. 2014, to be submitted.

[104] T. P. Weihs, S. Hong, J. C. Bravman, and W. D. Nix, "Mechanical deflection of cantilever microbeams: A new technique for testing the mechanical properties of thin films," *Journal of Materials Research*, vol. 3, pp. 931–942, 10 1988.

[105] D. Peroulis and L. Katehi, "Electrostatically-tunable analog RF MEMS varactors with measured capacitance range of 300%," in *IEEE MTT-S International Microwave Symposium Digest*, vol. 3, June 2003, pp. 1793–1796 vol.3.

[106] L. Dussopt and G. Rebeiz, "Intermodulation distortion and power handling in RF MEMS switches, varactors, and tunable filters," *IEEE Transactions on Microwave Theory and Techniques*, vol. 51, no. 4, pp. 1247–1256, Apr 2003.

VITA

VITA

Juan Zeng received the Bachelor's degree in Microelectronics from Harbin Institute of Technology, China, in 2007, and the Master's degree in Electrical and Computer Engineering from Tufts University, Medford, MA, in 2009. She is currently working toward the Ph.D. degree in Electrical and Computer Engineering at Purdue University, West Lafayette, IN.

Her research interests include tunable RF MEMS devices and related RF integrated circuits for reconfigurable wireless communication systems.